VHF-PECVD and Analysis of Thin Nano-crystalline Silicon Films With a Multi-tile Plasma Source for Solar Energy Applications

Eamonn Monaghan

January 30, 2014

A thesis submitted for the degree of

Philosophiæ Doctor (PhD)

from

Dublin City University,
School of Physical Sciences

Supervisor: Dr. Albert Ellingboe of Dublin City University

External Examiner: Prof. Masaru Hori of Nagoya University, Japan.

I hereby certify that this material, which I now submit for assessment on the programme of study leading to the award of PhD, is entirely my own work, and that I have exercised reasonable care to ensure that the work is original, and does not to the best of my knowledge breach any law of copyright, and has not been taken from the work of others save and to the extent that such work has been cited and acknowledged within the text of my work.

Signed: _____ (Candidate) ID No.: _____ Date: _____

Eamonn Monaghan

Plasma Research Laboratory,
School of Physical Sciences & NCPST,
Dublin City University,
Glasnevin, Dublin 9, Ireland.

Acknowledgments

First and foremost I would like to thank my supervisor during this work, Dr. Bert Ellingboe. From start to finish, his patience of my eccentric experimentation and laborious writing surpassed even my own. In addition, he has set for me an intimidating standard of what it is to think like a scientist. His insights and explanations always proved useful in expanding my understanding of science and his guidance helped steer this research where it needed to go.

I have had the pleasure to work alongside many people during my time in DCU. To current and past members of the plasma research lab, particularly; Cezar Gaman, Kevin Ryan, & Dave O'Farrell: You were always there to work out the nitty-gritty details over a coffee or to discuss the appropriate units with which to measure... anything. To those whom I worked with as part of *Phive*, particularly: Niel, Fiachra, & Tomasz, you gave me a unique perspective on what it takes to make an idea into a reality and inspired me with you work ethic, as well as your comradery. In addition to those above, my sincerest thanks go to the administrative and technical staff who each helped me greatly these last years, particularly: Barry O'Connell, Pat Wogan, Des Lavelle, Lisa Peyton & Sheila Boughton.

I also had the great opportunity to collaborate with many amazing research teams outside of DCU during the course of this research. To: Dr. Tatiana Perova and David Adley of TCD; Rusty Jewett, Brian Drews, Matt Jaskot, and all members of Sencera; as well as to Prof. G.Y. Yeom and his group in SKKU, It was a pleasure to meet and work with all of you.

To my friends, Chip, Foxi, Al, Jen, Kev, and Man-d, as well as many others. Thank you for distracting me when I needed distracting and encouraging me when I needed that too. The support of friends is difficult to describe, it is an amazing asset and a welcome luxury. I value yours immensely.

My family are my rock. They are somewhat unstable, but I cling to them none the less. To my siblings; Kevin, Eilish & Declan: We have nothing in common and are so much alike, you are each amazing and I love you. My mother is the best person I know, "she makes good people." My dad is my hero, I only knew him as a great father, but, I have seen his friends remember him and now I know, he was a great man. In this regard, I hope I can follow in his footsteps.

Contents

List of Figures

Abstract

This work presents a characterisation of a differentially powered, multi-tile VHF capacitively coupled plasma source, MAMELUKE. The use of a differential multi-tile source imposes a spatial structure on the plasma due to the combination of capacitive and inductive power coupling. Specifically, this thesis concentrates on the PECVD of nano-crystalline silicon for applications in thin film solar manufacturing. We examine films produced by the MAMELUKE source focusing on the capability to produce uniform, high quality films over large areas with high deposition rates. The measurements of film properties are then used in combination with knowledge gained from existing works to infer information about the gas phase chemistry produced by MAMELUKE.

The deposited films are characterised for silicon deposition rate; as measured by profilometry, and film crystalline fraction; as measured by raman spectroscopy. These measurements are made as function of process parameters and, also substrate position.

Films deposited in MAMELUKE are found to be crystalline in nature at deposition rates far exceeding conventional industrial processes and for areas larger than yet achieved by frequencies exceeding 100 MHz. The high deposition rates achieved are attributed to the unique gas phase chemistry achieved using VHF excitation.

The spatial structure imposed by the multi-tile source is found to have an effect on both the film crystalline fraction and deposition rate, depending on the power and flow settings during deposition. When non-uniformities in the film crystalline fraction are present it is observed that the crystalline fraction at tile centrers is consistently lower than the tile edges. This is attributed to a non uniformity in the gas phase chemistry, specifically the atomic hydrogen density, which is due to an un-even delivery of process gas across MAMELUKE.

Capacitive coupling is seen to be dominant at tile centrers and inductive coupling dominant at tile boundaries; the effect of this on plasma behaviour and thus film properties is examined. Power coupling is classified as capacitive when tile centre locations display the highest silane activation and thus deposition rate, conversely power coupling is classified as inductive when tile edges display the highest silane activation and thus deposition rate.

Chapter 1

Theory

1.1 Plasma

This document concerns itself with specific areas of interest in the fields of plasma physics and engineering. These areas include but are not limited to: The advantages of high frequency (VHF) plasma excitation, realising the advantages VHF across large substrate areas by implementing a multi-tile capacitively coupled plasma (CCP) configuration, and the subsequent process improvements possible in the field of thin film silicon deposition; specifically concentrating on applications in thin film solar manufacturing. To better comprehend claims made later in the thesis it is necessary to first briefly examine some basic concepts of plasma physics. This chapter can in no way encompass the vast field that is plasma physics, it will instead try to present in a succinct way, a series of descriptions which will serve to illustrate some basic concepts in plasma physics. The following exploration of these concepts relies heavily on the author's reading and interpretation of Chapter 3 from "Glow Discharge Processes: Sputtering and Plasma Etching" by Brian Chapman[1][1].

[1]Every effort has been made to avoid plagiarism and despite the likely crossover in reasoning and verbiage, no aspect of the following has been copied directly from this work.

1.1.1 Basic Plasma Science

Starting with a weakly ionised gas, containing electrons and ions and a majority of neutral species; the densities of these different particles are denoted by n_e, n_i, and n_n (in cm^{-3}) respectively. Similarly, the average kinetic energy (temperature) of these species will be denoted by T_e, T_i, and T_n (in eV) respectively. The subscripts n & i denote collections of neutral and ionised species [2]. The population of ions and neutrals can consist of single atoms, molecules and radicals as well the products of chemical reactions taking place within the plasma, and at any surface with which the plasma may be in contact. Just as with a gas, all particles are free to move and interact with each other. Particle collisions will result in a transfer of energy. The primary processes in plasma are driven by energy transfer from electrons to atomic or molecular particles. Collisions such as this can result in various reactions including: Excitation, combination, dissociation, ionisation, neutralisation and charge transfer.

- Excitation: $A + e^- \rightarrow A^* + e^-$
- Combination: $A + B + e^- \rightarrow AB + e^-$
- Dissociation: $AB + e^- \rightarrow A + B + e^-$
- Ionisation: $A + e^- \rightarrow A^+ + 2e^-$
- Neutralisation: $A^+ + e^- \rightarrow A$
- Charge transfer: $A^+ + B \rightarrow A + B^+$

The reaction rate for a given process, w_A is dependent on the reaction rate coefficient, k, as well as on the density of electrons energetic enough to produce the reaction and the density of the source atoms / molecules / ions[3]. The reaction rate coefficient is a function of both the collisional cross section σ of the source species and the energy distribution function(s) of the particles[4][2, p. 21].

[2]While the differences between neutral & ionised species can be significant they are electrically equivalent, and similar in mass so they are grouped together

[3]All species which appear on the left hand side of the above list of reactions could be described as a "source species"

[4]specifically the kinetic or thermal energy distributions

In this description of plasma behaviour the following assumptions will be made:

- All species are homogeneously distributed within a fixed volume or enclosure [5]
- There is a low ionisation fraction $\approx 0.1\%$ and only single ionisation will be considered, so that $n_e \approx n_i$. Given the electron temperature assumed above, ionising collisions occur at a relatively low frequency, and the probability of a subsequent ionisation is even less likely given the increase in the requisite energy.
- The plasma is in a steady state, i.e. the properties of the plasma are maintained as constant.
- That the plasma is quasi-neutral $\sum Q^+ = \sum Q^-$, where Q^+ and Q^- represent the positively and negatively charged species respectively. The term quasi-neutrality is used because, while local charge imbalances within the plasma are not uncommon, it is assumed spatially averaged plasma, or plasma bulk remains neutral. We can represent this mathematically as above
- Processes will act so that the flux of positively and negatively charged particles (per unit area per second) out of the plasma are equal.

$$\Gamma_e = \Gamma_i \tag{1.1}$$

where Γ_x is the flux of species x out of the plasma which can be written in terms of the root mean square velocity, $\overline{c_x} = \sqrt{\frac{8k_bT}{\pi m_x}}$

$$\Gamma_x = \frac{n_x \overline{c_x}}{4} \tag{1.2}$$

- Electrons will be assumed to have a temperature much higher than that of the ions and neutrals and are as such not in thermal equilibrium with them. As a result ions and neutrals will be considered stationary relative to the faster electrons. Put simply, this is a result of the mass ratio of the electrons to any

[5] The plasma is contained within a chamber

other species, which is significant ($> 10^3$), this assumption will be justified further later, in section 1.1.6 but is necessary for much the introduction which follows. The following estimates serve to offer a sense of scale and would hold true for the majority of industrial plasmas.

  - $T_e \approx 1.0 - 1.5\,\mathrm{eV}$
  - $T_e \gg T_i \approx 2T_n$

- Each species; electrons, ions and neutrals, are assumed to be in thermal equilibrium with other particles of the same type with Maxwell Boltzmann energy distributions

$$\frac{n'_x(\varepsilon)}{n_x} = -exp\left(\frac{\varepsilon}{k_b T_x}\right) \tag{1.3}$$

where $n'_x(\varepsilon)$ is the density of a given species as a function of thermal energy, ε, and k_b is Boltzmann's constant.

1.1.2 Plasma Sheath

Given the homogeneous distribution of species, faster electrons near the edge of a fixed plasma volume will be lost to the surroundings first. This sets up a space charge imbalance giving rise to an electric field. This electric field acts such that ions which approach the edge of the plasma are accelerated towards the walls of the enclosure while electrons with low energy are contained within the plasma bulk[6]. The region over which this electric field extends is known as the sheath. The sheath is an natural occurrence, necessary to balance/moderate the flow of charge from the plasma to a surface with which it is in contact, thus maintaining quasi-neutrality. The sheath forms a boundary between the plasma and all surfaces that are in contact with it.

To examine sheaths qualitatively, consider an infinite planar surface in contact with the plasma, the symmetry of which allows us to examine the behaviour of the plasma

[6]High energy electrons can overcome the electric field and escape to the surroundings

in one dimension (the displacement from that surface, which we will call x[7]). To think quantitatively about the sheath, consider the number of electrons with energy high enough to overcome the sheath potential, which we will refer to as n'_e as determined by Maxwell Boltzmann (Equation 1.4) and use this quantity to evaluate the condition for quasi-neutrality (Equation 1.5).

$$n'_e(Vs) = n_e exp\left(-\frac{(eV_s)}{kT_e}\right) \tag{1.4}$$

$$\frac{n'_e\overline{c_e}}{4} = \frac{n_i\overline{c_i}}{4} \tag{1.5}$$

where V_s is the potential difference across the sheath. Then combine this equation with the flux equality as expressed in equation 1.5,

$$\frac{n_e exp\left(-\frac{e(V_s)}{kT_e}\right)\overline{c_e}}{4} = \frac{n_i\overline{c_i}}{4} \tag{1.6}$$

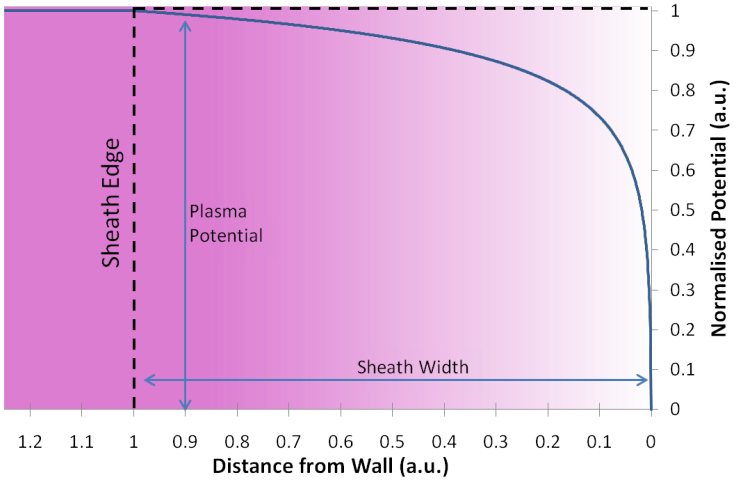

Figure 1.1: A graph of electrical potential versus distance from an infinite surface in contact with a plasma. The potential has been normalised to that within the plasma bulk.

[7]Treating the surface as infinite; ignores asymmetry in the dimensions parallel to the surface are negated. This is justifiable considering the scale of typical plasma sources and of plasma shielding (chapter 1.1.3)

Then assuming only singly ionised ions are present, by letting $n_e = n_i$ the above can be simplified by algebraic manipulation, to give the following expression for the potential drop across a sheath(Equation 1.7)

$$V_s = \frac{kT_e}{2e} \ln\left(\frac{\overline{c_e}}{\overline{c_i}}\right) = \frac{kT_e}{2e} \ln\left(\frac{m_i T_e}{m_e T_i}\right) \tag{1.7}$$

1.1.3 Plasma Shielding & The Debye Length

The sheath, as describe ins the previous section allows a plasma to be maintained so long as enough energy is supplied to maintain a sufficient ionisation fraction i.e. it is the effect that allows partial containment of the electrons, preventing their flow to ground. If all electrons were free to flow to ground no further ionisation would be possible and a plasma could not be maintained.

Further to this, consider the behaviour of charged particles within the plasma bulk. Given that particle will naturally move towards particles of opposite charge and away from particles of the same charge is easy to conceptualise that the particles on average will behave in such a way as to spread them-selves evenly and thus oppose a local potential inhomogeneity or charge density imbalance. If a test point charge (or some other perturbation of potential) is introduced to the plasma the local charged particles will move so as to counter the imbalance, as a result particles which are sufficiently spatially removed from the test charge will not be affected by the perturbation[8]. Effectively the net electric field that charged particles experience approaches the field experienced at infinity at a greater rate. Shielding in plasmas can be compared to the observed charge of atoms, where the nucleus and electron cloud independently represent high positive and negative charge density. When observed as a single entity the atom appears neutral. Plasma shielding is a more dynamic process, which can continuously shield a dynamic change in potential as long a the rate at which the local potential changes is slow enough that particles can respond. The radius over which plasma shielding is most significant is called the Debye length, λ_d, the derivation of which will now be

[8]The electric potential of the perturbation would penetrate significantly farther in vacuum or a neutral gas

summarised.

Starting with Poisson's equation,

$$\frac{\mathrm{d}^2V}{\mathrm{d}x^2} = \frac{\rho}{\epsilon_0} = -\frac{e}{\epsilon_0}(n_i - n_e(x)) \tag{1.8}$$

the electron density is then expanded using the Boltzmann distribution

$$\frac{\mathrm{d}^2V}{\mathrm{d}x^2} = -\frac{e}{\epsilon_0}\left(n_i - n_e exp\left(-\frac{e\left(\Delta V\left(x\right)\right)}{kT_e}\right)\right) \tag{1.9}$$

where $\Delta V(x)$ is the local potential difference due to the point charge, and x is the displacement from the point charge in question[9]; $\Delta V(0) = \Delta V_0$ is some finite potential difference relative to the (un-perturbed) plasma potential. Again assuming only single ionisation; $n_e = n_i$

$$\frac{\mathrm{d}^2V}{\mathrm{d}x^2} = -\frac{en_e}{\epsilon_0}\left(1 - \exp\left(-\frac{e\left(\Delta V\left(x\right)\right)}{kT_e}\right)\right) \tag{1.10}$$

The exponential factor can be expanded to the first degree of the Taylor expansion $e^x = \sum_{x=0}^{\infty} \frac{x^n}{n!}$, giving $1 - \frac{e(\Delta V)}{kT_e}$ under the assumption that $\Delta V(x) \ll k_B Te$. Giving the following result:

$$\frac{\mathrm{d}^2V}{\mathrm{d}x^2} \approx \frac{en_e}{\epsilon_0}\left(\frac{e\left(\Delta V\left(x\right)\right)}{kT_e}\right) \tag{1.11}$$

This differential equation can then be solved, giving:

$$\Delta V(x) = \Delta V_0 \exp\left(-\sqrt{\frac{x^2 n_e e^2}{k_b T_e \epsilon_0}}\right) \tag{1.12}$$

Which can then be rewritten as follows:

$$\Delta V(x) = \Delta V_0 \exp\left(-\frac{x}{\lambda_d}\right) \tag{1.13}$$

This allows the definition of the Debye length (Equation 1.14) as the displacement,

[9]This derivation is separate from and independent of that of the plasma sheath voltage where x was used in a different context

$|x| = \lambda_d$, where ΔV will be a factor of e (≈ 2.7182) less than ΔV_0

$$\lambda_d = \sqrt{\frac{\epsilon_0 k_B T}{e^2 n_e}} \tag{1.14}$$

1.1.4 Plasma Frequency

It should be noted that there are limitations associated with the above derivations of sheath voltage and Debye length which when considered give further insight into plasma behaviour. The derivations above only account for the behaviour of electrons in response to a chamber wall or local potential perturbation, ignoring the behaviour of ions. This is done under the reasonable assumption that heavy ions respond more slowly to changing electric fields within the plasma and can be assumed to be stationary. To examine the validity of this assumption it is sensible to quantify the time scale over which electrons (and ions) will respond to changes in the instantaneous electric field as opposed to a time averaged or constant electric field. To this end, we will derive the natural frequency at which electrons oscillate within the plasma. For the ease of mathematics and visualisation, uniformity in two spatial dimensions will again be assumed. It should be noted that the movement of ions will again be neglected in this calculation and as such can not be used justify that assumption.

Considering a slab of quasi-neutral plasma with a fixed thickness in the x[10] direction, τ; if the electrons are linearly displaced from the ions by $\Delta x << \tau$ as shown in figure 1.2 b), then a space charge imbalance will exist in the region from $x = -\Delta x$ to $x = 0$, where there is an excess of negative charge and from the region from $x = \tau - \Delta x$ to $x = \tau$, where there is an excess of positive charge. The resulting electric field, ε can be quantified by integrating Poission's equation as follows;

$$\frac{d\varepsilon}{dx} = \frac{n_e e}{\epsilon_0} \overset{integrating}{\longrightarrow} \varepsilon = \frac{n_e e \Delta x}{\epsilon_0} \tag{1.15}$$

[10] x is again being reused in a to represent displacement in one dimension in a context separate from the previous derivations

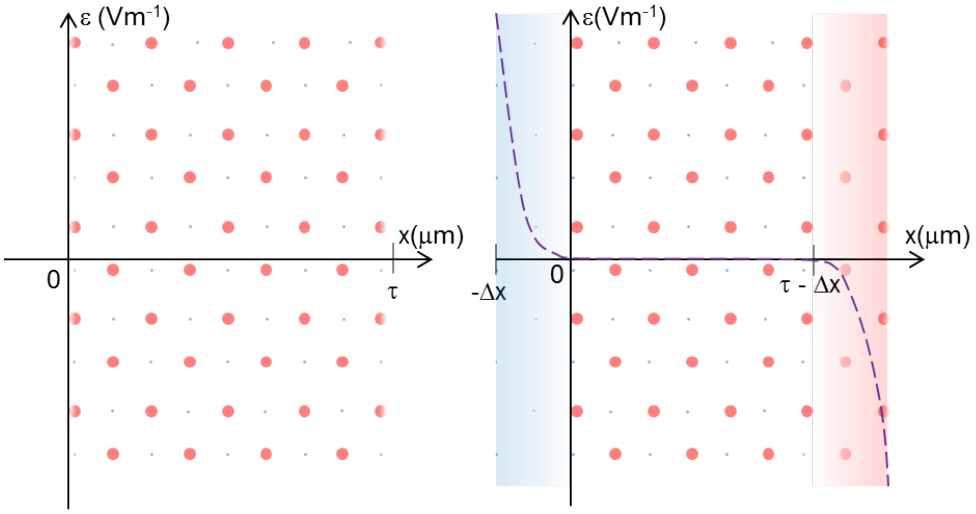

Figure 1.2: A visualisation of a plasma slab, assumed to be uniform in 3 dimensions (a) and then displaced in one of those dimensions, x (b). The strength of the (restorative) electric field is represented by the dashed line in (b)

and this expression can then be substituted into Newton's second law:

$$F = ma = -e\varepsilon \tag{1.16a}$$

$$\Rightarrow F = m_e \frac{d^2(\Delta x)}{dt^2} = \frac{n_e e^2}{\epsilon_0}\Delta x \tag{1.16b}$$

This result shows that the force on an electron is restorative; proportional to and in the opposite direction of the displacement, Δx. Classical mechanics tells us that such a force will give rise to harmonic motion the frequency of which is given by

$$\omega_e = \sqrt{\frac{n_e e^2}{m\epsilon_0}} \tag{1.17}$$

While a similar derivation can be made to quantify the natural ion frequency, ω_i it is necessary in this case to account for the motion of both electrons and ions which adds a layer of complexity to the derivation. Without exploring this explicitly it can be noted that as long and the electron temperature, T_e, is high enough the the result can be

simplified to mirror the expression for the electron frequency.

$$\omega_i = \sqrt{\frac{n_i e^2}{m_i \epsilon_0}} \tag{1.18}$$

For typical electron densities ($n_e \approx 10^{10}$) the electron frequency is calculated to be in the hundreds of Megahertz while the ion frequency will be in the range 1-5 Megahertz. Significantly these frequencies lie on either side of the typical excitation frequencies used to drive typical RF plasma reactors, most commonly 13.56 MHz, but ranging into the low hundreds of Megahertz. The implication of this is that electrons will show a response to the instantaneous electric or magnetic field produced by a powered electrode while ions will respond only to the time averaged field. This accounts for how energy is coupled more effectively to the more mobile electrons but, as mentioned above, it does not account for the assumption that electrons and ions are out of thermal equilibrium.

1.1.5 Langmuir Probe

At this stage we are able to examine how the plasma will interact with a small conducting element with a given bias relative to the plasma; a Langmuir probe. The probe will be immersed within the plasma, so in the absence of a bias a sheath will natural form around its exposed surfaces to regulate current flow. The exposed conducting element, or tip, is connected to an external power supply by means of an insulated and shielded wire. The current that is drawn through the probe tip is measured as a function of the applied voltage[11] as seen in figure 1.3.

If you consider the plasma enclosure to be at a potential of 0 V, or grounded, then the plasma will have a constant positive potential measured relative to the enclosure due to the sheath and the homogeneous charge distribution already examined. The voltage of the probe tip will be measured relative to the plasma chamber. The plasma behaviour will be described as the probe bias (V_{pr}) is swept from negative to positive

[11] This is typically done by means of a "sense resistor" of a known impedance. The resistor is placed between the probe and the power supply and the current can be calculated from the measured voltage-drop using Ohm's law, $I = \frac{V}{R}$.

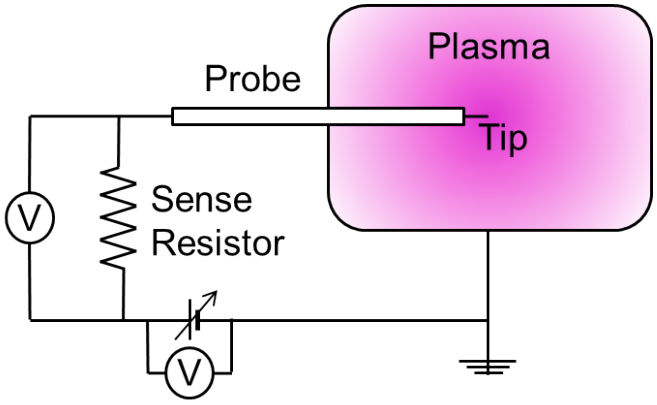

Figure 1.3: Electrical schematic of a Langmuir probe immersed in a plasma. The Schematic shows a DC power supply and two voltage measurements, one of which is converted to a current using the known value of the sense resistor

and the critical of interest points noted in sequence. The electron and ion currents will be described in isolation, however only net current can be measured using the probe (figure 1.4).

To begin, the probe is held at strong negative bias such that the electron current is suppressed; the potential difference across the sheath will be augmented by probe voltage and as such will repel even the highest energy electrons, at this point the (positive) ion current will be determined only by the random motion of ions into the sheath and any further decrease in voltage will only increase the ion energy. This is called the ion saturation current. As the potential of the probe is increased the voltage across the sheath will reduce allowing electrons from the high energy portion of the EEDF to leak though the sheath to the probe tip; the ion current will remain constant. When V_{pr} is increased to the point where the electron and ion currents are equal giving zero net current; this is called the floating potential as it is the potential which an electrically isolated object in the plasma would acquire[12]. As V_{pr} is further increased it will finally reach the plasma potential, here there will be no sheath and net negative current will flow due to the high mobility of the electrons, the ion current will be suppressed by even a modest positive potential difference and the electron current will

[12]a floating object in the plasma would acquire excess charge so as to equalise the electron and ion currents to the surface maintaining quasi-neutrality

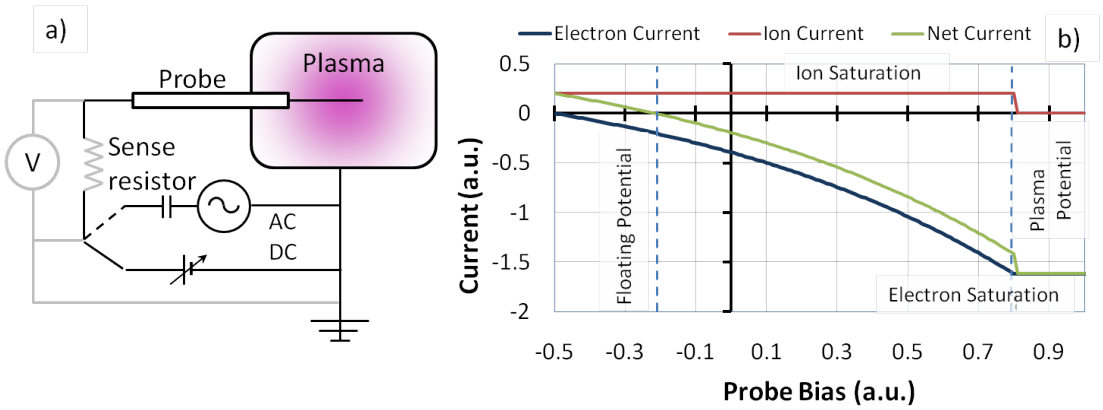

Figure 1.4: A schematic of a Langmuir probe which can be biased using an AC or DC supply. The probe potential is measured relative to ground and current is measured by the potential drop across a sense resistor b) a Current versus DC potential graph expected for such a probe

saturate according to the natural flux of charge carriers in the plasma and the surface area of the probe A_{tip}.

$$I_{sat} = A_{tip} e \Gamma_e \tag{1.19}$$

Now that the probe behaviour under a DC bias is understood it is informative to consider an sinusoidal alternating current (AC) bias upon the probe in question. To ensure that only AC current flows through the circuit, a blocking capacitor[13] is placed between the power source and the probe (Figure 1.4 a). It it necessary to then consider the response of the different charge carriers in the plasma.

Considering an alternating bias around 0 V, we can see form the I-V curve in figure 1.4 that for the majority of the the AC cycle net negative current will flow. Net positive charge will only flow for the portion of the cycle where the bias is less than the floating potential. As a result over a single cycle an excess of negative charge will accumulate on the probe. Since DC current cannot flow through the blocking capacitor this charge will continue to accumulate over several AC cycles. The charge accumulation will induce a DC voltage offset which will reach a constant value when the time averaged current

[13] A "blocking capacitor" prevents the flow of DC current through the probe into or out of the plasma so that the response to AC power van be measured.

to the probe tip is zero[14]. This self bias acts so as to balance the net current from the plasma over time and as such prevents further charge imbalance.

1.1.6 AC Sheaths & Capacitive RF Coupling

At this point the mechanisms by which RF voltages couple energy into a plasma across a sheath can be understood. The AC electromagnetic field accelerates electrons near the sheath edge while heavy, slow ions will only react to the time averaged electromagnetic field. Charge carriers in the plasma bulk are not directly affected by the field due to plasma shielding. The accelerated electrons have a high probability of colliding with other particles; these electrons will dissipate their energy through the plasma by a series of collisions tending towards a thermal equilibrium.

This energy is transferred to the electron population far more effectively than it is through more massive particles which can simply explained by looking at classical description[15] of energy transferred to a particle of different mass, as follows:

$$E_M = \frac{4Mm}{(M+m)^2} E_m \tag{1.20}$$

where E_M, and E_m are the ion and electron energy respectively and M, m are their masses. Using such momentum conservation calculations, it is easy to show that electrons transfer a low fraction of their energy to other, more massive species relative to compared to electron-electron collisions[3, p. 10]. Electrons are also thermally isolated from the surroundings given that the sheath acts to contain electrons. In contrast ions remain in good thermal contact with the surroundings (chamber walls) through collisions with neutral species which are unaffected by the electric field of the sheath [16]. This combination of effects justifies the proposition at the beginning that electrons

[14]The DC offset will act so as to equalise the amount of positive and negative current driven over a single AC cycle. Once the positive and negative currents are equal, no further charge will accumulate and the DC offset on the probe will remain constant.

[15]This calculation assumes a "head-on" collision at but the principle holds for less direct collisions

[16]Since the neutrals are of effectively equal mass as the ions they efficiently transfer their energy to each other.

remain out of thermal equilibrium with the heavier ions and neutrals.

1.2 VHF Plasma Chemistry

The treatment of surfaces using plasma processes is a widely used and highly studied tool. Using plasmas, layers of material can be deposited and (selectively) etched as well as activated, pacified or otherwise chemically or physically modified. Much work and time is given to the characterisation of these processes and (to a lesser extent) the plasma and gas phase properties which determine the way a plasma interacts with a substrate. When the excitation frequency of a plasma is increased there are 2 primary plasma effects, which lead to desirable changes for many industrial processes. An introduction to these effects will be provided here.

The best understood of these effects is the behaviour of the plasma sheath (described earlier in chapter 1.1.2). It is useful in this situation to consider the sheath as a capacitor in series with a resistive load (the plasma), hence the term capacitively coupled Plasma (CCP) (Figure 1.5). Indeed the current which flows across the sheath is primarily displacement current like capacitors[17]. The impedance of the sheath will then be strongly dependant on the excitation frequency. If the sheath were to act purely as a capacitive element the impedance would follow an inversely proportional behaviour with frequency,

$$Z_{sheath} = \frac{1}{j\omega c} \tag{1.21}$$

where $\omega = 2\pi f$. The higher the excitation frequency, the lower the sheath impedance and thus the more current that is free to flow through the entire circuit. This has several implications on the plasma structure. Given a constant power but a higher frequency:

- The sheath impedance (Z_s) drops which has the effect of decreasing the sheath voltage (V_s). The sheathe impedance determines the energy of ions impacting the substrate. For many plasma processes it is desirable to minimise the ion impact energy to avoid damage to the substrate/coating surface making high frequency

[17]Displacement current in capacitors and sheaths is the current driven by the AC electric field across the insulating boundary between conductive surfaces usually consisting of a dielectric in capacitors, which is analogues to the non-conducting sheath in a CCP.

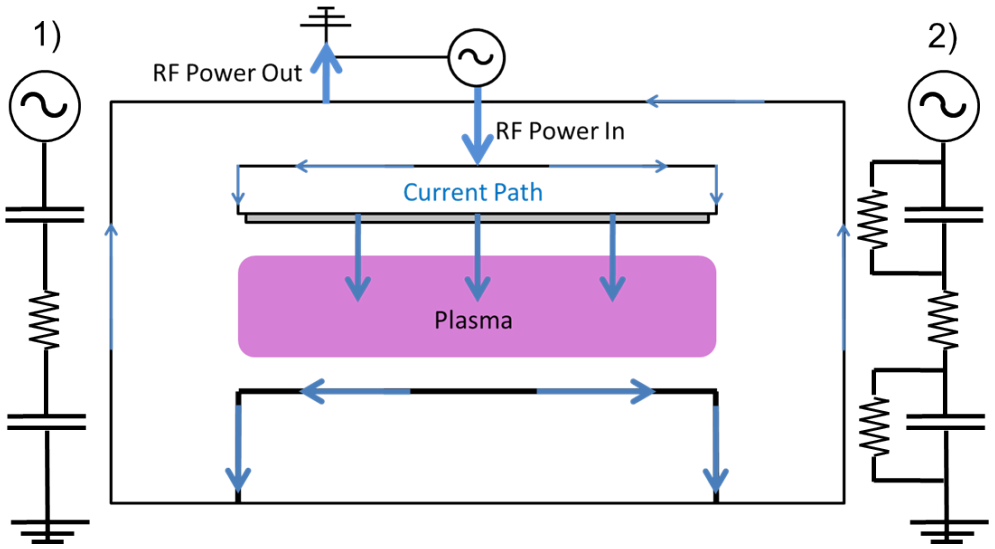

Figure 1.5: A simple CCP plasma showing the paths that currents take through the various elements in series, the effective electronic circuit is shown in it's most simple form to the left, 1) and with the introduction of sheath resistors to the right, 2). The capacitive sheath elements are used to illustrate the effect of changing excitation frequency in a CCP. The sheath resistors represent power lost to the acceleration of ins and their impact energy which is transferred to the surface.

excitation advantageous.

- The net current driven between the electrodes and through the plasma (I_p) increases. If the plasma is considered to be a primarily resistive element in the circuit. The power dissipated in the plasma can be considered ohmic heating where, the power, P_{ohm} is proportional to the square of the current driven through it, $P_{ohm} = I^2R$. Increase in P_{ohm} increases the electron temperature and thus changes the gas phase chemistry within the bulk.

When the 2 effects are considered together it is clear that even if the power coupled to the plasma and thus the electron temperature were kept constant for a higher excitation frequency, the fractional power coupled to the plasma will increase, while the fractional power dissipated in the sheath will be reduced[18].

Apart from the sheath behaviour the excitation frequency has been observed to

[18]While a purely capacitive element would not dissipate any power, power is deposited in the sheath by the acceleration of ions and their impact at the substrate / electrode surface

to have a demonstrable effect on the shape of a plasma's electron energy distribution function (EEDF). The EEDF has been shown to deviate from the expected Maxwellian distribution, towards a "2 temperature" regime[4]. This effect is observed as a bowing and accentuation of the high energy side of the energy distribution function. This represents a numerically low, but significant[19] population of higher energy electrons. This is accompanied by a shift of the major maxima of the distribution towards a lower energy[20].

This effect is accentuated by further increasing the excitation frequency. From a plasma processing perspective the EEDF produced by a higher excitation frequency allows for high energy reactions particularly ionisation and dissociation to occur while the average electron velocity (T_e) remains low. As a result both plasma stability and efficient chemical activation of precursors can be maintained at lower RF power levels. [4, 5]

Both sheath effects and VHF EEDF behaviour have shown their applicability in PECVD and plasma etching tools, primarily in the semiconductor industry [6]. "Triode" sources utilise dual frequency excitation, where a combination of low (RF) and high (VHF) frequencies are used to excite and maintain the plasma. By altering the power delivered by each frequency, independent control the electron temperature and the sheath potential is achievable[21]. In addition to this increased flexibility, process improvement has been directly associated with an increase in the higher excitation frequency alone. This will be discussed further in chapter 2.2. The utilisation of VHF excitation in CCP has been limited however, by it's incompatibility with larger substrates the nature of which will be explained in Chapter 1.4.

[19] any population of these high energy electrons has a significant effect on the chemical products produced in the plasma

[20] While the maxima of a symmetric Maxwellian would typically be referred to as the electron temperature, T_e because of the deviation in shape a more general term like the distribution maxima is appropriate

[21] independent control of T_e and V_s translates to independent control of the radical production rate and the ion bombardment energy

1.3 Thin film silicon

The PECVD of thin film silicon is an extremely active research field. As one of the primary solar energy production materials, advances thin film silicon growth translate to the development of new manufacturing techniques for the generation of solar panels with larger area / higher efficiency / greater stability. Hydrogenated nanocrystalline silicon (nc-Si:H)[22] is often the active material in thin film transistors (TFTs) in liquid crystal displays (LCDs) and is another area where research sees direct application. The deposition of nc-Si:H is the primary topic of interest in this thesis. Nano-crystalline silicon is a mixed phase material; it consists of small crystallites surrounded by a hydrogenated amorphous (a-Si:H) matrix. The synthesis and appearance is not significantly different from amorphous material but has significant differences in it's electrical and optical properties.

When examining nc-Si:H as an absorbing material in photo voltaic cells it offers a unique set of advantages from a material properties perspective.

- Similarly to a-Si:H, nc-Si:H can be deposited on glass substrates coated with a thin conducting oxide (TCO) back contact allowing for expansion in substrate area. Furthermore, because of it's low deposition temperature nc-Si:H can be utilised in roll to roll manufacturing line on flexible plastic substrates.

- nc-Si:H does not suffer from light induced degradation [7], unlike a-Si:H, where the efficiency of a panel is seen to drop by $10 - 15\%$ over the first years of operation.

- The band-gap of nc-Si:H is lower than that of a-Si:H so its absorption spectrum extends into the NIR band of the EM spectrum. Given that clouds are more transparent to low energy photons, PV modules based on nc-Si:H absorbing layers can provide electricity even on overcast days. The bang gap difference of nc-Si:H also allows it to be incorporated in double or triple junction stacked cells along

[22]Nanocrystalline silicon is often referred to as microcrystalline, polycrystalline, or multicrystalline silicon. All material found to be in a crystalline growth phase will be referred to as nanocrystalline for the purposes of this thesis

with a-Si:H cells where each material absorbs a different portion of the spectrum increasing the panel efficacy.

The major disadvantage of nc-Si:H is an indirect band gap. Photons incident on nc-Si:H require 2 particle (photon & phonon) interaction to create an electron hole pair. As a result the absorption coefficient is low when compared to a-Si:H. In order to produce comparable efficacy levels nc-Si:H absorbing layers must be 100 times thicker than the amorphous equivalent, this results in a lengthy deposition process which becomes a considerable fraction of a panels production cost.

PECVD using CCP is the most prevalent deposition technique for both a-Si:H and nc-Si:H. PECVD can be preformed at relatively low temperatures and high deposition rates. The presence of high energy electrons in plasma allow for dissociative reactions which would usually require hundreds of degrees of additional thermal energy to produce. Other techniques such as hot wire chemical vapour deposition (HW-CVD) [8–10] have been explored but PECVD remains the industry standard.

PECVD of amorphous and nano-crystalline silicon use a feed gas mix of mono silane (SiH_4) and hydrogen (H_2). Throughout the PECVD process there are several critical processes which determine the film properties. The rate at which these processes occur and thus the electrical and chemical properties of the plasma are controlled by the experimental parameters[23].

Working backwards, the preferred plasma conditions for high quality nc-Si:H deposition will first be examined, then the critical plasma processes which can facilitate these conditions will be introduced, finally several deposition process regimes will be examined for their advantages and disadvantages. The following are necessary plasma conditions in order to deposit high quality nano-crystalline films the reasoning behind each condition is briefly introduced here and will be elaborated on later in the chapter:

- High density of H
  - Passivation of surface dangling bonds allowing for high radical mobility increasing the likelihood of deposition in crystal lattice site[11, 12].

[23]Primarily but not exclusively: Power, pressure, gas flow and dilution ratio

  - Preferential etching of amorphous material[13].
  - Chemical annealing of the surface and bulk during growth converting strained amorphous bonds to relaxed local crystallites[12, 14, 15].

- Low density of SiH_4
  - Reduces rate of the annihilation reaction which consumes atomic hydrogen and produces molecular hydrogen $SiH_4 + H \rightarrow SiH_3 + H_2$

- Low density of SiH_2 radicals
  - Higher order radicals of silane are highly reactive with each other as well as the film surface and usually result in the production of poly-silane molecules, eventually forming dust in the plasma which have negative repercussions on film crystallinity as well as electronic performance [16].
  - Reactions of this kind take the form of $SiH_2 + Si_nH_{n+2} \rightarrow Si_{n+1}H_{n+4}$
  - These higher poly-silane molecules serve as nucleation sites for dust growth within the plasma.

- Low ion bombardment energy as determined by the sheath voltage / plasma potential
  - Reduces amorphization by high energy ion impact [24].
  - Ion impact has also be associated with positive effects such as annealing by abstraction of surface hydrogen [17], but negative amorphization is the dominant effect[25].

The above points can be summarised as follows: To produce nanocrystalline films a high relative population of atomic hydrogen in the plasma is necessary while maintaining a low sheath voltage to minimise ion bombardment energy and a low population of high order silane radicals which lead to dust production. There are several regimes

[24]Typical ion species associated with this amorphization include H^+, H_3^+ and SiH_3^+

[25]In addition non-ionised radicals can achieve, hydrogen abstraction effect without the effect of amorphization

under which these conditions can be achieved. In all cases plasma conditions and thus film properties are dictated by the rates of incidence for relevant chemical reactions, specifically those which contribute to the silane radical and and atomic hydrogen density. The primary dissociative processes occur as a result of inelastic collisions of parent molecules with electrons; bound electrons are promoted to un-stable and meta-stable energy levels temperately storing the energy. This energy is released when the molecule the decays to its electronic ground state by breaching the inter-atomic bonds and dissociating the molecule. Depending on the degree of excitation [26] the molecule will dissociate into different products. The following is a list of possible dissociative reactions in order of descending energy[18]:

- $SiH_4 + e \rightarrow SiH_4^* + e$
  - $SiH_4{}^* \rightarrow SiH_x^+ + (4-x)\,H$
  - $SiH_4^* \rightarrow SiH_x^- + (4-x)\,H$
  - $SiH_4^* \rightarrow SiH^* + 3H$
  - $SiH_4^* \rightarrow Si^* + 4H$
  - $SiH_4^* \rightarrow SiH_x + (4-x)\,H,\ (x < 3)$
  - $SiH_4^* \rightarrow SiH_3 + H$
- $H_2 + e \rightarrow H_2^* + e$
  - $H_2^* \rightarrow H^+ + H$
  - $H_2^* \rightarrow H^* + H$
  - $H_2^* \rightarrow 2H$

Knowing that the preferred plasma condition are those that produce high densities of SiH_3 and H it can be seen that a high frequency of lower energy excitations is conducive to this condition. The high density of low energy electrons produced by

[26] degree of excitation refers to the number of energy levels the bound electron has been promoted

VHF excitation can will therefore contribute to a desirable chemistry for nanocrystalline deposition. The relative density of silane and atomic hydrogen in the plasma can also be affected by secondary collisional processes; not involving energy transfer from hot electrons.

- Ion exchange: $SiH_x^+ + SiH_4 \rightarrow SiH_x + SiH_4^+$
- Ion - Molecule: $SiH_x^+ + SiH_4 \rightarrow SiH_3^+ + SiH_3$
- Neutral - Molecule: $SiH + SiH_4 \rightarrow Si_2H_5$
- Disproportionation: $Si + SiH_4 \rightarrow SiH_3 + SiH$
- Insertion: $SiH_2 + SiH_4 \rightarrow Si_2H_6$
- Recombination: $SiH_2 + H_2 \rightarrow SiH_4$
- Abstraction: $H + SiH_4 \rightarrow H_2 + SiH_3$

There are several models which attempt to explain the significance of atomic hydrogen density in nc-Si:H growth [11, 12, 18, 19], which we will introduce briefly here. Many of the processes described are shown in figure 1.6.

The surface mobility model [11, 12] asserts that the pacification of dangling silicon bonds at the growth surface is a critical factor in producing crystalline films because it enhances the mobility of precursors at the the surface. The film growth precursors are silane radicals; primarily SiH_3. Once produced by dissociation these radicals have a high degree of reactivity with the surface and on striking the surface have a high probability of forming a Si-Si bond and being incorporated into the solid. The higher the mobility induced by hydrogen passivation increases the chance that a given radical will encounter a crystalline nucleation site at which to bond. Rather than forming a bond at the nucleation site nearest to where they strike the surface, when the surface is passivated film precursors will have enhanced surface mobility and a greater likelihood to form a bond at a favourable nucleation site with lower strain. Since growth in the crystalline phase is favourable from this perspective, if a radical encounters a crystalline

bonding site, it is more likely to form a bond than at an amorphous site. This model is supported by the studies which observe reduction in film crystalline fraction when the substrate temperate is raised above 250° C[18] where hydrogen is known to thermally desorb from the growing surface[27].

The preferential etching model [13] asserts that atomic hydrogen impinging on the surface will sometimes break Si-Si bond, forming a silane molecule / radical and extracting silicon from the growing surface. This etching will preferentially break the weaker Si-Si bonds present in amorphous regions of the film. When another Si atom is deposited at this site the subsequent bond may be crystalline. While this model can explain why the crystalline fraction of deposited films is dependant on the atomic hydrogen density in the plasma it can not account for the initial transition from amorphous to crystalline growth regimes

The chemical annealing model [14, 15] asserts that atomic hydrogen impinging on a silicon film will result in reactions at the surface and within the bulk. Those reactions resulting in insertion and abstraction of hydrogen at silicon bonding sites are both exothermic. The resulting heat is dispersed locally, and in the amorphous regions structure will relax into a crystalline phase just as has been seen with thermal or laser annealing processes[20]. This model is supported by studies which expose a pre-deposited film to a "pure" hydrogen plasma and show an increase in the films crystalline fraction[21].

Traditionally the above conditions have been achieved by heavy dilution of the source gas with hydrogen. While this method is effective, it has disadvantages as well as limitations (chapter 2.1). In order to achieve the above conditions it is necessary to maximise the dissociation rate of incoming SiH_4 (and H_2) without significantly increasing the sheath voltage so as to prevent amorphization by ion bombardment.

[27]The thermal desorption of Hydrogen is the the combination of 2 hydrogen atoms that were previously passivating surface silicon bonds. This results in the emission of a H_2 molecule from the surface without the need for a chemical abstraction as demonstrated in Figure 1.6.

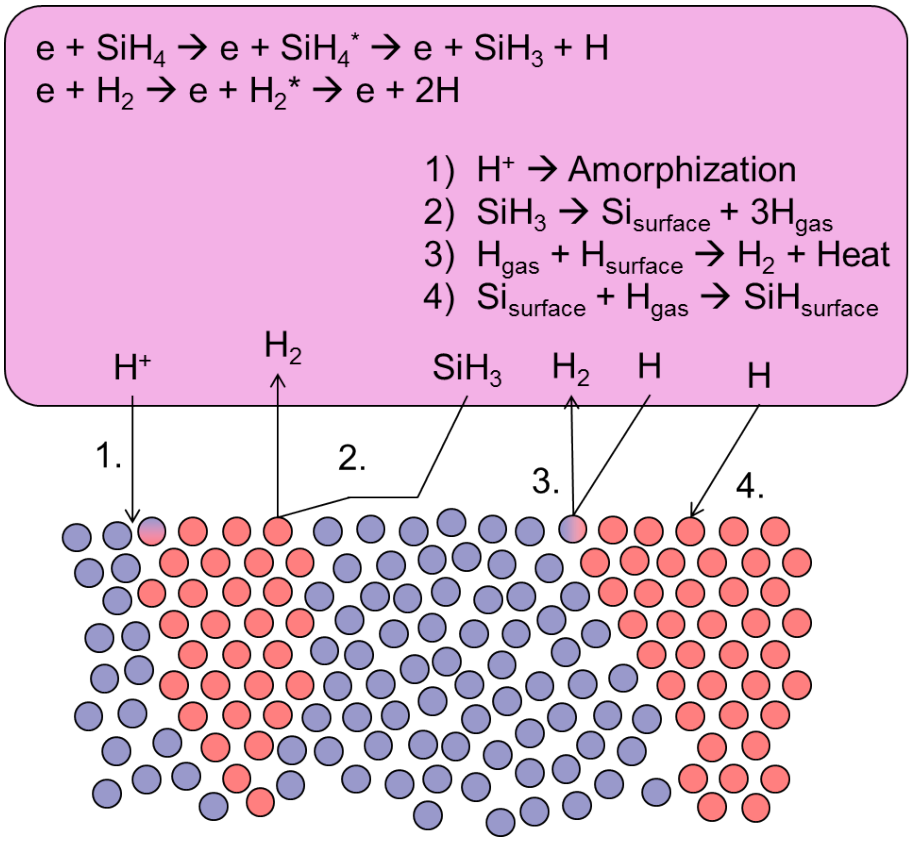

Figure 1.6: Illustrates the chemical processes involved in the PECVD of nc-Si:H. High electron density, low electron temperature and low ion bombardment give rise to a high rate of silane and hydrogen dissociation by both primary and secondary precesses. Representative, dissociative plasma reactions are included at the top. Surface reactions are displayed graphically and as a numbered list. 1. Amorphization by ion bombardment. Typical ion species associated with this amorphization include: H_3^+, and SiH_3^+., 2. nc-Si:H deposition due to high surface mobility 3. Chemical annealing by Hydrogen extraction 4. dangling bond passivation by hydrogen insertion.

1.4 Multi-tile CCP & the PSTLD

1.4.1 Multi-tile CCP

In plasma processing, whether it be in the semiconductor, thin film solar fields or elsewhere there is a continuing demand for either increase the surface area and/or excitation frequency. In semiconductor manufacturing one of the major research challenges is to advance from 300 mm to 450 mm diameter wafers while maintaining the process performance and stability offered by VHF triode sources[22, 23]. In the thin film solar industry substrates exceeding $1\,m^2$ are common and the advantage of VHF excitation capability is becoming apparent as it shows the ability to deposit nc-Si:H at high rates[28]. Many studies have investigated the effect of excitation frequency on plasma parameters and any subsequent improvements in process quality[4, 5, 24–28]. Unfortunately it is apparent that achieving VHF excitation and large substrate coverage simultaneously pose significant technical difficulties. Traditionally, "quarter wavelength" effects have been compensated for by altering the power feed geometry [29] but as both frequency and area technology frontiers are expanded this is no longer sufficient.

In order to explain quarter wavelength non-uniformities the power delivery mechanisms inherent to CCP sources will be explored. Consider the path along which current flows in a traditional parallel plate CCP chamber (Figure 1.7). Since the skin depth, $\delta = \sqrt{\frac{2\rho}{\omega\mu}}$ of RF and VHF radiation in metals is significantly smaller than the scale of the electrode thickness electrical currents flow along the surface of the electrode.

The alternating voltage on the electrode surface will drive displacement current across the capacitive sheath. Currents flowing horizontally across the electrode face will induce image currents in the plasma adjacent to the sheath. Currents flowing, vertically around the electrode edge will induce a magnetic dipole between the electrode and the chamber, which may in turn drive inductive currents in the plasma[29]. Displacement currents scale with the potential difference across the sheath divided by the sheath

[28] Manufacturers have produced panels using 60 MHz and 100 MHz excitation

[29] Given that in conventional CCP reactors the plasma is localised to the area in front of the powered electrode, dipoles outside this area will have minimal influence on the plasma profile, this is not the case for segmented electrodes

impedance,

$$I = \frac{V}{z} \tag{1.22a}$$

$$z \propto \frac{1}{f_{RF}} \tag{1.22b}$$

while inductive currents scale with the skin depth of the plasma $\delta_s = \frac{c}{\omega_p}$. Electrons can be heated directly by the oscillating RF E-field in the sheath, while both capacitive and inductive currents will heat electrons adjacent to the sheath edge.

$$P_{bulk} = (I_{cap} + I_{ind})^2 R_{plasma} \tag{1.23}$$

To examine the relative strength of these power coupling mechanisms consider the magnitude of the current and voltage across the electrode face. Since the electrode has no direct physical connection to ground[30], no direct current can flow and thus charge carriers behave as if they meet open circuit termination. The point of effective electrical termination is the point on the current path which is furthest from the power supply. Since the current path wraps around the edges of the electrode this point is is on the electrode face opposite the electrical connection on the back side. The forward and backward propagating RF waves will interfere to form a standing wave with a voltage maximum at this point [30].

In order to examine the effect of this standing wave the standing wave wavelength (λ_{sw}) should be compared to the electrode diameter (d_{source}) (Figure 1.8). The standing wave wavelength can be calculated as follows:

$$\lambda_{sw} = \frac{\lambda_{RF}}{\varepsilon_p} \tag{1.24}$$

where ε_p is the plasma permittivity and $\lambda_{RF} = \frac{c}{f_{RF}}$ is the vacuum wavelength of the power source and f_{RF} is the RF frequency.

[30]In this instance a direct physical connection means a direct conductive path. Despite the lack of a physical connection, AC current can still flow to ground by capacitive and inductive coupling.

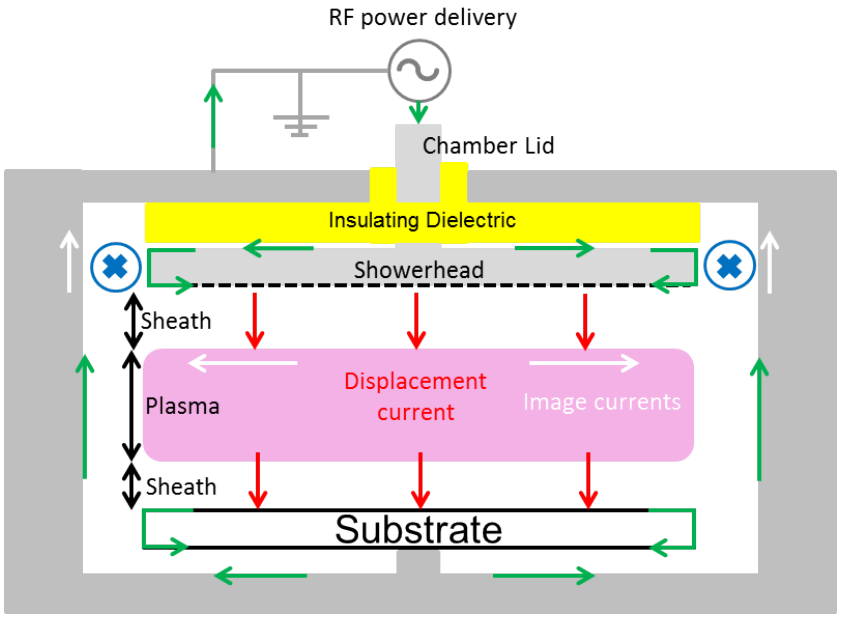

Figure 1.7: Showing the power coupling mechanisms inherent to a conventional parallel plate CCP. The current path through the electrode; in green, follows the surface of the powered electrode. Capacitive displacement currents, inductive image currents and magnetic dipoles are shown; in red, white, and blue respectively.

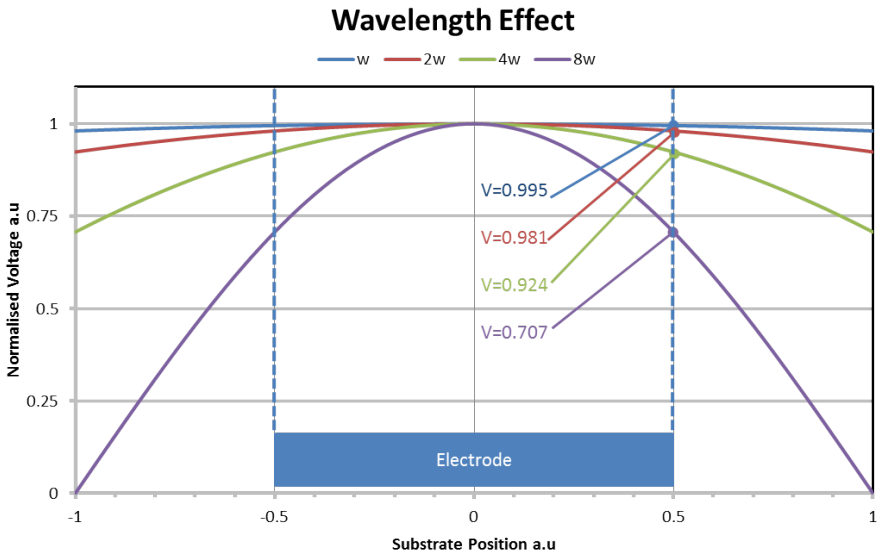

Figure 1.8: Illustrates the voltage uniformity across an electrode for various excitation frequencies. The frequencies were picked so that $\frac{\lambda}{4}$ of the highest frequency is equal to the electrode diameter. While all frequencies have a maximum normalised voltage of 1 at the tiles centre the normalised voltages at the tile edge (± 0.5) are marked explicitly

If the standing wave wavelength is long compared to the electrode dimensions then the voltage can be considered effectively constant at any point in time. Assuming a cylindrical geometry[31] as well as this constant voltage the current profile across the electrode will also be described. Since voltage is just a representation of space charge density, consider the necessary charge to induce constant voltage across the substrate. Beginning form a point in time where the voltage is 0 and considering the current flowing onto the surface from the edge. All of the carriers necessary to charge the electrode must flow through a cross sectional area around the circumference of the electrode to/from the generator. The area through which the current flows can be expressed as follows, $c = 2\pi r\delta$. Moving towards the centre of the electrode; the number of carriers needed to charge the smaller areas at the centre is smaller. The net current is proportional to the surface area of the electrode contained by that circumference $A = \pi r^2$. As such the current flowing along the surface increases linearly as a function of radius.

$$I \propto \frac{\pi r^2}{2\pi r\delta} = \frac{r}{2} \tag{1.25}$$

Quantifying the current profile for non-uniform voltage profiles is possible but non-trivial; it is worth mentioning however, that the current profile will remain edge dominant. The strength of image currents will, therefore be greater at the electrodes edge, the strength of this non-uniformity will depend on the skin depth as well as the relative size of the electrode and the inter-electrode gap.

Displacement currents will be the dominant power coupling mechanism across the electrode surface. When using larger electrode dimensions and higher excitation frequencies the $\frac{\lambda_{sw}}{4}$ becomes comparable to the electrode diameter; voltage and current non-uniformities become significant. This will lead to unequal, power delivery across the plasma, specifically: capacitive coupling will dominate power deposition at the tile centres while inductive coupling will dominate at the tile edges. This in turn introduces process non-uniformities across a substrate.

Multi-tile CCP sources offer a solution to the issue of voltage non-uniformities

[31] 2 circular electrodes, forming a cylindrical volume where the plasma will be formed

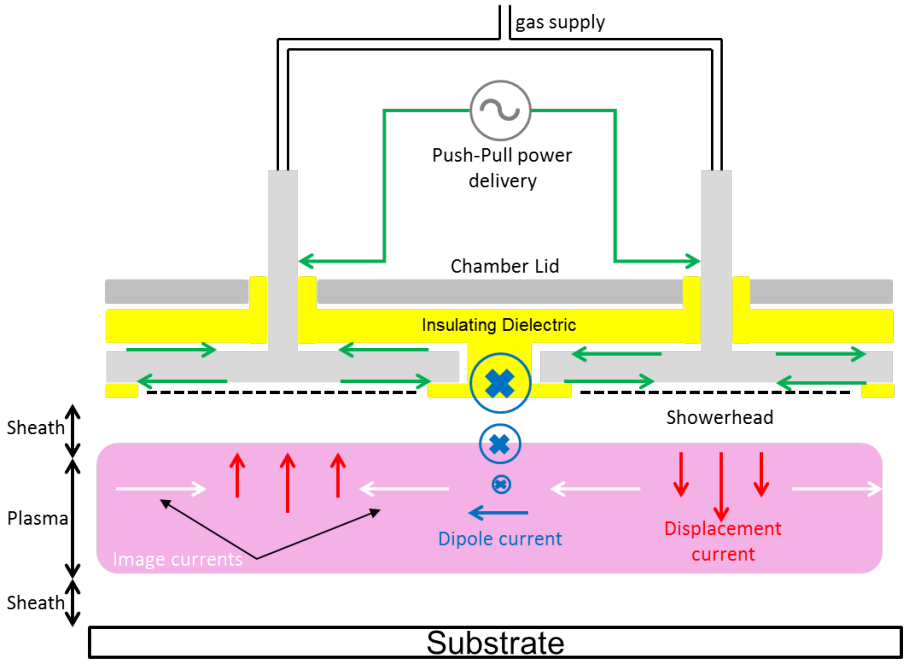

Figure 1.9: Power deposition in a push-pull multi-tile CCP source. The figure shows a single unit cell as section of a larger array of tiles each exciting plasma locally to provide total plasma coverage over the desired substrate area

caused by standing wave effects. By dividing the powered electrode into tiles and providing an equal and independent power feed[32] to each tile VHF/UHF excitation can be used to produce uniform plasma over much greater areas, a full description of the MAMELUKE source can be found in section 3.1. In order to provide an independent power feed to each tile a suitable power splitter is required. The PSTLD which is described in section 1.4.2 provides independent push-pull power to each unit cell (2 adjacent tiles) of the MAMELUKE source.

Multi-tile CCP sources operated in differential power delivery mode display much the same current behaviour as conventional CCPs with some key differences

- Magnetic dipoles produced between the tiles are stronger and are located at regions facing the plasma rather than at the plasma edge.

- VHF excitation leads to high electron densities decreasing the penetration depth

[32]It is advantageous to to electrically isolate the electrical connection for each tile as opposed to connecting one to all tiles in parallel

of the plasma, strengthening all inductive current effects.

- Zero, or very little net current flows through the plasma to ground. The push-pull nature of the PSTLD means that for each tile driving "positive" current, into the plasma it's neighbour is 180° out of phase driving negative current, out of the plasma. As a result the source behaviour is independent of the electrical path to ground and not sensitive to effects resulting from asymmetrical or imperfect grounding. Furthermore push-pull sources located in different chambers with different grounding can more readily be compared.

1.4.2 The PSTLD

The Power Splitting Transmission Line Device (PSTLD)[31] (Figure 1.10) consists 2 concentric metal cylinders forming a co-axial transmission line which is terminated by an electrical short at the end furthest from the input. Several coupling loops are located in the cavity between the 2 cylinders. Each loop produces a pair of outputs which carry a differential, push-pull current signal (Figure 1.10).

RF current is driven along the centre conductor and back along the grounded outer. A voltage null (node) is coerced at the short between the 2 conductors, which defines the standing wave which will propagate back along both conductive surfaces towards input. If the length of the co-axial transmission line is at least as long as one quarter of the electrical wavelength ($\frac{\lambda}{4}$) then the full range of electromagnetic (current, voltage, magnetic field) amplitudes; from node to the first anti-node will be evident along the length of the conductors.

Figure 1.11 depicts the Voltage, Current, and Magnetic Field as a function of position along the PSTLD. The current standing waves on opposing surfaces (inner and outer conductors) are 180° out of phase and thus contribute constructively to an azimuthal magnetic field in the cavity. The subsequent introduction of a secondary coupling loop to intersect this magnetic flux allows power to be transmitted inductively

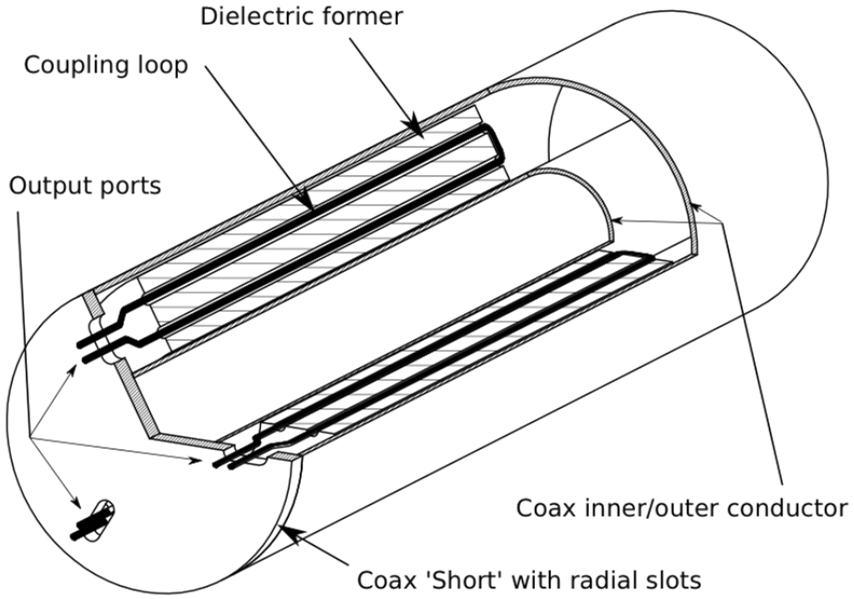

Figure 1.10: The internal structure of the PSTLD. Secondary coupling loops, made of copper are inserted into the cavity between the powered coaxial surfaces perpendicular to the azimuthal magnetic field shown in figure 1.10. The coupling loops are held by a dielectric former and further insulated by quarts tubes. Slots are cut in the end-plate which shorts the outer and inner conductors of the transmission line, this allows for the output of the coupling loops to be fed through and delivered to the individual tiles by twisted pairs of copper wire. Credit: Neil O'Hara

and an EMF is set up in the secondary loop following Faradays Law.

$$EMF = -\frac{d\Phi}{dt} \tag{1.26}$$

An arbitrary number of secondary coils can be introduced to allow for the equal splitting of the power to an arbitrary number of outputs. The secondary windings are fed through a slot in the transmission line short (figure 1.10); while the wire remains unbroken no further power coupling occurs after this point and it is called the output. Power is delivered to the tiles of the source by twisting the ends of the output pairs of 3 mm diameter copper wire. The voltage of the 2 terminals of each winding oscillate in a push-pull configuration; the voltages alternate 180° out of phase with each other. One output from the PSTLD powers a single unit cell (2 tiles) of the multi-tile source.

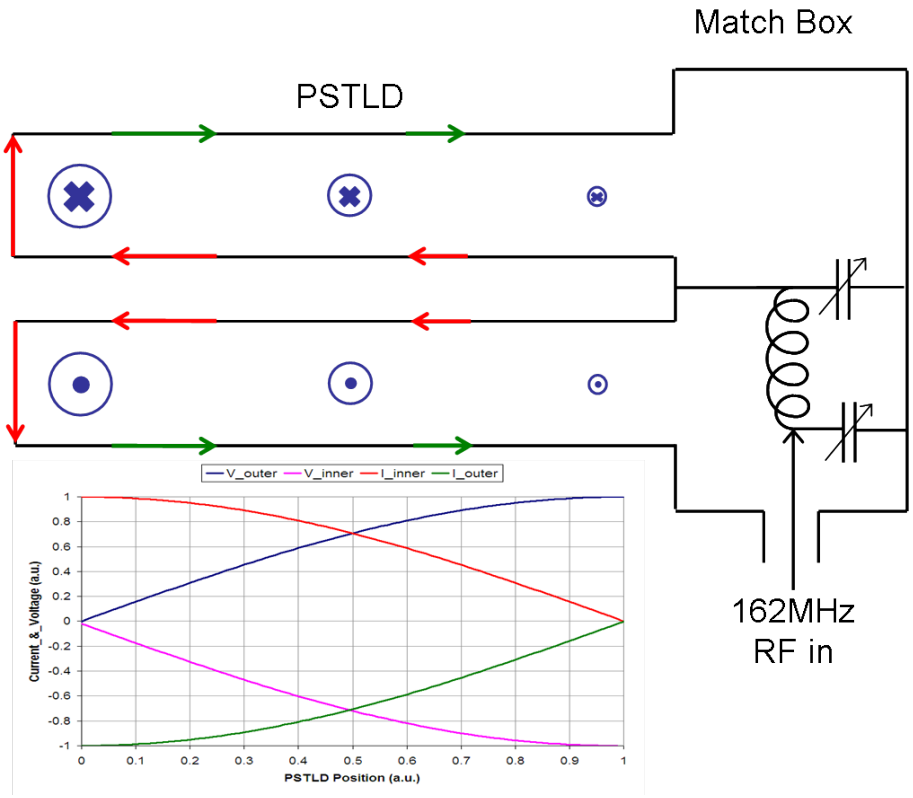

Figure 1.11: Cross section of of the power matching and splitting apparatus for the MAMELUKE source. 162 MHz power is input to the matching unit whose impedance can be tuned so as to maximize the power delivered to the plasma. The current paths at one point in time are depicted by arrows flowing along the surfaces of the coaxial transmission line as part of the PSTLD. In addition the graph below depicts the relative current and voltage along the inner and outer conductors. Finally the azimuthal magnetic field is depicts by vectors perpendicular to the plane of the page the magnitude of these vectors is represented by the size of the symbol.

Chapter 2

Previous Work

2.1 Nano-crystalline Silicon

2.1.1 Deposition

Hydrogenated nano-crystalline silicon (nc-Si;H), also referred to in the literature as microcrystalline, polycrystalline, or multicrystalline silicon[1] was first deposited at low temperature by *Veprek et.al* in 1968[32] by "chemical hydrogen plasma transport" and since has been an extensively researched material for optoelectronic applications. Specific applications of interest include the production of thin filim transistors (TFTs) which see application in thin film display technology[33–35]; research is conducted most extensivly for the production of nc-Si:H absorbing layers in thin film photovoltaic technologies[34, 36–47] as will be explored in section 2.1.2.

The ability to deposit nc-Si:H at low processing temperature using processes such as PECVD and hot wire chemical vapour deposition (HW-CVD) is of particular interest. In this instance, low temperature refers specifially to a substrate temperature of less than 250 ° C. This is far below the melting temperature of silicon; usually temperatures exceeding 600° C are required for the growth of ordered, crystalline silicon[15]. Even after extensive investigation the exact nature of low temperature synthesis mechanisms

[1]Depending both on the average crystallite size and popular nomenclature at the time

continue to be debated. While this process remains only partially understood it is one of the main attractions of the material. Low temperature synthesis lowers the production cost as well as introducing a greater choice of suitable substrate materials; specifically deposition on glass[2] or even flexible plastic for roll-to-roll production[41, 47].

The primary advantages of nc-Si:H when compared to amorphous material are its high electrical conductivity[48], low defect density, as well as its lower band gap compared to a-Si:H. In addition it maintains the advantages of all silicon based devices, abundance of raw material, durability and non-toxicity[46, 49]. An advantage specific to solar applications is that nc-Si:H is not susceptible to light induced degradation a.k.a. the StaeblerWronski effect (SWE)[7], which limits the long term efficiency of solar cells manufactured with an amorphous silicon (a-Si:H) absorbing layer[50, p. 21]. The band gap of nc-Si:H is lower than amorphous material allowing for collection of long wavelength light that an amorphous layer will not absorb. As a result it became an attractive material to be incorporated in multi-junction cells[38, 41, 44, 51] for the collection of a broader spectrum than any one absorber can achieve alone.

While the growth mechanism of nc-Si:H are not fully understood several useful growth models have been thoroughly explored in the literature. The surface mobility[11, 12], preferential etching[13] and chemical annealing [14, 15] models attempt to examine the dependence of crystalline growth on atomic hydrogen density. Other growth studies concentrate on the significance of other factors, including the ion bombardment energy [17] and the substrate topography[51].

2.1.2 Solar Application

Originally nc-Si:H was only utilised for the window layer in otherwise amorphous cells[48] but fully nc-Si:H p-i-n cells were finally produced in the late 90s[52]. Once this was achieved the primary challenge in the manufacture of nc-Si:H based solar panels became it's band gap. Since the band gap is indirect, it has a lower coefficient

[2]glass substrates allow for the production of display and/or solar products at low cost and over large surface area. It has also been utilised in the manufacture of both a-Si:H and nc-Si:H thin film solar technologies

of absorption (α) than a-Si:H[3]. As a result the intrinsic absorber layer must be made significantly thicker than an amorphous equivalent. Approximately 1 micron thickness of nc-Si:H is required to increase the path-length of photons in the layer and achieve an acceptable absorption of light. The resulting deposition time for each panel is much longer (Section 1.3). The increased cost of producing thick layers makes nc-Si:H solar a less attractive alternative even considering the advantages in stability and efficiency. For this reason the bulk of research in improving nanocrystalline silicon has been focused on increasing the deposition rate, without compromising the materials properties [19, 42, 44, 45, 53–56].

The deposition rate is limited by 2 major side-effects encountered using the conventional PECVD process[4], ion bombardment and powder formation both of which are explored in section 1.3. The primary conclusion from the above papers was that high densities of atomic hydrogen and low gas phase SiH_4 density in the plasma were responsible for the growth of of device quality nc-Si:H[5]. As a result most processes were developed with a heavy dilution of hydrogen gas and as the silane flow was increased to maximise deposition rate, the 13.56 MHz power was increased to encourage high dissociation rates. Both amorphization and powder formation were encountered at higher power density and thus limited the maximum silane flow, and consequently the maximum deposition rate.

- The use of lower RF frequencies limited the achievable silane dissociation rate because at the higher powers necessary to dissociate high flows the the sheath independence and thus the ion bombardment energy were too high and amorphized the film through high energy impact.

- In addition the high RF power density was further limited by the need to avoid multiple dissociations of silane, specifically the production of SiH_2 radicals, which

[3]Indirect band-gaps require a 2 particle (photon + phonon) to create each electron-hole pair

[4]In this context, conventional refers to the combination of of heavy hydrogen dilution and 13.56 MHz excitation in the majority of industrial PECVD processes

[5]Processes with too low a density of atomic hydrogen resulted in layers of a-Si:H or crystalline material with high defect density

drive powder formation in the plasma[16] severely compromising the electronic properties of a film.

- Heavy hydrogen dilution of the source gas dramatically increases the total gas flow through the system and, for a constant pressure reduces the residence time of each molecule in the plasma volume. As a result the same dissociation rate of silane will achieve a lower steady state density of atomic hydrogen and a higher steady state density of silane. The high total flow rates require higher power density at lower silane flow to produce nc-Si:H material, thus limiting the achievable deposition rate (Chapter 1.3).

The results of recent studies have shown that the conventional, heavy dilution regime, while conducive to crystalline growth is limited in terms of deposition rate. The alternative, high depletion regime has been shown to be capable of far superior depositions rates[19, 57]. These studies are preformend using some combenation of: low hydrogen dilution, high process pressure, and VHF excitation to achieve high atomic hydrogen density and high silane depletion, while avoiding high energy ion bombardment or silicon dust particles. In these studies a significant fraction if not all of the gas phase hydrogen is produced by a combination of dissociative plasma processes and liberation of hydrogen during deposition. In addition, high sheath potential is either avoided by the use of VHF and/or compensated for by increased collision rate in the sheath as a result of high gas pressure[58].

The reduction in sheath impedance with VHF excitation allows for an increase in the electron density of the plasma while maintaining a low sheath voltage so as to prevent amorphization by high energy ion bombardment[25, 26, 28, 59]. In summary, the recent research has suggested that best way to achieve high deposition rates of device quality nc-Si:H is through a combination of VHF excitation and high pressure [42, 58, 60, 61].

2.1.3 Analysis by Raman Spectroscopy

Since nc-Si:H was first deposited in the late 60s determining a reliable and repeatable diagnostic of crystalline fraction has been a source of much study. Many techniques have been used to analyse and compare films produced with different methods (PECVD, HW-CVD, ICP etc.) or often with the same method but for different deposition conditions (Power, Pressure, Temperature etc.). Diagnostics used include, but are not limited to: X-ray diffraction (XRD)[10, 62], scanning electron microscopy (SEM)[8], transmission electron microscopy (TEM)[40, 63]. These techniques often offer interesting insights into the films examined but to date have only been able to offer qualitative data on the crystalline fraction of the material[6].

Examination by Raman Spectroscopy has become a standard however and while the raman crystalline fraction (RCF), X' measured is not an exact measure of the fractional crystalinity as explained in section 3.2 it is a repeatable quantitative measure indicative of the volumetric crystalline fraction (VCF). As a result the technique has been utilised in various studies investigating nc-Si:H[65–69]. While concerns about the applicability of Raman spectroscopy have been raised they are primarily with the error introduced by variations in temperature and substrate bias resulting strained bonds[62].

The equation used most frequently to analyse the crystalline fraction of nc-Si:H was first introduced by *Tsu et.al.* in 1982[70]. While the majority of studies still utilise this method several researchers have adapted and improved upon the techniques approaching the problem from differently. In [68] *Ledinsky et.al.* argue against the use of more than 2 peaks in any fitting technique, contending that there is no physical effect that an intermediate peak can be attributed to. Instead they argue in favour of a model where Raman emission between the amorphous and crystalline peaks is caused by asymmetrical broadening of the crystalline peak. In addition the authors observe the different RCV values calculated for different light frequencies[68].

[6] XRD being the exception in the case as it can offer a quantitative comparison of crystalline growth in different configurations, specifically: (1,1,1), (2,2,0) and (3,1,1). Attempts have also been made in the literature to extract the bulk crystalline fraction from diffractogramms[10, 64] it remains rare and methodologies often differ

2.2 VHF Plasma and Wavelength Effects

Many researchers have recognised that VHF-PECVD is a viable way to improve the deposition rate of nc-Si:H. Previously, VHF excitation has been researched for the purposes of a-Si:H production[71–73]. Previous to this, the advantages of VHF excitation have been explored extensively outside of the field of thin film silicon PECVD and solar manufacturing. In the the field of micro-electronic / semi-conductor processing the benefits of VHF excitation have been extensively implemented.

In semi-conductor manufacturing VHF excitation is often deployed in dry-etch processing using dual frequency CCP sources commonly refered to as triodes[6, 23, 74–77]. By powering the top electrode with with higher frequencies and the substrate electrode at conventional 13.56MHz or lower it is possible to partially de-couple and separately control the electron density and the the ion impact energy[6, 78]. The independent control of these process parameters has been shown to become stronger for greater difference between the higher, excitation frequency and the low, bias frequency. Furthermore the chemistry of the plasma properties become more attractive with further increases in excitation frequency. These frequency effects were thoroughly explored by *Samukawa et.al.* with the use of a spoke-wise antenna source[4, 79–81]

While the process of dry-etching is, in ways the opposite of PECVD it should be noted that the desirable gas phase chemistry reactions are similar in nature to those of a silicon PECVD process. A desirable chemistry is one with a high density of primarily low order radicals[82]. The high energy tail seen in the EEDF of VHF excited plasmas allows for the production of high electron density, low electron temperature conditions required for this kind of process[81]. Despite the successful utilisation of VHF plasma processing it is apparent that existing technology is not forward compatible to the larger 450 mm substrates of next generation manufacturing as wavelength effects continue to be accentuated at these larger dimensions[7].

Higher frequencies (100 MHz) have shown limited success in being deployed in

[7]Wavelength effects are apparent when processing 300 mm substrates using VHF excitation. To date these have been compensated for but the increase in electrode size is expected to exacerbate these effects to the point that they cannot be compensated for

manufacturing at the large surface areas required for solar and display manufacturing ($> 1m^2$). Yet it remains clear that in order to have flexibility in both excitation frequency and substrate area of CCP processes, suitable hardware changes are necessary. Various Options that have been put forward include:

- Ladder-shaped electrodes [83]
- Multi-hollow-cathode electrodes [58, 61]
- Graded conductivity electrodes[84]

A further introduction of these technologies is given in Chapter 2.3.

2.3 Multi-Tile sources & Segmented electrodes

While it has been clear since the early 1990s[25] that the excitation frequency is an important parameter in the PECVD of solar materials as well as other plasma processes. A solution to wavelength dependent non uniformities has remained an open are of research since then[22, 25, 29, 69, 77, 85].

In the field of semiconductor manufacturing as the trend of increasing excitation frequency has progressed it has encountered issue of wavelength dependent non-uniformities but has been able to compensate for them primarily due to the relatively small substrate diameter (300 mm) of CCP sources in this industry. As the industry progresses, however it has become apparent that existing technology is not forward compatible to the next generation of larger area substrates (450 mm) as explained in the previous Chapter (2.2) This prompted extensive research in this field also.

Apart from the alternate source designs described in section 2.2 various attempts have been made to sensibly adapt existing, well understood CCP technology to compensate for voltage non-uniformities.

Initially it was sensibly observed that the standing wave effect can be controlled by altering the positioning of the power connection point on the reverse of a powered electrode. That is to say that the voltage maximum will be located at the point furthest from the connection point. In [29] *Sansonnens et.al.* investigate the effect of moving the connection point of both powered and grounded electrodes as well as the possibility of splitting the connection to multiple symmetrically arrayed points in parallel. It was concluded that the ideal position for a single connection point was at the centre of the electrodes' back side (not the plasma facing side).

Subsequently similar studies were conducted on the effect of a curved electrode face with a dielectric lens on the voltage profile across a powered electrode[86, 87]. It was found that the standing wave effect could be compensated for by shaping a cylindrical electrode with a Gaussian profile. Unfortunately this solution is dependent on a consistent plasma refractive index and as such has only limited flexibility once implemented.

Previous studies have also been conducted investigating the applicability of segmented or divided electrodes for application as a 450 mm source for semiconductor applications[88]. This source concept differs from the one presented here in that all electrodes are driven from the same power supply without a splitting device such as the PSTLD (section 1.4.2) which allows for 2 contrasts to be drawn between the sources:

- The tiles are not electrically isolated from each other which can have the side effect of a localised breakdown, where plasma is produced in front of only one of the electrodes.
- Adjacent tiles are not operated in a push-pull configuration and as such current is still driven through the substrate to ground.

Chapter 3

Experiment

3.1 Mameluke Source

All experiments described in this thesis were preformed on the MAMELUKE multi-tile PECVD source. MAMELUKE has a total surface area of 720 mm × 600 mm (Figure 3.1) and is contained within a grounded vacuum chamber. Because of the complexity of describing such a multifaceted piece of equipment thoroughly the following aspects of the source will be described separately: 1. The source or upper electrode; 2. The back side, and external components of the chamber; and 3. The front side components necessary to achieve a PECVD system, including the lower electrode (susceptor) and substrates. First the design and composition of the multi-tile upper electrode will be described, followed by the details of the back and front side.

The upper electrode is divided into 16 individual electrodes each of which has dimensions of 300 mm × 80 mm, for the purposes of this document, these segments will be referred to as tiles. Each tile consists of: a front surface, which faces the plasma and allows for the gas delivery through a shower-head[1]; a middle, which is surrounded by insulating dielectric, glass fibre filled peak; and a shank feed-through which protrudes from the chamber lid allowing for gas and power to be delivered externally. There is a

[1] in this instance a shower-head refers to an array of holes drilled in the electrode faceplate, small enough so as not to perturb the electrostatic behaviour of the surfaces while large enough to prevent significant pressure differential across the boundary

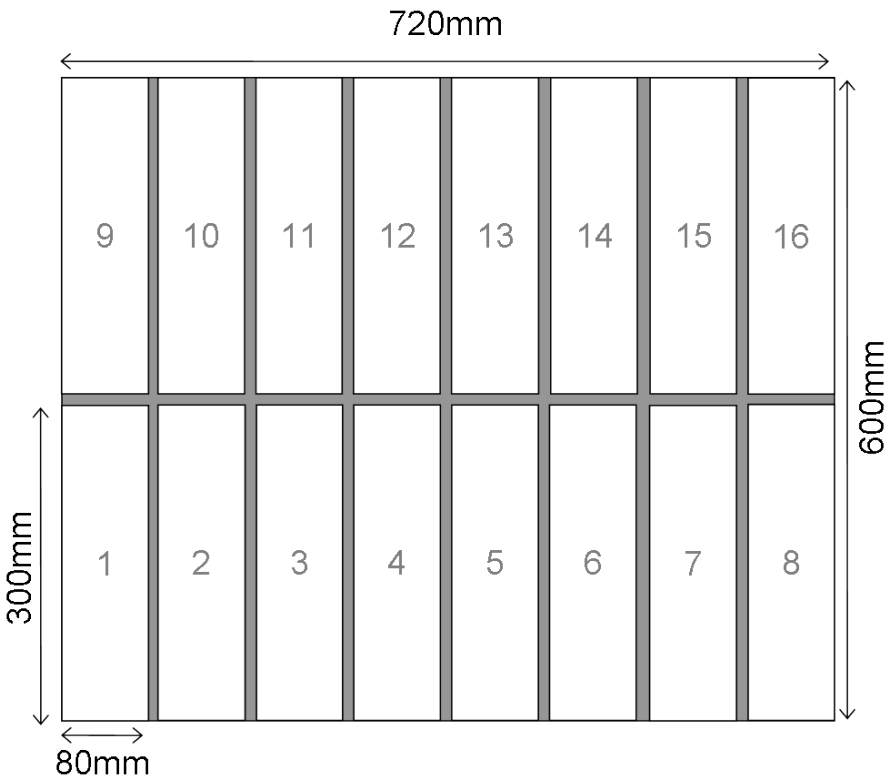

Figure 3.1: A basic schematic of the MAMELUKE source from a "plan" or top-down perspective. The schematic includes including the primary dimensions of the upper segmented electrode as well as the dimensions of individual component tiles. The numbering convention for referring to tiles is included and substrate positions will be referred to using this convention through out this document

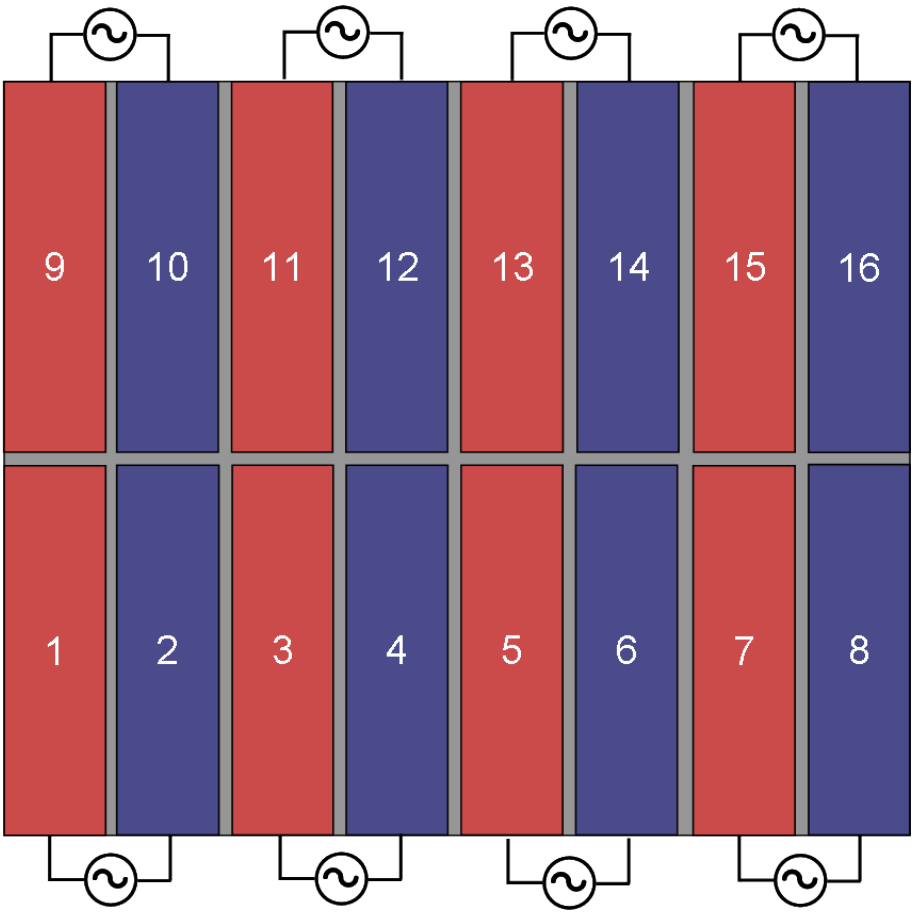

Figure 3.2: A layout of the MAMELUKEsource including showing the tile numbering scheme (1-16) for the individual tiles as well as the polarity of each of the tiles with respect to each other. All tiles of the same colour, red/blue are at the same phase and 180° out of phase with the opposite colour.

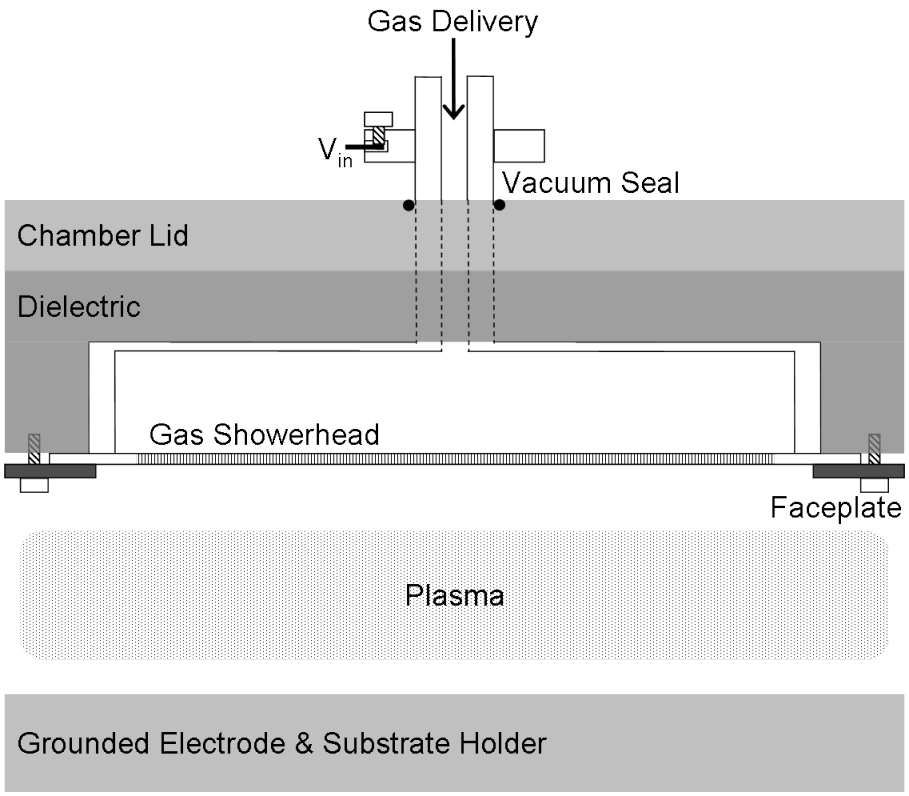

Figure 3.3: A schematic of a single tile within the MAMELUKE source. This figure demonstrated the power and gas delivery to the plasma source. Each tile is surrounded by an insulating dielectric and separated from neighbouring tiles by a ceramic faceplate. Note: This schematic does not illustrate the exact method of vacuum seal between the electrode shank and the chamber lid.

vacuum seal between the chamber lid and the shank allowing for power and gas delivery to be at atmospheric pressure (Figure 3.3). Considering 2 adjacent tiles in the source, their relative position and orientation are such that their 300 mm sides are aligned and adjacent; between these tiles is the same electrically insulating dielectric that separated each electrode from the grounded chamber. In addition an insulating alumina face plate is attached to the inter-electrode peak and overlaps the plasma facing edges of the 2 neighbouring tiles. For the purposes of this document we will refer to such a collection of 2 tiles, the inter-tile dielectric and faceplate as a unit cell of the source (Figure 3.4). The 16 tiles which make up the source can also be considered as 8 unit cells.

The back side of the MAMELUKE tool consists mainly of the apparatus to enable delivery of power and gas to the powered upper electrode. Given the multi-tile nature of

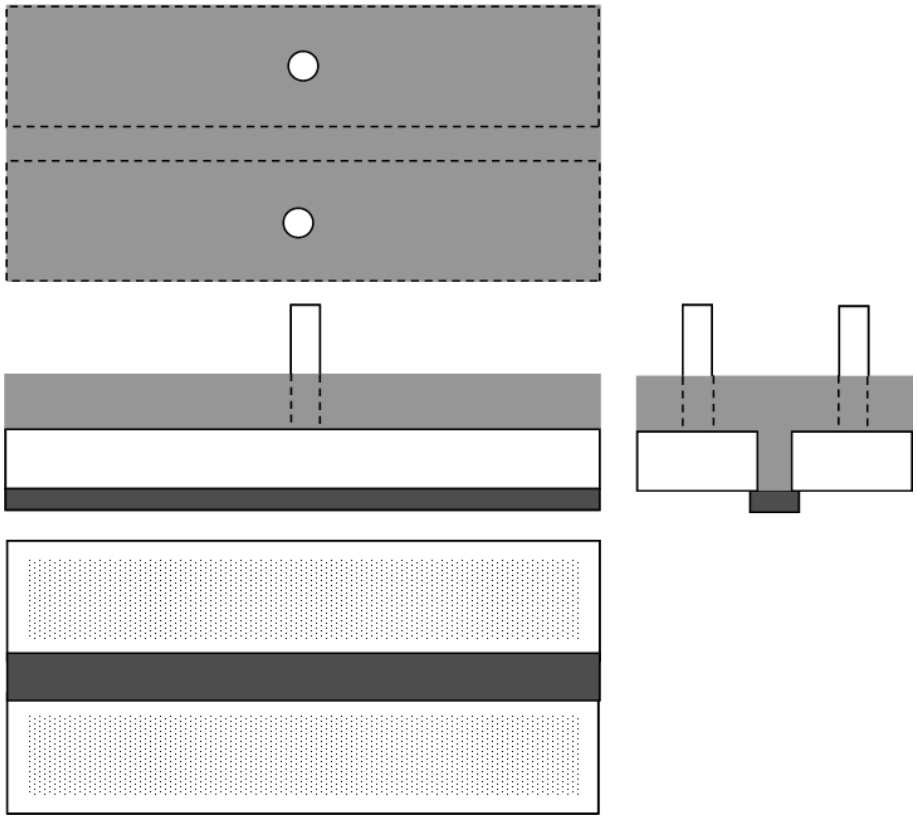

Figure 3.4: 2 neighbouring tiles; also referred to as a unit cell are shown. This figure depicts the unit cell electrodes as well as the necessary insulating components.

the source there are several unique design elements involved in achieving this[2]. 162 MHz RF power is produced by an Advaced Energy Ovation162 Generator. This power is split and delivered to the individual tiles by a PSTLD power splitter the theory of which has been explained in chapter 1.4.2. Between the PSTLD and the RF generator there is a custom, high frequency matching unit with a π configuration; the combination of two variable capacitors with an inductor as seen in Figure 1.11, allows for the impedance of the system to be tuned so as to minimize the power reflected to the generator.The excited plasma is a component of this system the impedance of which will depend on various experimental factors. It is therefore necessary to be able to compensate and minimize reflected power for all experimental conditions making a tunable match, with variable capacitors necessary.

Equal gas delivery to all of the individual tiles is achieved by having a single gas feed which containes the premixed gas combination as determined by separate mass flow controllers (MFCs) upstream. Adjacent to the back side of the chamber lid, the gas-line successively is split in 2 [3] until a symmetric array of 16 poly-line feeds connect to each of the electrode shanks. The conductance of each branch of the gas delivery is designed to be equal, specifically, the length of tubing from the first division to each tile is the same. Under the assumptions that each line is of equal inner diameter, and that the pressure is equal at the face of each tile this should ensure equal gas delivery across the source. The use of poly-line as opposed to stainless steel gas line, in the distribution of gas has two advantages, primarily as an insulator it isolates the gas delivery line from RF exposure[4], secondarily the flexibility of the poly-line allows for ease of instillation in a space which is already crowded with the twisted pairs used for the RF power delivery.

The rest of the process chamber consists of the substrate and susceptor as well as the pumping apparatus. The substrates in MAMELUKE are the same dimensions as the

[2]The segmented nature of a multi-tile source requires equal delivery of power and gas to each powered tile

[3]each tile will have 4 t- shaped splits between the shank and the original mixed gas line

[4]because the gas delivery line is connected directly to the electrode shank (Figure 3.3) a metal tub would provide an alternate electric path for the push-pull electric current to travel between tiles

upper electrode, 600 mm ×720 mm . These substrates are glass coated in a transparent conducting oxide (TCO) such as indium-tin oxide (ITO) or Silver oxide. The substrate is held on a large aluminium heater block; the height of which is adjustable and driven my a stepper motor. The temperature of the substrate is monitored and controlled by a watleau thermostat and a thermocouple, the position is monitored using a Honeywell linear potentiometer. Under the perimeter of the substrate there is a metal frame which is used for the purpose of lifting the substrate on & off of the movable suseptor and carrying it to & from the load-lock. The lift ring has a perimeter of skirts which are designed to align with matching skirts at the upper electrode for the purpose of directing the process gas to flow through the narrow ends of the substrate before exiting the chamber though an iso100 port connected to an edwards ih80 dry pump equipped with a roots-type supercharger. Between the chamber and the pump there is a butterfly type throttle valve which allows for the fine adjustment of the pumping speed which controls the process gas pressure and when coupled with a MFCs the gas residence time in the plasma.

3.2 Raman Spectroscopy

Raman Spectroscopy is a spectroscopic technique which takes advantage of a phenomenon during the process of Rayleigh Scattering. In order to give an adequate explanation of the process it is therefore necessary to begin by introducing Rayleigh Scattering. Rayleigh Scattering is the elastic scattering of light by atomic or molecular entities[5], it is the absorption and re-emission of electromagnetic energy. Rather than directly exciting rotational, vibrational or electronic energy levels of the a molecule, Rayleigh scattering occurs when the electromagnetic field of the incident photons polarises a molecules local charge density such that it acts as an electric dipole, which then absorbs the photon and oscillates in resonance with the incident light frequency. The molecule is now said to be in a virtual state[6]. The molecule then, quickly relaxes into a stable state which results in the re-emission a photon with the same frequency as the incident radiation. Each individual molecular dipole is a secondary source of radiation. The re-emission of phonic radiation can have many directions and given that there are many such secondary sources in a given sample the resultant emission is inherently diffuse.

Rayleigh scattering is the primary phenomenon [7] behind blue skies and red sunsets. Given that sunlight is a broadband light source it appears white when observed directly. When this mixture of light frequencies reaches earth it is scattered by the gases that make up atmosphere. Given that Rayleigh scattering preferentially scatters light of higher frequencies light near the blue end of the visible spectrum will be scattered while those towards the red colours will penetrate further un-scattered. The penetration depth (σ_s) of radiation in a given sample is known to be inversely proportional to the fourth power of the wavelength. As a result the light we observe directly will have less blue light while the light we observe indirectly, or "sky light" will appear be blue. In

[5]for the purposes of this discussion we will discuss molecular scattering only

[6]by this it is meant that while energy from the incoming photons has been absorbed, the molecule is not in any of its natural, excited energy states; rotational, vibrational, or electronic and as such it is unstable. The absorbed energy usually exceeds that needed to excite any of these natural energy state

[7]Mie scattering also contributes to this effect but Rayleigh scattering is dominant

contrast to this when the sun is near the horizon the sky can appear red, while blue light is still preferentially scattered the path which the light traverses in the atmosphere is dramatically longer. Given that the scattering of light is multi-directional, at longer path lengths (penetration depths) the majority of blue light has been scattered out of the viewing angle of an observer on the surface[8]. The remaining low frequency light is still weakly scattered, making the indirectly observed "sky light" appear both fainter (darker) and red.

Raman scattering can also be thought of as the excitation of an atom or molecule to a virtual state (Figure 3.5). On relaxation, there is a small probability that the molecule will de-excite to a different (ro-)vibrational state than the one from which it was excited (Figure 3.5), this results in a slight shift in the energy / frequency / wavelength of the light, which is re-emitted from the secondary molecular source. This can be shown mathematically as:

$$\nu' = \nu \pm \frac{\Delta E}{h} \tag{3.1}$$

where ν & ν' are the frequencies of incident and re-emitted photons, ΔE is the difference between the two energy levels and, h is planks constant. As a result, this phenomenon can be used to investigate the (ro-)vibrational spectrum of a gas/liquid/solid (Figure 3.6). Rather than measuring the absorption or transmission of IR light through a sample as a function of wavelength, Raman spectroscopy measures the intensity, I of re-emitted light as a function of its deviation from the incident radiation wavelength ($\Delta\lambda$). This is achieved by using a narrow band, high intensity optical source (such as a laser) to illuminate the sample and then to spatially filter the excitation wavelength in a spectrograph before detection. This avoids saturation of the detector so that the relatively low intensity of the raman scattered can be detected.

In this document we will discuss specifically the Raman spectroscopy of multi-phase silicon as deposited by VHF-PECVD. The specific application of Raman spectroscopy in this case is to asses the volumetric crystalline fraction (VCF) of the material as a

[8]Absorption is also accountable for a fraction the radiation lost before it reaches an observer

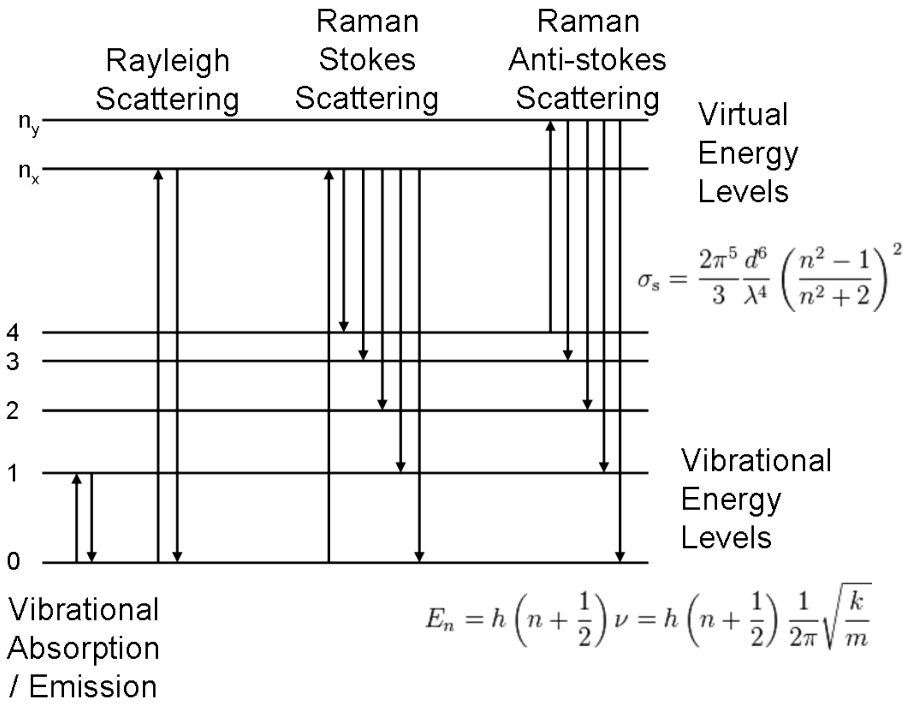

Figure 3.5: An energy level diagram showing the possible transitions to/from virtual energy states as part of Reiligh scattering and Raman spectroscopy

function of plasma process conditions. There are specific considerations that should be made for this measurement. Firstly it is necessary to consider then nature of the vibrational states which are being examined. Contrary to the appearance of spectra observed gaseous samples which display discreet vibrational states, the spectroscopic analysis of non-crystalline solids in particular show broad, overlapping peaks.

It is well established that the vibrational states within a crystal lattice can be easily effected by local or global inhomogeneities in the inter-atomic bonds. While the majority of inter-atomic bonds may be homogeneous the presence of trace contaminants will lead to slight shifts in the energy required to reach a specific excited state. This has the effect of broadening the observed peak in any vibration spectrograph. Locally this effect is strongest when a contaminant is directly adjacent to an atom in the crystalline matrix; naturally the effect is less significant when separated by 2 (or more) inter-atomic bonds as such when observing a volume averaged spectra the spectral broadening is dependent on the density of contaminants. Furthermore in the

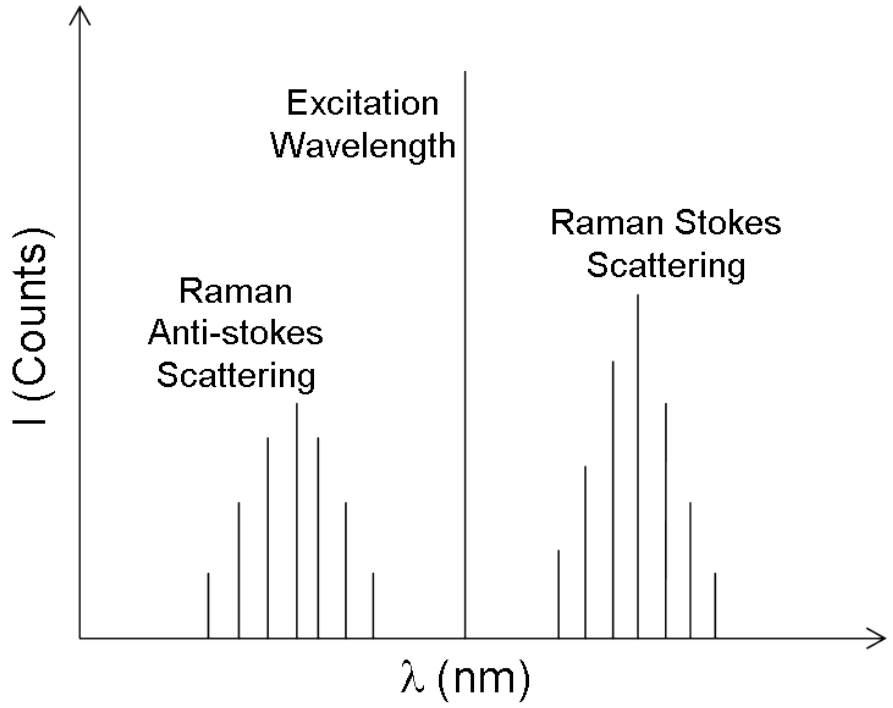

Figure 3.6: A sketch of the expected shape for a theoretical raman spectrum showing discrete energy level transitions both above and below the excitation corresponding to the stokes and anti-stokes transitions shown in figure3.5. Energy levels for solids such as examined in this study are broader and thus overlap but the principal remains the same

case of hydrogenated nano-crystalline silicon (nc-Si:H) the film consists of 2 atomic configurations; specifically, sub-micron sized crystallites surrounded by an amorphous matrix, dangling bonds are primarily passivated by hydrogen atoms.

First, considering the behaviour of material within a crystalline island, the lack of long range order causes deviation in the vibrational energy states from the idealised crystalline model. Experimentally, when viewing a spectrograph, this manifests in a blue/red shifting of the Raman peak centre this shift is a function of crystallite size. Furthermore, considering the nature of amorphous material which exhibits no long or short range order, it can be inferred that the excitation energy for each atomic bond can deviate significantly from its neighbour's. Finally, material at the interface between crystalline and amorphous material presents a greater density of dangling bonds which are primarily passivated by atomic hydrogen. Some short range order is evident in atoms located in this region resulting in an emission in the spectrum between that of the crystallites and amorphous extremes. Given these distinct material composition and the resultant distinct emission profiles it is expected that the observed Raman spectra will contain 3 components the relative intensity of which correlate to the volumetric fraction of each phase.

Given that the probability of a photon exciting a virtual vibrational state depends on the material structure the intensity of the individual emission peaks depends also on these probabilities

$$X_c = \frac{I_b + I_c}{I_a + \alpha_b I_b + \alpha_c I_c} \tag{3.2}$$

where X_c is the volumetric crystalline fraction (VCF), I_c, I_b, and I_a are the emission intensities of crystalline, boundary and, amorphous peaks respectively, in addition α_b and α_c are the relative photon cross sections for the given excitation wavelength. The relative photon cross section in this case is the relative chance of excitation of a virtual vibrational state in crystalline material when compared to the probability of excitation in amorphous material. For example $\alpha_c = A_c/A_a$ where A_c and A_a are the absolute absorption probabilities. In all experiments detailed within this document we have assumed a relative scattering cross sections of 1 for all materials giving the simplified

formula

$$X_c' = \frac{I_b + I_c}{I_a + I_b + I_c} \tag{3.3}$$

where X_c' is the Raman crystalline fraction (RCF), related to but not exactly the crystalline volume fraction. This assumption can be justified as follows: While an extensive body of research investigating the absorption coefficients of amorphous, crystalline and mixed phase silicon exists [62, 65, 67] producing and measuring the components of mixed phase material in isolation is inherently subject to errors. This is reflected in the variance of the published figures (0.1-0.88). In addition the relative absorption coefficients can be strongly dependant on the crystallite size and Raman excitation wavelengths as mentioned in *Ledinsky et.al.*[68]. Using relative absorption fractions of 1 gives an ease of consistency not only from measurement to measurement but also in comparison to findings within the literature. In addition we are sure that the Raman crystalline fraction, X_c' is a lower limit for the volumetric crystalline fraction (VCF), X_c, in the examined silicon.

Another factor which specifically effects the Raman analysis of nc-Si:H is the Raman collection volume (RCV). For Raman spectroscopy completed in a back scattering configuration the RCV is half of the penetration depth, light which penetrates deeper into the solid before scattering will most likely be absorbed before exiting the film (Figure 3.7). Typical nc-Si:H layers are on the scale of 1 micron, while the penetration depth is strongly dependant on the excitation wavelength. In addition the VCF of the material is known to decrease as a function of depth. This is due to the growth mechanism of the material growth, where individual crystallites grow from nucleation sites early in the deposition as described in Chapter 1.3. Given that the crystalline fraction is significantly lower in the incubation layer, formed during the initial phases of deposition those wavelengths which penetrate further into the material will show a lower value of RCF.

Once a Raman spectrum is obtained it is necessary to assess the contribution of each relevant component in order to accurately determine the RCF. The following will outline the fitting procedure for the results presented here. The analysis was completed

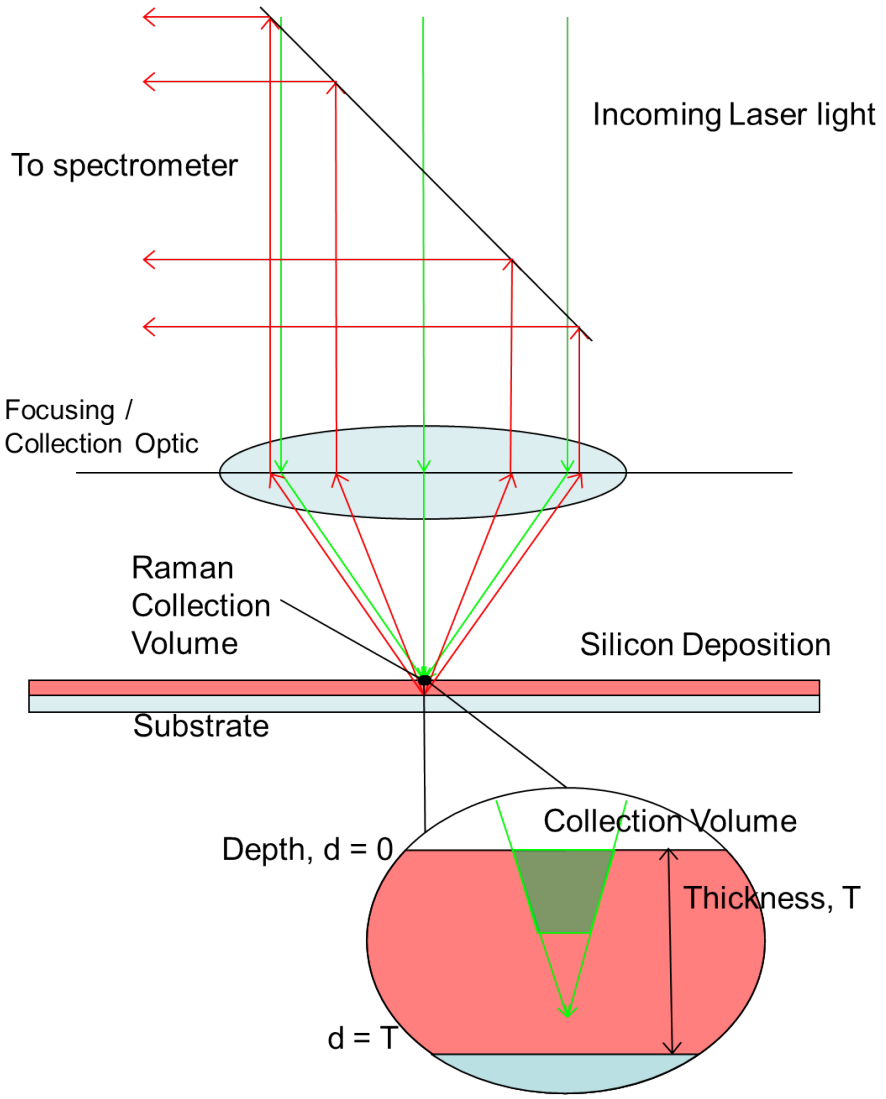

Figure 3.7: Schematic of a sample being examined by Raman spectroscopy in a back scattering configuration. Focused laser light interacts with the film, light which is backscattered will be collected by the focusing lens and directed through a spectroscope where light intensity can be measured as a function of Raman shift. A representation of the RCV, 1/2 of the penetration depth is shown with respect to the layer thickness.

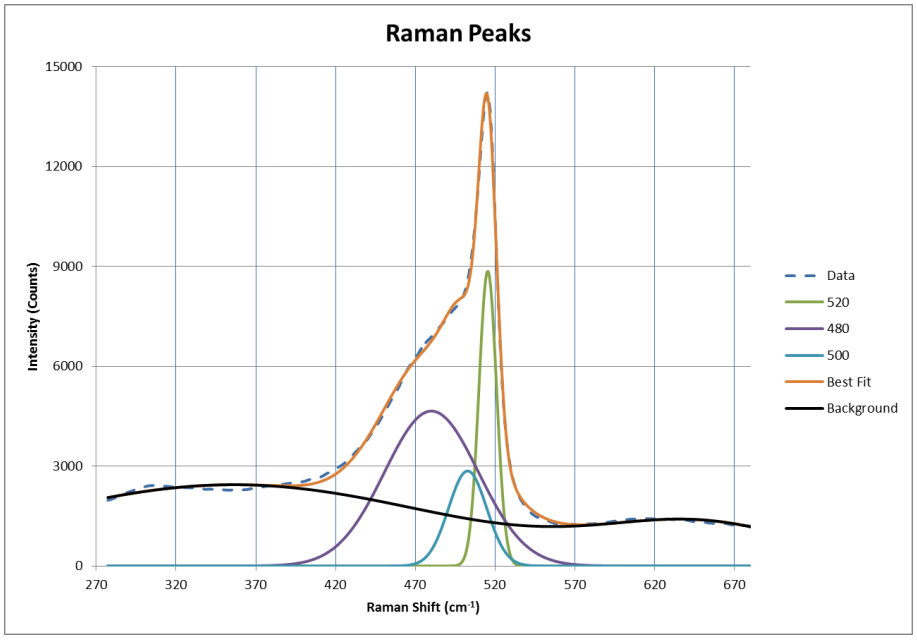

Figure 3.8: A graph showing the various components used in fitting a Raman spectra of multi-phase silicon, Intensity is plotted in counts versus the shift in wave-numbers. The experimentally acquired data is shown as a dashed line to show the quality of the fitting procedure. All component peaks are Gaussian. Specifically shown are the amorphous ($480cm^{-1}$), boundary ($510cm^{-1}$) and crystalline ($518cm^{-1}$) contributions ans well as a 2 peak background. Fitting is achieved by a least squares routine in the fityk program[89]

using Fityk spectrum analysis software[89] fitting parameters included the peak centre, peak maximum and full width half max (FWHM) of each of the Gaussian components. The fitting procedure was kept constant for all results presented, the quality of the fit was verified by the monitoring the least squares deviation as well examining the individual peak's contribution. The raw data was first restricted to an appropriate range ($300cm^{-1} - 750cm^{-1}$) so that irrelevant secondary features of the broadband spectrum could be neglected in the fitting routine. 5 main peaks were used to produce the spectrum. In addition to the 3 silicon peaks mentioned above, 2 additional Gaussian peaks were used to simulate the background; while the background contained various secondary peaks their relative intensity and frequency shift their effect on fit quality was considered to be negligible.

In cases where individual peaks deviated significantly such as to be visually different from the observable effect in the raw data the peaks were manually approximated before restarting the automated fitting routine. For example in an instance where there was a low amorphous contribution this peak was often difficult to distinguish from the background. In some instances this led to a strange "best fit" solution, one of local background peaks would exceed the actual measured intensity levels in the $480cm^{-1}$ region but was compensated for by a second negative Gaussian peak, neither of which appear close to the expected $480cm^{-1}$ shift position. While this configuration may have produced the best least squares fit it was clearly not an accurate representation of the spectrum and as such was re-fit restricting the amorphous peak to a centre position of $480cm^{-1}$.

Once an appropriate fit was found for a spectrum the area of the three relevant peaks were calculated and the RCF obtained using formula 3.3. The RCF was then related back to the relevant experimental parameters in order to discern any trends in behaviour which not only allows the prediction of advantageous process regimes but also gives insight into the behaviour of plasma parameters and gas phase chemistry relevant to the deposition regime.

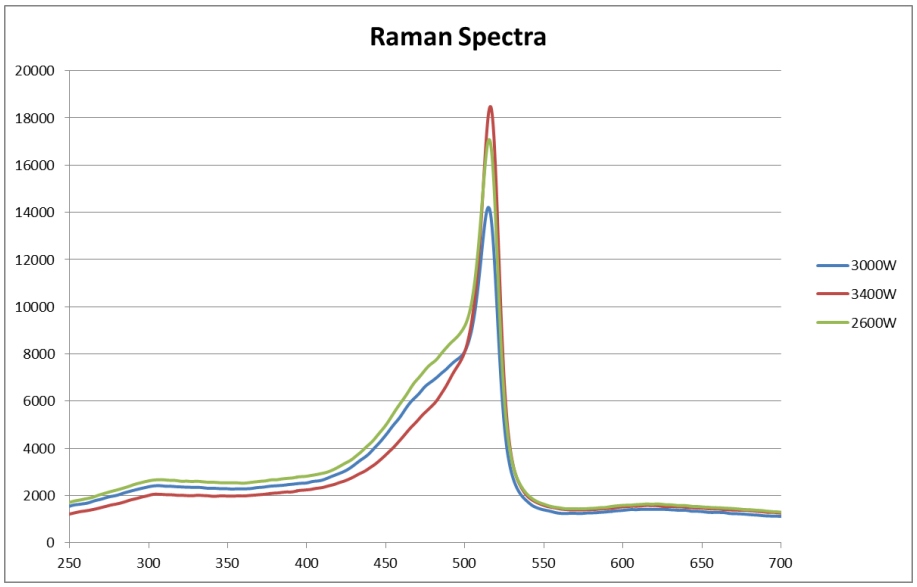

Figure 3.9: Several Raman spectra of mixed phase silicon with varying degrees of crystalline fraction. The change in crystalline fraction is apparent in the comparative area of the narrow , crystalline(520 nm) and broad, amorphous (480 nm) peaks

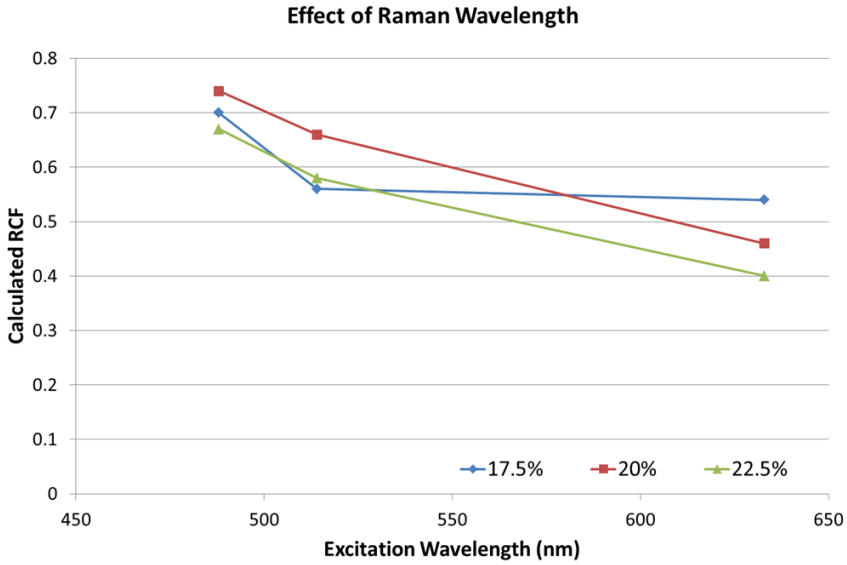

Figure 3.10: The dependence of RCF on excitation wavelength. 3 layers deposited at 17.5%, 20%, and 22.5% silane fractional flow. The layers have thicknesss of 3500Å, 4000Å, and 3300Å respectively. The excitation wavelength determines the penetration depth and collection volume. Measurements made at shorter wavelengths and smaller collection volumes show a higher RCF for fil.

3.3 Dek Tak

Due to the inherent spatial structure imposed on the plasma by the multi-tile design of MAMELUKE it is of great importance to quantify the extent to which this effects spatial uniformity of deposited films. The most obvious metric of this uniformity is the film thickness. We measure the uniformity of a films thickness using a Brunker/Veeco Dektak profilometer. The profilometer consists of a diamond tipped stylus, the vertical position of which can be accurately measured by an electromagnetic sensor positioned on the opposite end of a lever to the stylus tip.

The fulcrum of the lever is held at constant height during a scan and the sample is moved relative to the stylus on a 2-axis (x, y) stage as the measurement proceeds. Positioning and alignment of the substrate is achieved using a video camera focused on the area under the stylus tip. The feed from the video camera is overlaid with a cross-hairs approximating the point of contact (if the stylus were to be lowered) so that alignment can be achieved without damaging the stylus tip.

The description of this measurement has been divided into 3 sections for reasons of clarity; sample preparation, measurements, and, analysis each of which will be described sequentially.

- Sample preparation
  - Deposition were preformed on small substrates of 200 mm × 430 mm placed on top of the full sized carrier substrate. These substrates were aligned with the corner of the carrier opposite tile 1. The 430 mm side was aligned with the 720 mm side of the carrier.
  - The substrates were prepared before deposition by "masking," a line along the glass substrate using a permanent (waterproof) marker. The line was drawn 75 mm from (and parallel to) the long (430 mm) side of the substrate. The line was drawn so as to be located on the substrate area facing electrodes 1-4 as seen in figures 3.2 and 4.5.
  - After deposition the mask was removed by wiping the surface with a cloth,

containing a solvent of isopropyl alcohol. The process also removed any silicon deposited on top of the line; revealing a strip of bare substrate. This area will be referred to as the reference strip.

- Finally a sample area is cut from the substrate using a diamond scribe. The scribe marks were made on the the back side of the glass and, the sample is made small enough to fit on the stage of the DekTak but big enough to include the area of interest (between tile centre 2 and tile centre 4).

- Measurements

  - The sample section (of the substrate) is placed on the stage of the DekTak
  - The sample section was aligned horizontally by hand so that the maximum range (15 cm) of the of the stage (x-drive stepper motor) could be utilised. The stage was sent to it furthest extrema (± 7.5 cm) and it was ensured that at these positions the stylus was above the substrate, specifically over a point corresponding both tile 2 and tile 4 at extrema[9].
  - The substrate was then aligned so that the reference strip was parallel with the direction of the x-drive. Again the x-drive was sent to it's extrema and the substrate was rotated so that for the same y-drive position (nominally 0 mm) the cross-hairs is above the centre of the strip.
  - A this point a single scan could be made. The stylus was moved down using a third (z) motor until it makes contact with the substrate[10].
  - The stage was moved in the direction perpendicular to the reference line (y), the vertical position of the stylus was continually logged at the desired spatial resolution. At the end of a scan the thickness was calculated using the step height function described below in as part of the discussion of analysis.

[9]This is done so that the measurement does not over shoot on one end, or fail to capture the deposition profile from the 2 inter-tile boundaries

[10]The force between the stylus and the substrate is maintained as less than 3mg and as such avoids errors in measurement due to deformation of film.

  - A 3D map of stylus height versus position was made by plotting all of the levelled z vs y scans. A thickness profile (Δz versus x) was created by repeating the step height measurement along the length of the exposed strip. The DekTak Software allows for the automation of both these process.

- Analysis

  - Post-analysis tools described here utilise cursors. These cursors consist of a range of y values selected in advance. The y position and width of the cursor can be controlled by the user. Each cursor will represent a relative measurement in z the average height of the stylus is calculated for this range to remove error due to jitter and the value is assigned to the y position at the centre of the cursor range (band width)

  - Given that the stage is not perfectly level it is necessary to subtract a background slope for each scan. The DekTak software allows for automatic levelling of the scan by the use of 2 cursors placed at points known to be at the same height. In this case they were placed at 2 points within the reference strip. This levelled scan was then saved as a single profile so that all profiles could be plotted versus x for a full 3D map of the surface.

  - Once level another set of 2 cursors could be placed to automatically calculate the thickness using a step height function. In this case one of the cursors was placed at the position corresponding to silicon adjacent to the reference strip, while the other was placed in centre of the reference strip. The difference in height, Δz of the cursor measurements was taken to be the thickness at that x position.

Certain complications should be noted about the techniques described above as they will influence the interpretation of the profilometry results. The 2 main sources of complication are: imperfections in the reference area, and the automation of the levelling and step height processes.

Often imperfections in the removal of silicon would leave islands of residual material.

As a result the levelling of an isolated z versus y scan would be skewed. In addition often areas of material were removed outside of the masked area. While the automation of levelling and step height processes was convenient for the faster completion of analysis it introduced a level of inflexibility. The y position and thickness of the cursors needed to be set before the acquisition of the 3D data set. Any in consistencies such as those described above could not be accommodated for as they were un predictable.

These complications often resulted in spurious outliers in the thickness profile. No easy solution was found to correct of these errors. As such these points must be removed and or discounted manually to give an accurate representation of the deposition profile[11].

[11]No interpolation of the data has been preformed and so any data which has been removed from the graphs is shown as visible gaps in the plots

3.4 Activation Energy & Film Conductivity

In initial experiments, to be presented in chapter 4.1 we are interested in the transition form amorphous to nanocrystalline material as the plasma parameters are changed. In order to explain the film tests preformed some knowledge of semiconductor behaviour is required. From solid state physics it is known that solid materials have energy bands rather than discrete energy levels. This is caused by an overlapping of the discrete levels of neighbouring atoms. As the number of neighbouring atoms becomes much greater a band structure emerges. The bands which most concern us are the valance band (the highest band where electrons are normally present at absolute zero) and the conduction band (The lowest band that allows an electron to flow freely from atom to atom). Considering 3 basic kinds of solid, conductors have a band structure where the valance band and conduction band overlap, while insulators have bands which are separated in energy by their band gap, E_g. Semi conductors have a band gap which is small enough that it can be overcome by an electron with a reasonable amount of energy [12]. When the material is at a reasonable temperature there is sufficient energy to excite some electrons into the conduction band. Assuming a Boltzmann distribution of thermally excited electrons within the structure it is expected that the conductivity of a semi-conductor increases exponentially with temperature. It is also possible for the conductivity of a material to be changed by other means of excitation, specifically it is possible for electrons to be excited by exposure to light whose photon energy ($E_{photon} = h\lambda$) is above that of the band gap.

In the case of nc-Si:H the grain boundaries of the crystalline islands provide locations where discrete intermediate energy levels are introduced which has the effect of reducing the necessary thermal energy needed to introduce an electron hole pair. The dark conductivity of nc-Si:H is therefore much greater than that of a-Si:H. This can be observed in both the dark-photo conductivity ratio and the activation energy (E_a).

To test film quality, 1 inch square glass tokens are placed on the substrate. Af-

[12] reasonable in this case is intended to imply an amount of energy that is easily anticipated under normal conditions e.g. a particle with thermal energy within material at room temperature or the amount of energy associated with a photon of visible light

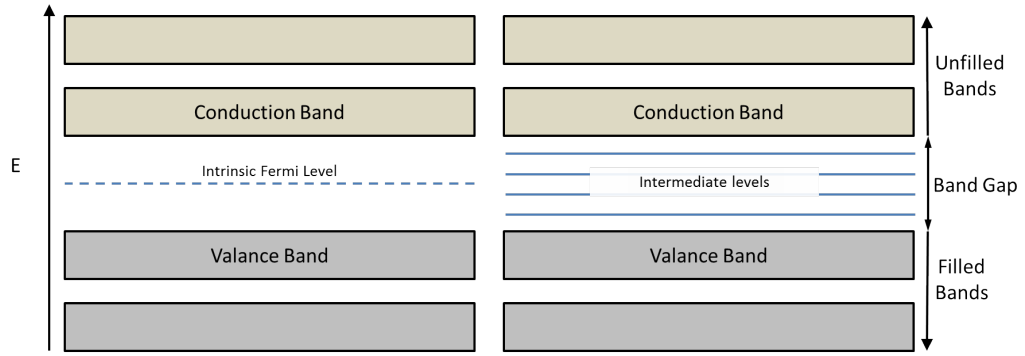

Figure 3.11: A diagram showing the different energy bands seen in a traditional semiconductor (left) and in nc-Si:H (right) The intermediate levels lead to the activation energy measurements explained below

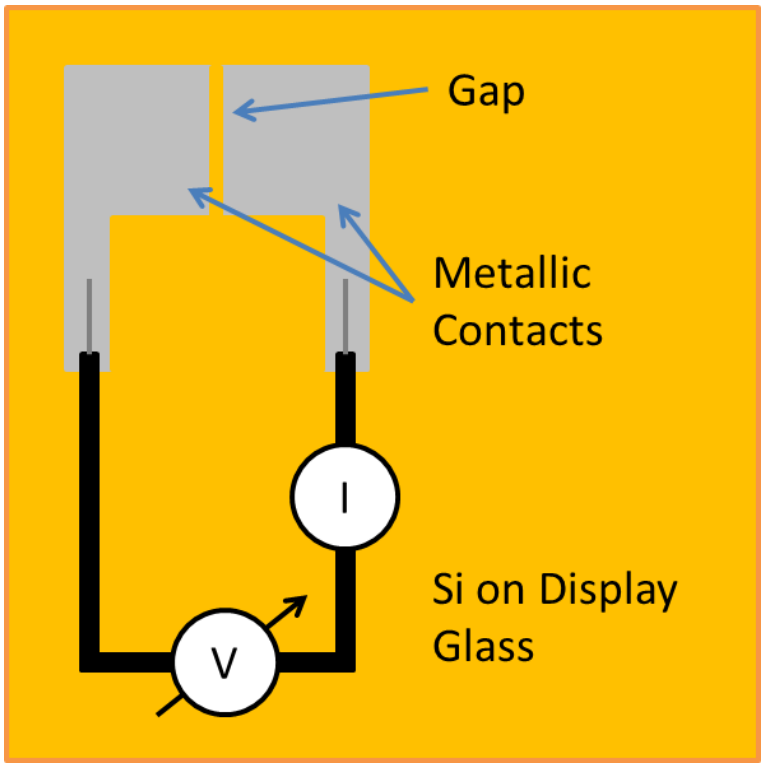

Figure 3.12: The layout of a 1 inch^2 glass token used to measure the conductivity levels of deposited silicon. The electrodes are connected to a 90V power supply and the current is measured for changing temperatures as well as the light/dark ratio while at room temperature

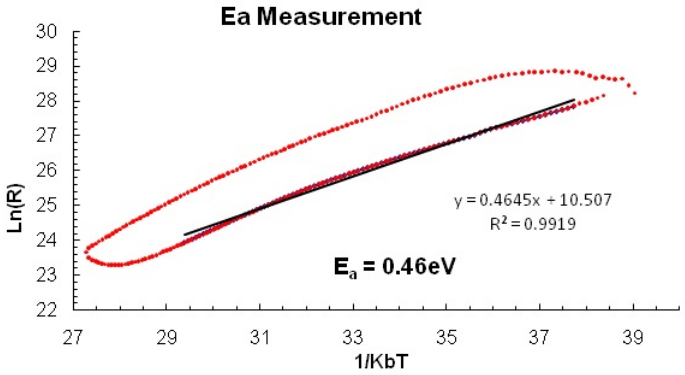

Figure 3.13: A scan of film resistance versus temperature for both the heating and cooling cycle the slope of this graph gives the activation energy of the material

ter deposition metallic electrodes are deposited on each sample so a calibrated area of 10 mm^2 can be examined. Each sample is tested for activation energy (Ea) and dark/light-conductivity. A constant voltage (90V) is placed across the metallic contacts in (a dark) vacuum and the current is measured as the sample is put through a temperature cycle. The resistance is calculated and the activation energy is determined by calculating the slope of a line fit to a graph of $Ln(R)$ versus $\frac{1}{K_bT}$.

$$E_a = \mathrm{Ln}(R)k_bT \tag{3.4}$$

When the sample returns to room temperature (20 °C) the current is measured for both dark and light conditions to give the conductivity ratio, the light current remains relatively constant, while the dark current saw significant changes which we later attributed to the crystalline fraction. A high conductivity ratio (>1000) and E_a (>0.5eV) are taken to indicate amorphous material alternatively samples are said to be crystalline.

3.5 X-Ray Diffractometry

The final diagnostic we have utilised to characterise the silicon films deposited by MAMELUKE is X-Ray Diffractometry (XRD). This diagnostic operates on the principles of diffraction and interference, where light waves transmitted through a aperture will be bent as shown in figure 3.14 a). In order for diffraction effects to be significant the aperture dimensions should be comparable to the light wavelength. When light is transmitted through 2 or more apertures placed with equal spacing between them interference will occur between the bent wave-fronts. Constructive interference will occur at positions where the wave fronts from each source are in phase, and destructive interference will occur at positions where they are 180° out of phase, as seen in figure 3.14 b).

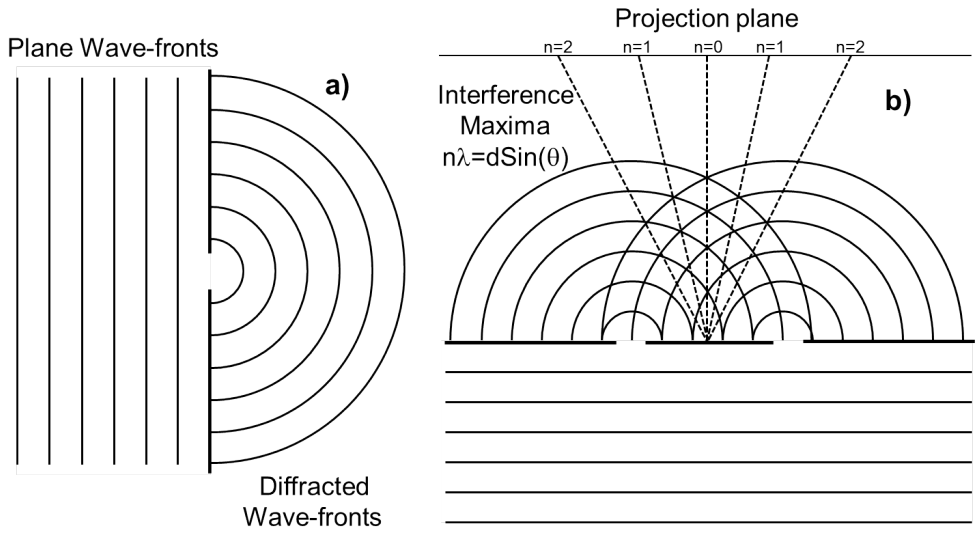

Figure 3.14: A drawing showing the bending, or diffraction of wave fronts as they pass through a single, a) or double, b) slit configuration. Wave front bending occurs when the slit width is comparable to the wavelength. When there are 2 or more evenly spaced slits as seen in b) an interference pattern can be seen as a result of the constructive and destructive interference taking place at different angles to the plane of the slits. Dashed lines show angles at which constructive interference takes place

The condition for constructive interference is that the path difference between radiation diffracted by adjacent apparatuses equals an integer number of wavelengths of

the light. This is known as Bragg's law and can be expressed as follows,

$$n\lambda = \mathrm{d}\ \mathrm{Sin}(\theta) \tag{3.5}$$

The path difference between light transmitting adjacent apertures depends only on the spacing between apertures, d and the angle of diffraction, θ. This is better understood by considering the path difference between 2 rays as a function of diffraction angle as seen in figure 3.15 a).

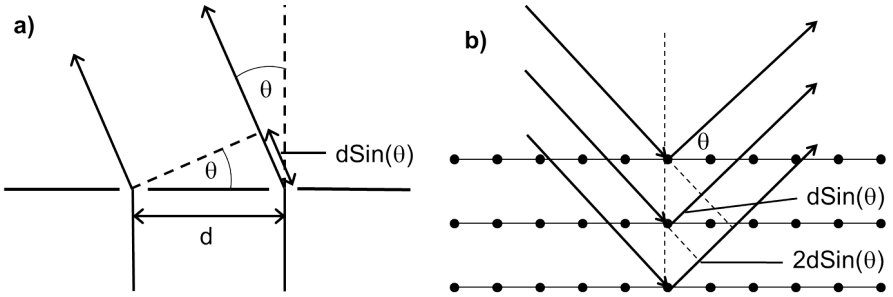

Figure 3.15: To determine the points at angles at which constructive interference will take place we consider the phase shift between light diffracted from adjacent slits, a), or crystal planes, b). Constructive interference will occur when the phase difference is equal to an integer multiple of the light wavelength. The phase difference between slits (or planes) can be calculated as a function of angle

When considering a crystal as the diffracting element in an experiment it is the individual atoms in the lattice. The uniform spacing between crystal planes defines the condition for constructive interference. In addition when considering relative path difference between 2 rays diffracted by adjacent crystal planes, the relative path difference doubles giving: 2d Sinθ, assuming equal angles of incidence and diffraction as shown in figure 3.15 b).

For these tests we used a Brüker D8 Advance diffractometer. The X-ray source consists of a Siemens X-ray tube, which produces a combination of Kα, Kβ and bremsstrahlung radiation. The $K\alpha$ radiation is isolated and collimated by use of a parabolic Gobel mirror and a slit. The X-ray beam is 6 mm in width and 3 cm in hight. The detector is equipped with 2 6 mm slits to limit the incoming radiation radiation. The first slit eliminates any scattered radiation reducing the background

while the second, detector slit defines the spatial resolution of the scan.

The sample is mounted on a motorised stage. The stage is capable of movement in the 3 spatial dimensions (x, y, z), where z is the dimension perpendicular to the surface of the stage (and the sample). In addition the stage is capable of motorised rotation in 3 axes θ, X, and Φ, which correspond to rotation about the x, y, and, z axes respectively. In addition the detector is capable of rotating about the stage so as to collect the diffracted x-rays.

Given the small thickness of the layers produced, the scans preformed as part of this thesis operate the XRD in a grazing angle configuration where the stage is positioned to have small angle of incidence (2.5°) with respect to the source. The detector is then swept about the sample logging x-ray intensity as a function of the angle of diffraction, 2θ

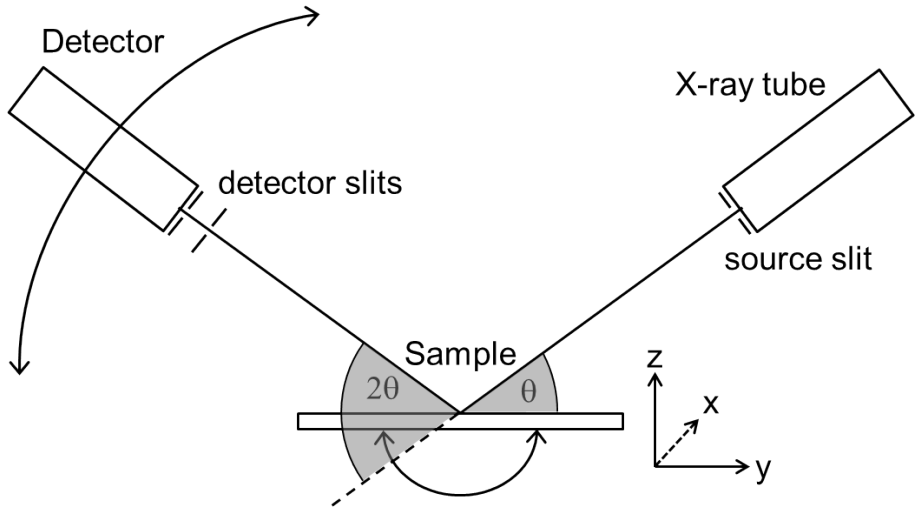

Figure 3.16: A schematic of the XRD measurement showing x, y, and z directions as well as the angle in which the detector and sample are rotated. For the grazing angle scans preformed in this study θ is held constant at a small value of $\approx 2.5°$ while the detector is scanned through a 2θ of $0° - 60°$

Given that the crystal planes of silicon have different spacing we see peaks ad different angles for each orientation. Peaks at $\approx 28.5°$ $\approx 47.5°$ and $\approx 56°$ correspond respectively to the 111, 220, and 311 planes[64]. The intensity of these peaks is measured by manually selecting a peak width for each of the relevant peaks by manually defining a start and an end point. An approximated, linear background is calculated

and subtracted from the total (integrated) area under each peak. The results are tabulated and used to support the findings made using raman spectroscopy but also to give insight into any preferential growth orientation of the silicon.

Chapter 4

Results

4.1 Demonstration of VHF Behaviour

As mentioned in section 1.3 the primary advantage of VHF-PECVD of nc-Si:H in comparison to conventional PECVD is higher deposition rates of device quality material. This is explained by more efficient depletion of silane in the plasma, which has been attributed to both the reduction in sheath impedance and the development of high frequency chemistry, which has been linked to a high energy tail EEDF, associated with increasing excitation frequency.

When deposition experiments were first conducted on the MAMELUKE source the goals were to first: Confirm that the expected VHF deposition capabilities were achievable and second: To inform the direction of future research, most relevant was the question of how significant was the effect of the segmented electrode on film uniformity when depositing crystalline material at high rates.

Film analysis was preformed using Raman spectroscopy at various wavelengths. The research was also guided by measurements of activation energy[1]. RCF, activation energy, and spot measurements of thickness were made on small ($1''^2$) tokens of, 1 mm thick, un-coated, display glass. The tokens were placed in front of the centre of tile number 2 as shown in figure 3.2. While local measurements of thickness were made on

[1] as measured using the conductivity behaviour of the film

the tokens, profilometry was preformed on the full scale (600 mm × 720 mm) substrate of 3 mm thick float glass, coated with Pilkington Tec8 thin conducting oxide (TCO). Thickness measurements in this section were all made individually without the use of the automated procedures described in section 3.3.

The first experiment preformed was to confirm that the source could be used to deposit nc-Si:H at high deposition rates, with lower levels of hydrogen dilution than systems utilising conventional 13.56 MHz. To this end the silane fractional flow (SFF= $\frac{Q_{SiH_4}}{Q_{total}}$) was increased while the crystalline fraction was monitored by Raman spectroscopy and/or activation energy measurements. A series of layers that appeared on the transition from crystalline to amorphous behaviour were then deposited and analysed by raman spectroscopy preformed using 3 wavelengths (488 nm, 514 nm, and 633 nm), 3-peak curve fitting analysis was preformed, as described in section 3.2 and the resulting data is presented in figure 4.1.

For these experiments other process parameters were held constant as follows: Forward VHF power = 2400 W ; pressure = 1 Torr (≈ 1.33 mbar); silane flow = 90 sccm; deposition time = 500 s, substrate temperature = 180°C; distance from electrode to substrate surface 8 mm. The silane fractional flow was changed by increasing or decreasing the flow of hydrogen with set points of 424 sccm, 360 sccm, and 310 sccm, which correspond to silane fractional flows of 0.175, 0.2, 0.225 respectively.

Initially, it was noticed that the calculated raman crystalline fraction (RCF) is significantly different for each of the wavelengths used. We attribute this behaviour to the increasing crystalline fraction of the material as it grows. The known growth mechanisms of nc-Si:H indicate that material deposited earlier and thus deeper in the film has a lower crystalline fraction; the material which is deposited first, known as the incubation layer, is completely amorphous. Laser light of longer wavelengths has a greater penetration depth which increases the collection volume and decreases the average crystalline content of the examined material.

Secondly, it was noticed that, while the RCF measured by 633 nm follows the expected trend of decreasing crystalline fraction for increased silane fractional flow the

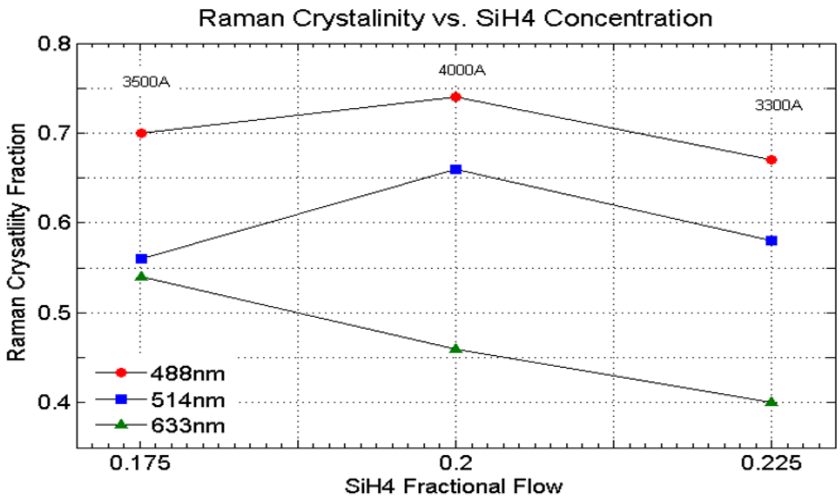

Figure 4.1: The behaviour of crystalline fraction as measured by Raman spectroscopy as the silane fractional flow is increased. The laser wavelength is changed (488 nm, 514 nm, and 633 nm) and the change is shown to have a significant influence on the calculated RCF due to the difference in penetration depth as is explained 3.2.

other wavelengths show an unexpected peak in crystalline fraction at a silane fractional flow of 0.2[2]. Initially this was not understood then the thickness of each sample was examined.

Elaborating on the theory of different collection volumes for each the laser wavelengths, to a first approximation the RCF as measured by 633 nm can be considered to be the thickness averaged crystalline fraction[3], while the shorter wavelengths, particularly 488 nm give an estimate of the surface crystalline fraction. The thickness of each sample is noted at the top of figure 4.1 with the sample deposited at 0.2 silane fractional flow is 50 nm thicker than the others.

The high sensitivity of measurements at shorter wavelengths to layer thickness indicates that the layers crystalline fraction is continuing to increase with deposition time (layer thickness) under these conditions. Given that the layers examined here are $< 0.5\,\mu$m and that absorption layers in solar cells are typically at least double this, it

[2]this behaviour is not consistent with data reported in the literature and requires explanation

[3]The thickness averaged crystalline fraction is used to describe the average fraction of crystalline growth over the entire film thickness at the point of measurement.

is not unreasonable to predict that material grown under these conditions, but for a longer times would show significantly higher volume average RCF. Having made these considerations it was concluded that the films produced by the MAMELUKE source displayed results which met or exceeded expectations based on the behaviour of other VHF-PECVD sources presented in the literature.

Specifically considering the deposition deposited at the lowest silane fractional flow:

- This film showed the highest volume averaged RCF (633 nm) and was still deposited at a rate of 7 angstroms per second (0.7 $\mathrm{nm}s^{-}1$). While this is not exceedingly high it is a considerable improvement on rates achieved by 13.56 MHz plasma ($\approx 0.3\,\mathrm{nm}s^{-}1$)
- The surface crystalline fraction of this film is very high (0.7) If deposited to a thickness suitable for solar applications the volume averaged RCF would be considerably higher
- This crystalline fraction was achieved with a SFF of 0.175 where a typical deposition in solar manufacturing would have a value of ≤ 0.05

In conjunction with the raman analysis XRD measurements were also made on these depositions. The results are presented in figure 4.2. Five specific elements were

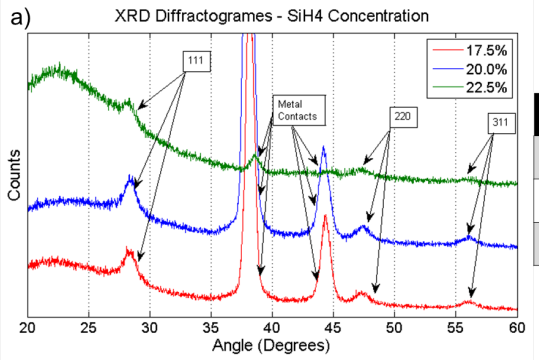

b)

SiH4%	111	220	311
17.5%	0.603	0.294	0.104
20.0%	0.60	0.30	0.11
22.5%	0.61	0.29	0.10

Figure 4.2: The behaviour of X-ray diffractogrammes as the silane fractional flow is increased. 3 diffractogrammes measured for films deposited at 17.5%, 22%, and 22.5% silane flow are shown in a) to the left. Peaks associated with the 111, 220, and 311 planes of crystalline silicon are observed and the relative intensity of these peaks is shown in the table, b) to the right

identified in each of the plots. In addition to the background X-ray counts there were 2 elements not associated with the nc-Si:H which were identified before being discounted. There was a broad "amorphous peak," which appeared at a 2θ angle of approximately 22° and 2 high intensity peaks at angles of 38° and 44° which were attributed to the metal contacts used for film conductivity measurements.

It is clear from the plots that the intensity of the peaks at $\approx 28.5^\circ$ $\approx 47.5^\circ$ and $\approx 56^\circ$ corresponding to the 111, 220, and 311 planes collectively follow the trends seen in RCF. That is to say that for increasing silane fractional flow, and reduced volume averaged crystalline fraction, the intensity of all "crystalline" peaks is reduced. When the relative area of the peaks is compared however, the data suggested that there is no change in the fraction of material growing in each orientation. The consistent breakdown in orientation is $\approx$60% in the 111 direction, $\approx$ 30% in the 220 direction and, $\approx$ 10% in the 311 direction for the three depositions examined.

Given the proof of VHF like behaviour, the next step was to investigate the ability of the source to operate in a higher depletion regime. With knowledge of of the sources behaviour as dilution was changed it was decided to hold the dilution of the gas mix constant and to preform a second series of depositions examining the behaviour with changing gas flow. Little mention of a sources behaviour with increasing gas flow has been made in the literature but the expectation was the given the increase in silane flow and and the reduction in gas residence time the the density of molecular silane in the plasma would scale with total flow and show an appreciable effect on the conductivity measurements and the Raman crystalline fraction.

These depositions were preformed at the same process conditions (power, pressure, and substrate temperature) as above, but the deposition time was scaled so as to ensure constant silane exposure in an attempt to maintain equal deposition thickness. The SFF was held constant at a value of 0.2 while the total flow was set to: 459 sccm; 540 sccm; 630 sccm; and 720, which correspond to silane flow rates of: 90 sccm; 108 sccm; 126 sccm; and 144 sccm respectively. The results of the test can be seen in figure 4.3

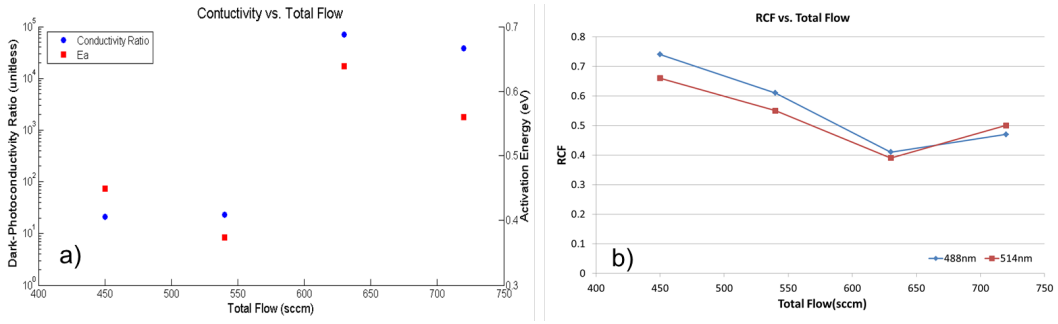

Figure 4.3: The material properties of silicon grown at different flow rates but with constant SFF. Measurements are of activation energy and light/dark conductivity ratio (left, a) as well as the RCF (right, b). The raman measurements were taken using laser wavelengths 488 nmand 514 nm, which have shallow penetrations depths and as such are more sensitive to film thickness.

As the total flow was increased for constant experimental parameters so too was the silane flow, conversely, given that the pressure was held constant by changing the pumping rate the silane residence time dropped. Both these factors acted to reduce the fraction of dissociated and thus depleted silane. As a result the silane density in the plasma increased and the silicon films became less crystalline resulting in a greater conductivity ratio and a larger activation energy. Despite equal silane exposure, the measured thickness of the silicon layers on the sample tokens was 400 nm, 370 nm, 295 nm, and 345 nm. In the absence of measurements taken using a longer wavelength the conductivity data is presented to strengthen the argument that the bulk crystalline fraction is effected by total flow. The falling RFC level follows the expected behaviour with increasing silane flow but could also be attributed to the different film thickness. The rise in RCF at 720 sccm certainty indicates some dependence on thickness, but the conductivity measurements data support some behaviour based on total flow. Further data exploring these trends is presented in section 4.2.

The topology of a segmented electrode source imposes a special structure in the plasma. It is expected that this spatial structure is dependent on the process parameters as explained in section 1.4.1. It is expected that as the forward power is changed the electron density of the plasma will change. With increased electron density at higher powers the higher currents seen at electrode edges will couple inductive power more

effectively. As the density increases the inductive penetration depth is reduced and as such power is coupled more effectively at the high current electrode edges (equation 1.23).

It is important to understand the effect this has on deposited silicon layers. To this end; deposition rate across and between neighbouring tiles was observed for 2 different levels of forward power (2800 W and 3200 W) and for two flow rates at the higher power setting (630 sccm and 720 sccm). The measured profiles are presented in figure 4.4. The same data is presented in the form of a 3D colour plot and a 2D scatter plot for clarity.

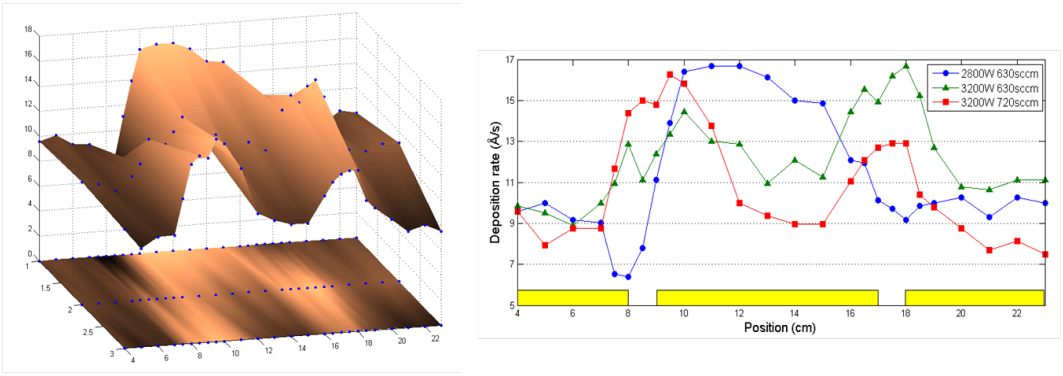

Figure 4.4: The thickness uniformity of silicon layers deposited with the MAMELUKE source at different process parameters. The boxes above to the horizontal axis represent the approximate position of tiles.

At lower powers the deposition profile had maxima at the tile centre and minima at the inter-tile boundaries. At higher powers the profile changed to have peaks at the boundaries. The high power profile was observed at 2 different total flow rates. This change is consistent with a shift in the power coupling mode of the source. At low powers capacitive displacement current in the sheath dominate, while at high powers inductive currents between the tiles become significant. The difference in local power deposition leads to a difference in dissociation rates of the molecular silane. The higher dissociation rates mean that there is a greater availability of film precursors and thus a higher deposition rate.

It was concluded from these initial results that there was good reason to believe that the spatial structure would have some effect the local film properties of the deposition,

and that this should be further investigated. It is also conceivable that an optimised, uniform condition could be found where power coupling modes are balanced.

4.2 Analysis of source Uniformity

The following section presents the major results of this thesis. The parameters for these experiments and the explanation of results is informed by the science and theory presented in previous chapters. The experiments described in this section build upon the results of the previous section 4.1, which consists of a preliminary investigation of the MAMELUKE source by characterising the material produced at a single position on the substrate; under the face of tile number 3 as seen in figure 3.2, neglecting the plasma spatial structure imposed by the push pull, multi-tile configuration of the source.

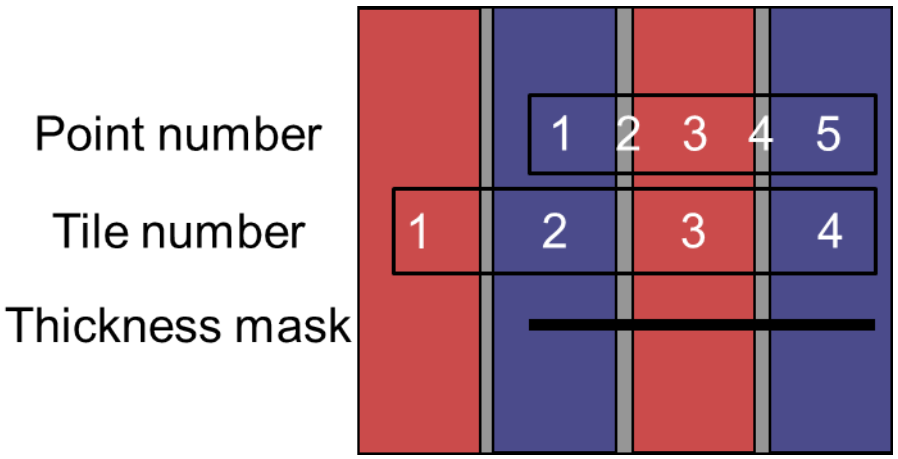

Figure 4.5: A diagram showing the points at which the RCF and thickness of a film are measured relative to the electrode tiles 1-4. Figure 3.2 shows the entire source in the same style (tiles of a different colour are powered out of phase with each other). All uniformity results shown in this chapter are as a result of measurements on this section of the substrate.

Many of the explanations may be similar in nature to those made in the previous section but they often bear repetition within the context of this uniformity study[4]. Here we elaborate on this groundwork and examine the deposition thickness & RCF uniformity as a function of process settings, plasma parameters, and deposition conditions. While these terms are interchangeable to a degree for the purposes of this document we will distinguish between them to facilitate the easy progression of explanations.

[4]The analysis is similar in that the same diagnostics are used and similar trends are observed, however in the context of this uniformity study there can be different causes for this behaviour

- "Process settings," or "set-points", will be used to refer only to quantities that can be controlled directly by the experimenter as a deposition is performed. Specific examples include gas flow rates and chamber pressure. These quantities are used to quantitatively distinguish between different depositions.

- "Plasma parameters" will be used to refer to specific quantities such as electron density, n_e, or plasma potential, V_s, the quantitative nature of which arise from the theory of plasma science (Section 1.1.1), but which only indirectly effect the properties of a deposited silicon layer. For the most part the quantities are not measured as part of this study, instead they will be used to describe known plasma behaviour as a function of process settings[5]. These known trends will inform the conclusions made to explain silicon uniformity results.

- "Deposition conditions" will be used to refer to quantities which have a direct effect on silicon film growth, and which are usually of specific interest in silane plasmas for thin film silicon deposition; examples include the ion impact energy and the atomic hydrogen flux to the surface.

Just as film properties can reveal information on the local gas phase chemistry they may also be used to qualitatively assess any sources of non-uniformity across the plasma. While there is a long list of process settings that can influence the plasma behaviour here we have chosen to examine the deposition behaviour directly, with respect to 2 settings; Forward power, P_{fwd}(W), and silane flow rate, Q_{SiH_4}(sccm), and indirectly with respect to one plasma parameter; the gas residence time, τ_r(s). The effect of these parameters on the plasma chemistry profile in a multi-tile source can be understood in quite simple terms allowing for easier analysis of the effect of the plasma spatial-structure on film properties.

Other experimental parameters are held constant. These parameters include: Gas pressure $p = 750 \pm 5\,\text{mTorr} \approx 1\,\text{mbar}$, plasma gap, $x = 10 \pm 2\,\text{mm}$; substrate temperature, $T_{sub} \approx 190 \pm 5°\text{C}$;total gas flow, $Q_{total} = 500\,\text{sccm}$ or $250\,\text{sccm}$; and silane

[5]For example it is known that increasing the chamber pressure of a plasma will increase the collision frequency, and reduce the electron temperature, T_e

exposure, $E_{SiH_4} = 1000 \pm 10\,\mathrm{scc}$[6].

The choice of these parameters is not significantly different from experiments performed in the literature but there are slight differences that should be noted before proceeding with a description of the results.

The silane exposure setting requires a little explanation. The silane exposure is a measure of the net amount of silicon delivered to the plasma. It is the product of the silicon flow rate (sccm) and the deposition time (mins), $E_{SiH_4} = Q_{SiH_4} t_{dep}$. We hold this parameter constant in order to achieve films of comparable thickness and as a result simplify the analysis of the RCF. Complications arising from the RCF analysis of films of different thickness are examined in section 4.1. In addition, if the film density is constant for all deposition conditions any variance in the thickness of the films can yield information about the silane utilisation of the plasma, which is simply a measure of the conversion efficiency from silane gas-flow to solid silicon in the film.

The primary plasma condition in determining the crystalline fraction of a film is the relative density of atomic hydrogen n_H and silane molecules n_{SiH_4} in the plasma bulk. As a result it was desirable to chose our process parameters so that they could be easily related to this parameter. The majority of previous experiments have controlled hydrogen density by changing the level of hydrogen dilution. While the hydrogen/silane fractional flow does effect the atomic hydrogen density in the plasma it is not always the primary determining factor. Furthermore depending on how a change in dilution ratio is achieved other effects of the changing gas flow configuration may become more dominant.

Consider the competing settings effecting the relative density of silane and hydrogen: The rate of silane delivery to the plasma[7] and the rate of silane dissociation[8]. The silane dissociation rate due to electron collisions is important due to several effects:

- Holding other settings constant increasing the forward power will increase the

[6] With respect to the $\pm$; numbers given, in this instance they represent an estimate in the variance/error in the measurement rather a result of quantitative analysis.

[7] which is simply to the silane flow rate

[8] which, to a first approximation is controlled by the power delivered to the plasma, assuming other settings are held constant

rate of ionisation in the plasma thus increasing the electron density

- This increased electron density leads to a higher rate of dissociation, encouraging a high rate of deposition which both removes silicon from the plasma, and releases several hydrogen for each silicon incorporated into the film.
- Each successive Silane dissociation increases the hydrogen density in the plasma
- Low n_{SiH_4} reduces the annihilation reaction which removes atomic hydrogen from the plasma $SiH_4 + H \rightarrow SiH_3 + H_2$

In completing these experiments it is desirable to obtain results comparable with the literature but also desirable to minimise the ambiguity that can arise from using the dilution fraction of the source gas a primary criteria. In order to achieve these goals the method by which the hydrogen dilution of the gas mix is changed between depositions is considered.

1. For constant silane flow; increase or decrease the hydrogen flow to achieve the desired fractional flow.
    - Assuming that hydrogen, as the diluent, is the primary gas component, the total flow will be dramatically effected by using this method.
    - If the pumping speed is kept constant then the pressure will also be effected which will in turn change the electron density and electron temperature of the plasma.
    - If the pumping speed is changed so as to keep a constant pressure the gas residence time of the silane will be affected.
2. For constant hydrogen flow; increase or decrease the silane flow to achieve the desired fractional flow.
    - Assuming that silane is the diluted gas, and as such, is the minority gas component: the total gas flow is only effected slightly by this method thus the pressure & pumping speed effects mentioned above are less significant but still present.

- This method assumes the dilution ratio is the primary determining factor driving the atomic hydrogen to mono-silane density ratio in the plasma which is not the case under all circumstances. Several studies have produced films of high crystalline fraction with low or even no dilution[19, 57, 90] indicating that high rates of dissociation can contribute sufficient hydrogen to facilitate crystalline growth.
  - $SiH_4 + e \rightarrow SiH_4^* + e \rightarrow SiH_x + (4 - x)\, H$
  - $SiH_3 \rightarrow Si_{film} + 3H$

3. For constant total flow; change both the silane and hydrogen flow for each deposition to achieve the desired fractional flow.

   - This method allows for an analysis of film properties as a function of forward power and net silane flow as well as fractional silane flow (or hydrogen dilution). When considering process settings which contribute to the silane and atomic hydrogen density these are the most direct.
   - Considering silane flow and forward power together they can be seen to cause competing effects, where increasing silane flow rate reduces the atomic hydrogen density but increases the possible deposition rate, Conversely increasing power boosts density of atomic hydrogen and facilitates high silane depletion promoting crystalline growth at higher deposition rates.
   - This method allows for the complete de-coupling of the fractional flow and residence time as factors contributing to gas phase density ratio.

Figure 4.6 shows 3 graphs. Each graph illustrates how the RCF uniformity of films behaves at three silane flow rates a) 50 sccm, b) 63 sccm, and c) 75 sccm, corresponding to 10%, 12.5%, and 15% of the 500 sccm total flow respectively. The 5 measurement points are consistent for all RCF uniformity graphs presented in this thesis and run along the long (720mm) axis of the MAMELUKE source between the centre of tile 2 and the centre of tile 4. The 5 spatial points of measurement are alternately located in

front of[9] three tile faces and two tile boundaries as shown in figure 4.5.

Each graph illustrates the uniformity of the RCF for different levels of forward power 2600 W, 3000 W and 3400 W which, assuming zero losses in the power transmission from generator to source, correspond to power densities of 0.60 W cm^{-2}, 0.69 W cm^{-2}, and 0.79 W cm^{-2} respectively.

The RCF is measured using a Kaiser Optical Systems spectrometer operated in a backscattering micro-raman configuration as illustrated in figure 3.7 with a laser wavelength of 785nm. Each spectrum consists of the average of 2, 20 second exposures with a suitable dark background subtraction. After completing the 3-peak fitting procedure described in section 3.2 the RCF is calculated using equation 3.3.

Examining first figure 4.6 a) films prepared at the lowest (50 sccm) silane flow over the longest (20 min) deposition, films of uniform, high RCF are seen for all powers. The crystalline fraction approaches the maximum achievable RCF point in each of these depositions; for these experiments, it appears that a value of 0.7 for the RCF is the point of "saturation." The maximum measurable RCF is a common feature for all experiments of this type, but the point of saturation will most likely be unique to a specific measurement conditions[10]. Beyond this point changing the process settings so as as as to increase the crystalline fraction[11] does not discernibly increase the measured RCF.

By contrast, figure 4.6 b) shows films prepared at an increased flow (63sccm). The average RCF of all depositions is lowered and non-uniformities in RCF are discernible between the tile centre positions and the tile edges, particularly at 3000 W . This can be attributed to the increase in silane flow; at the lower power settings the electron density is not sufficient to dissociate the increased flow of silane as efficiently. The

[9]While the RCF is measured on the substrate here we are using the source as a reference for the position given that we are most interested in the effect of any plasma spatial structure on the films

[10]there are 2 factors which explain the saturation i) there will always be a finite amorphous component of the spectrum and ii) because selecting a cross section of 1 underestimates the total crystalline volume of the solid so even for small levels of amorphous material the amorphous contribution to the spectrum will be accentuated

[11]increasing the forward power, reducing the silane flow, or increasing the deposition time should increase the crystalline fraction of the material

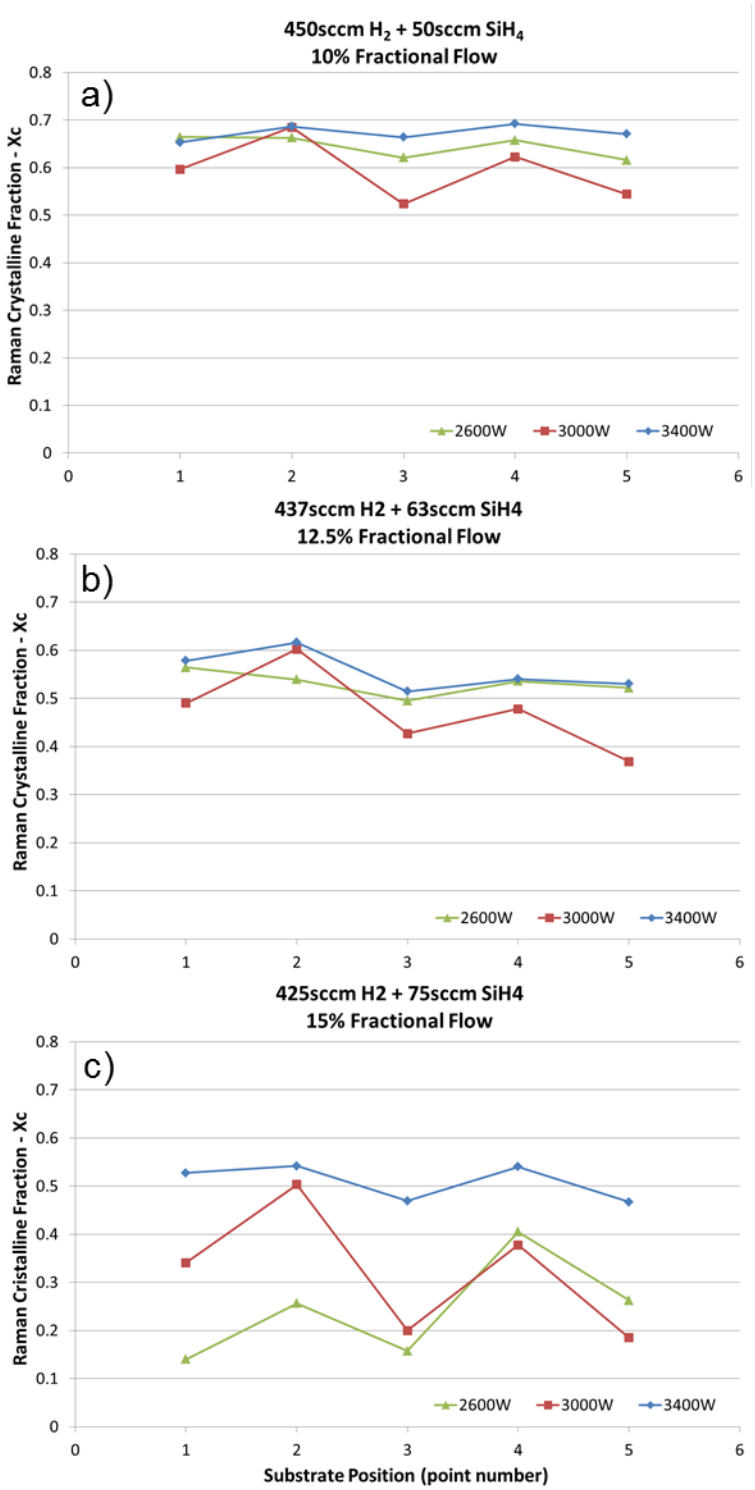

Figure 4.6: The uniformity of Raman crystalline fraction (RCF) for different levels of 162MHz power. Each graph represents films deposited with a different fractional flow of silane (10%, 12.5%, 15%). The total gas flow, pressure, temperature and other process parameters are held constant for all depositions

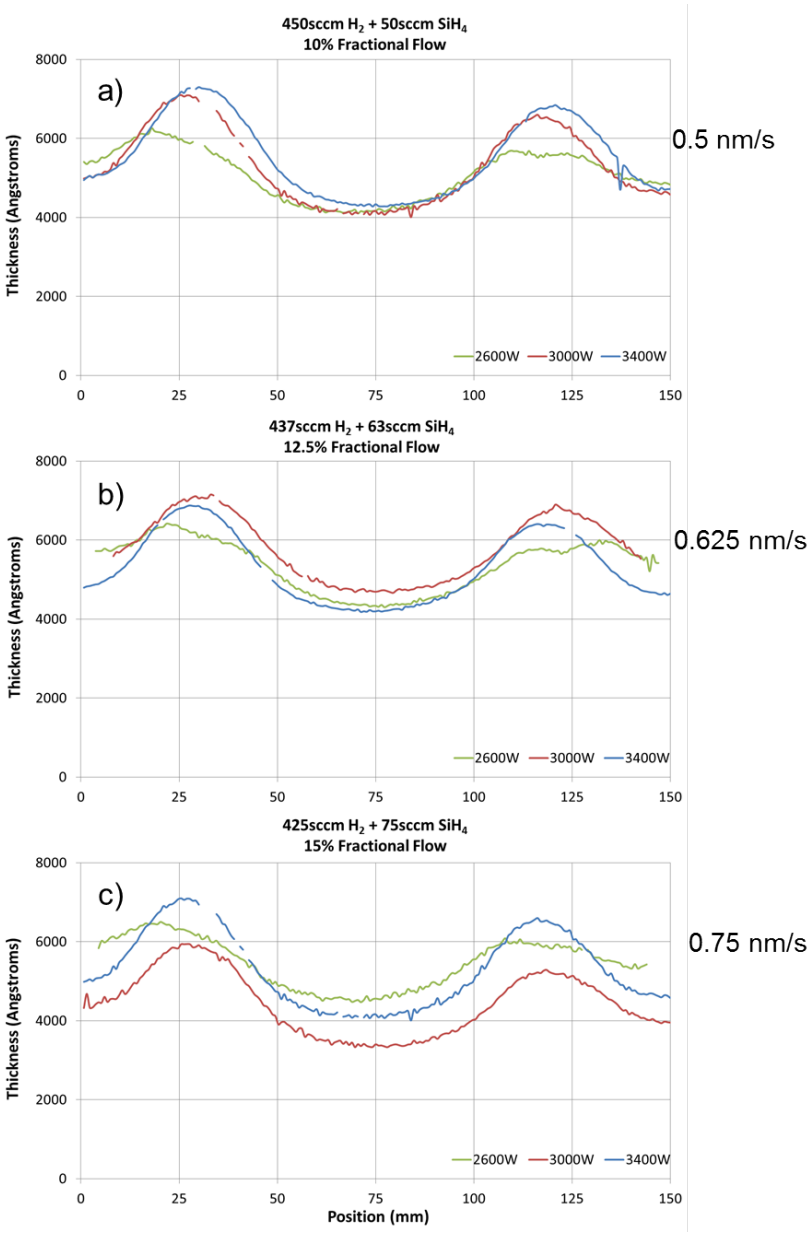

Figure 4.7: The uniformity of film thickness for different levels of 162MHz power. Each graph represents films deposited with a different fractional flow of silane (10%, 12.5%, 15%). The total gas flow, pressure, temperature and other process parameters are held constant for all depositions. Given that the deposition time for each group of 3 depositions is constant the equivalent deposition rate of a 6000 Angstrom film is noted on the right hand side of each graph

silane density in the plasma is increased and the atomic hydrogen density is reduced which as described in section 1.3 leads to a reduction in crystalline fraction.

This trend continues further in figure 4.6 c) (75 sccm silane flow). The average RCF at 3400 W is only reduced slightly compared to the other flow regimes while retaining good RCF uniformity. The depositions at lower power exhibit increasing non-uniformity compared to those deposited with a silane flow rate with 63 sccm, the areas of high RCF are located at the tile boundaries and low RCF at the tile faces.

It was then seen as appropriate to add confidence to the observed uniformity of the material properties of deposition preformed at higher powers. To this end the relative fraction of crystalline growth in different planes was investigated for an apparently uniform deposition. Specifically the deposition preformed at a silane flow of 63 sccm and a forward power of 3400 W (figure 4.6 b)) was examined at positions corresponding tile faces (3 & 5) and tile edges (2 & 4) as seen in figure 4.8. The relative fraction of crystalline growth in the 111, 220, and 311 planes was calculated by measuring the area each of the respective peaks as described in section 3.5. The results of these measurements are seen in figure 4.8 b) and it can easily determined to a reasonable level of confidence that the material growth is indeed uniform as suggested by the RCF measurements.

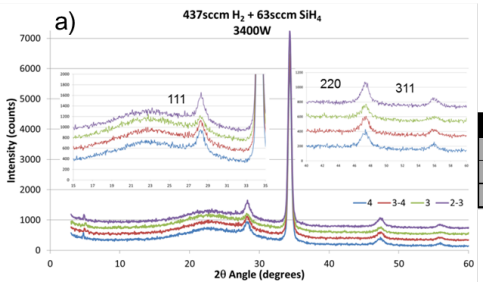

b)

	2	3	4	5
111	0.49	0.43	0.53	0.53
220	0.32	0.39	0.32	0.33
311	0.18	0.18	0.14	0.14

Figure 4.8: The behaviour of X-ray diffractogrammes taken at positions on the substrate corresponding to tile faces (3 & 5) and tile edges (2 & 4). 4 diffractogrammes measured for films from the same deposition with relativle uniform crystalline fraction a) to the left. Peaks associated with the 111, 220, and 311 planes of crystalline silicon are observed and the relative intensity (area) of these peaks is shown in the table, b) to the right

The low power RCF non-uniformities displayed in all three graphs of figure 4.6

are consistent with either a plasma gas chemistry inhomogeneities or with deposition rate non-uniformities. The results discussed previously in section 4.1 show a strong correlation between the film thickness of a sample and the measured RCF, which is strongly supported by the known growth mechanisms of nc-Si:H, specifically the development of an amorphous incubation layer early in deposition which slowly transitions to crystalline growth with increasing thickness. Given this correlation examining the thickness uniformity of these depositions helps identify the nature of plasma inhomogeneities across a muli-tile source. A thickness profile of each deposition is measured and analysed using the procedures described in section 3.3.

Both the laser wavelength (785 nm) and the range of film thicknesss determine the extent to which the film thickness effects the measurement of the RCF. The penetration depth of the 785 nm is long enough that all measurements in rage of thicknesss should represent the volume averaged crystalline fraction but given that the thicker film will have a smaller fraction of their bulk in the incubation layer the effect cannot be completely discounted. In addition, previous studies have also seen that for higher deposition rates the crystalline fraction of films fall. Based on this it is not trivial to predict what if any thickness non-uniformities will be displayed working from the RCF data alone. To investigate, the thickness uniformity of all samples shown in figure 4.6 are measured using the DekTak and plotted using the same layout as figure 4.7. The location of the profilomenter measurement is displayed in figure 4.5. The thickness is measured along a strip, adjacent to the RCF measurement locations.

It is informative to view the thickness data with a consideration for the fractional utilisation of the silane gas. To accomplish this we consider the maximum achievable deposition thickness. Knowing that each deposition has been exposed to 1000 standard cubic centimetres of silane gas we can calculate the total mass of the available silicon as follows:

$$m_{SiH_4} = \frac{\rho_{SiH_4} P}{nRT} \cdot (0.874) V_{SiH_4} \tag{4.1}$$

Where ρ_{SiH_4} is the gas density of Silne, P is the gas pressure (1 atm), n is is the number of moles (=1), R is the universal gas constant (= 82.1 $\frac{cm^3 \cdot \text{atm}}{mole \cdot \text{Kelvin}}$), T is the temperature

(=273.15 Kelvin), and V_{SiH_4} is the volume of silane (=1000 scc). We introduce a factor of 0.874, which is the fraction of mass associated with silicon (the 4 hydrogen atoms per molecule making up the rest). This calculation gives a total deposition mass of $\approx 1.2525\,g$. Taking the density of solid silicon to be $2.329\,g \cdot cm^{-3}$ and assuming that the substrate represents one half of the deposition area[12]. The maximum achievable average film thickness is then calculated to be 6224 Angstroms.

For all depositions we found that the films were thicker at the tile boundary than at the tile centre, which mirrors the pattern seen in the non-uniform RCF measurements. Initially this would seem to indicate that despite the long penetration depth of the excitation laser, the film thickness continues to have a strong influence on the measured RCF in these depositions. After further scrutiny however, it is seen that those depositions which show the greatest non-uniformity in RCF - those deposited at low power (2600W) - show the lowest non-uniformities in thickness. In addition the thickness uniformity seems to show little or no sensitivity to the silane gas flow rate which strongly effects the RCF uniformity. As such it seems more likely that the RCF non-uniformities are as a result of the gas chemistry inhomogeneities.

To further emphasise the strength of correlation between the measured RCF and the net silane flow[13] the data in figure 4.6 is replotted in figure 4.9 such that the power is constant for each graph. In each successive graph (increasing power, a$\longrightarrow$b$\longrightarrow$c) it is found that the strength of the RCF dependence on silane flow decreases. This result further supports the idea that power and silane flow counteract each other in producing a plasma chemistry desirable for crystalline growth. To clearly display the contrast of this behaviour with that of the thickness uniformity figure 4.10 displays figure 4.9 a) with the equivalent thickness measurements. Despite the difference in silane flow rate, the silane exposure is kept constant and the thickness at all points remains essentially constant, which indicates efficient Silane utilisation for all flow rates.

Under the assumption that the effect of film thickness on the RCF uniformity can

[12]The electrode surface making up the other half

[13]the correlation is to both the average RCF of a given deposition and the uniformity of the crystalline fraction form tile face to tile edge

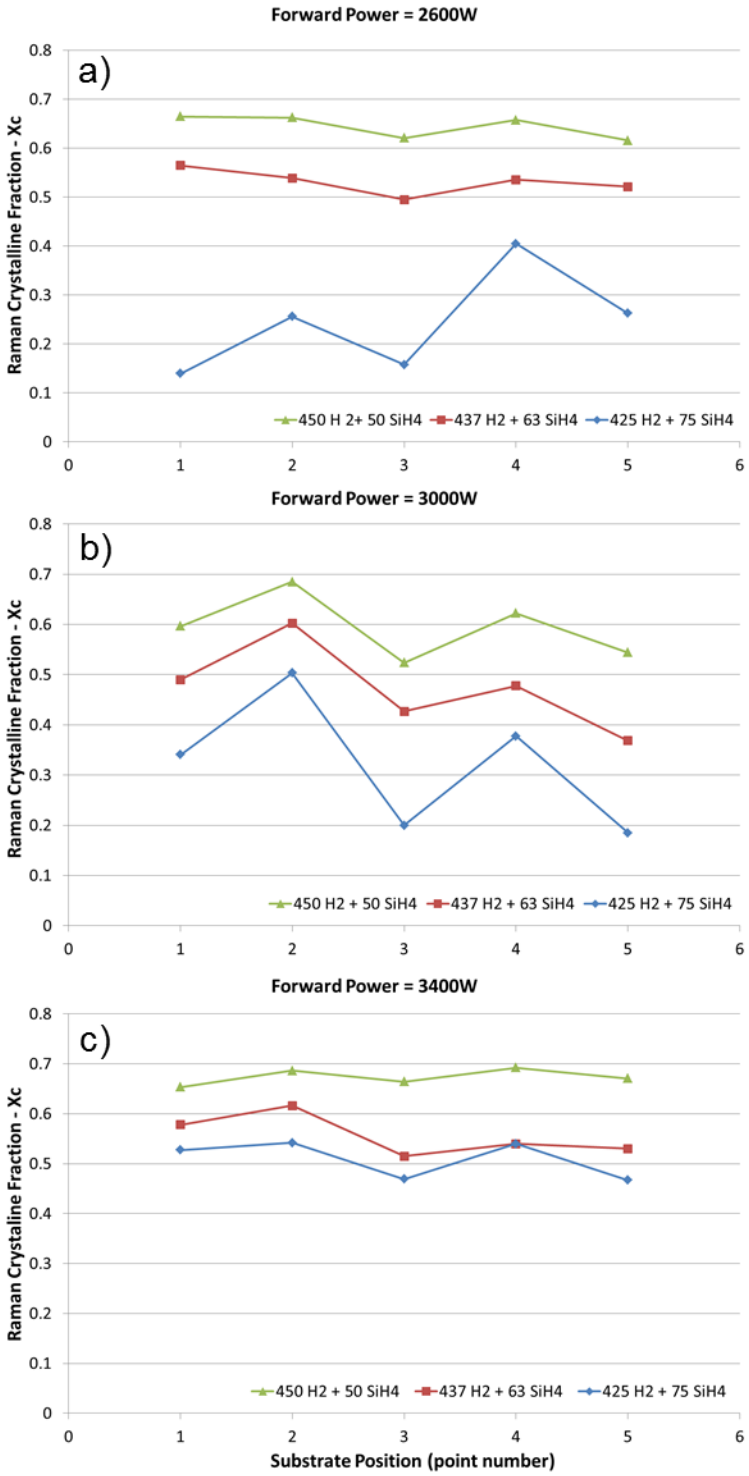

Figure 4.9: The uniformity of Raman crystalline fraction (RCF) for different levels of Silane Fractional Flow. Each graph represents films deposited with a different forward 162MHz power set-point (2600W, 3000W, 3400W). The total gas flow, pressure, temperature and other process parameters are held constant for all depositions

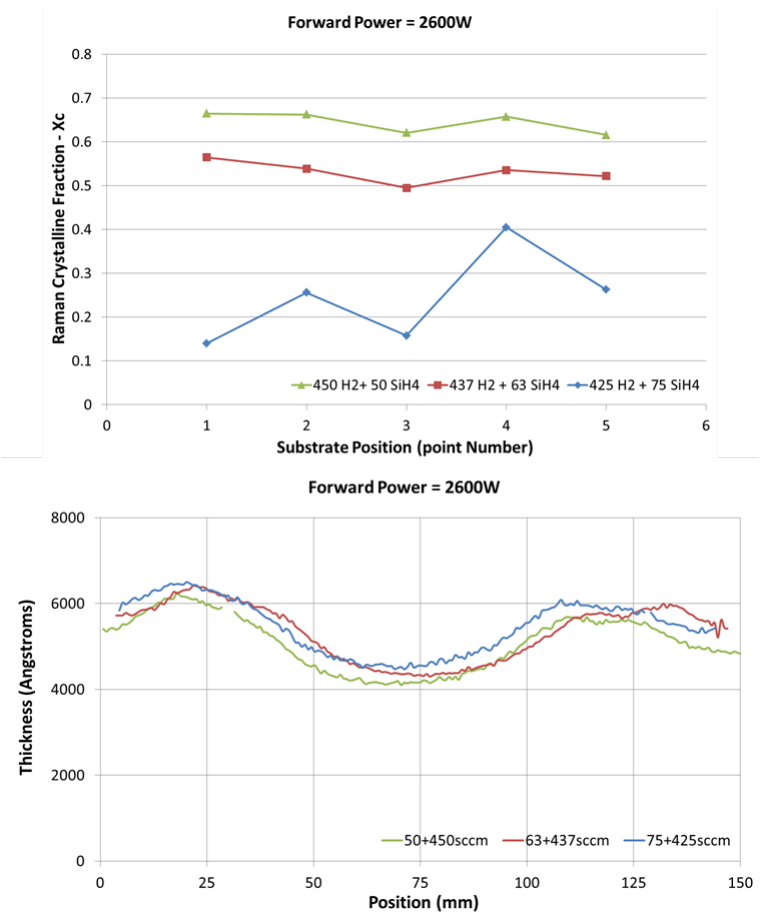

Figure 4.10: RCF and thickness uniformity for depositions preformed at 2600W forward power. The figure emphasises the disparity between the 2 effects. For the lower silane flow depositions high levels of RCF uniformity are seen despite higher deposition at the tile edges. In addition large discrepancies are seen when comparing the depositions to each other. Significant changes in the RCF level are not reflected at all in the thickness profile which remains constant.

be ignored it is necessary to consider other explanations for the RCF non-uniformity at low powers and/or high silane flow. As discussed in section 1.4.1 the push-pull, multi-tile configuration of the MAMELUKE source introduces a spatial structure; which may induce plasma chemistry non-uniformity. We must then consider the following as possible causes for the RCF profiles.

- The un-equal power delivery by capacitive and inductive coupling through the sheath
  - Increased deposition rate at the tile edges indicates a higher electron density when compared to the tile face due to strong inductive coupling
  - This will result in a higher dissociation of silane molecules giving rise to attractive conditions for films with higher VCF (and RCF), specifically low mono-silane density and high atomic hydrogen density
  - This effect is accentuated at higher forward powers by a decreased skin depth[14] of the plasma which lowers the impedance of the system to the inductive currents
- The interruption of the gas delivery shower head by inter-tile dielectric.
  - The absence of gas delivery at the tile edge means that the incoming gas mix will have translated some distance through the plasma before arrival at a point on the substrate opposite the dielectric
  - If the frequency of silane dissociation is comparable to the inverse of the gas residence time this could lead to a partial depletion of the gas before arrival at the tile edge
  - As a result the plasma in front of the tile edge will have a higher density of atomic hydrogen and a lower density of mono-silane, a condition which is favourable for crystalline growth at the higher deposition rates experienced as a result of high power deposition through inductive coupling

[14] as a result of higher electron density

Both of these possibilities are supported by the trends seen in the data. They explain the behaviour of the RCF pattern when experimental settings give rise to conditions where the fractional dissociation of silane is low. As the silane flow is increased the crystalline fraction at the tile face drops dramatically while the at the tile edges it remains high.

The postulation of high inductive coupling between this tiles is strongly supported by the shape of the deposition pattern and its accentuation at higher powers. The theory that unequal gas delivery over small displacements can affect local gas chemistry is less easily supported. The gas pressure and the surface area of the source are such that the assumption of laminar flow behaviour is valid, but it is not necessarily known that the residence time of a silane molecule is comparable to the inverse of the rate of dissociation. The validity of this theory is investigated by changing the residence time while maintaining the net silane flow. To achieve this effect the further depositions are preformed while the hydrogen flow is reduced, halving the total gas flow from 500 sccm to 250 sccm. This has the side effect of doubling the fractional flow of silane. Conventionally this reduction in the hydrogen dilution would be thought to reduce the atomic hydrogen density in the plasma producing a more amorphous growth regime. In figure 4.11 we see that this is not the case.

Depositions were preformed using the new flow rates at the 3 standard power set points; 2600 W , 3000 W , and 3400 W . The measurements of RCF show high crystalline fraction and high RCF uniformity for all 3 power levels. This is indicative of a increased steady state population of atomic hydrogen despite the substantial reduction in hydrogen fractional flow. The difference is most prominent at the tile faces where, previously crystalline fraction was seen to drop significantly at at lower powers and high silane flow rates (figure 4.9). This result strongly supports the theory that VHF excitation is capable of facilitating crystalline deposition through heavy depletion of silane. In addition this result highlights the significance of gas residence time in determining the steady state gas chemistry, specifically in achieving a heavily depleted silane population. Given that the time required for silane dissociation is comparable to

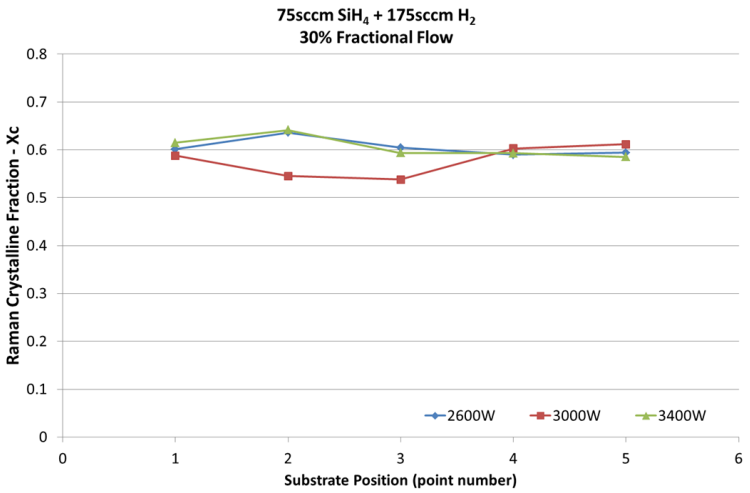

Figure 4.11: The uniformity of Raman crystalline fraction (RCF) for different levels of 162MHz power. Process conditions for depositions are as before with the exception of the total gas flow which is decreased to increase the gas residence time. As a side effect the Silane fractional flow is doubled when compared to previous depositions, despite this RCF remains high and uniform for all depositions

the residence time this supports the claim the partially dissociated gas flowing from the tile face to the tile edge will induce local gas chemistry inhomogeneities, specifically a reduction in the molecular silane density and an increase in the atomic hydrogen density, directly impacting the crystalline fraction but not necessarily the deposition rate.

Chapter 5

Discussion & Conclusions

This chapter will concentrate on giving context to the data presented in chapter 4, drawing conclusions specifically relevant to the behaviour of multi-tile sources. Specifically information concerning the nature of the plasma produced as well as the quality of deposited films will be discussed. An elaboration of conclusions presented in chapter 4 will be presented here, looking at the body of research as a whole, referencing information taken from a combination of graphs and datasets to reach a series of more complete conclusions regarding the results. The results will be compared and contrasted to the body of established knowledge gained from previous work (chapter 2). With this in mind the data will be used to show where operation of a VHF multi-tile source for PECVD of nc-Si:His fully consistent with and where it differs from previous works.

Initially we will make conclusions concerning the properties of the nc-Si:H films produced, drawing conclusions on the plasma properties as well as the material properties. Given these conclusions we will discuss the film growth characteristics in term of the desirability for industrial manufacturing. Separately we will discuss conclusions related to the measurement tools and techniques used for film analysis, specifically raman spectroscopy and profilometry. The applicability and limitations of the methods will be discussed with the context of the analysis of thin film silicon. Finally we will outline a summary of conclusions concerning the nature of multi-tile sources in general and as it relates to the applicability of multi-tile sources for large VHF-PECVD as well

as other plasma processing applications.

5.1 Film Characteristics: Deposition Rate and Crystalline Fraction

Nano-crystalline silicon layers have been produced at high deposition rate with a high degree of crystalline fraction uniformity. This is particularly evident in figure 4.7 c) where the deposition rate exceeds 7.5 Ås^{-1}.[1] All 3 depositions in this plot have some degree of crystallinity and the deposition preformed at 3400 W shows a uniform RCF of approximately 0.5. It is also concluded that this combination of deposition rate and RCF can be optimised further using the gas residence time as a control. This can be seen in figure 4.11 where higher levels of RCF are found for all powers, while maintaining the RCF uniformity. The silane flow rates and deposition times for each set of depositions is the same, depositions produced at higher silane fractional flow but longer residence time maintain highly uniform RCF at lower powers.

Existing industrial manufacturing process for nc-Si:H manufacturing remain limited in deposition rate of nc-Si:H despite recent progress implementing higher frequencies excitation to good effect[83, 87, 91, 92]. Hardware solutions such as dielectric lens[87, 91] and ladder electrode[83, 92] have shown the limited capability to increase the excitation frequency to 40 MHz and 100 MHz respectively, but so far no so solution has been found to implement higher frequencies over large areas. In addition experimental results on small area substrates have shown that further increasing the frequency continues to allow greater power to be coupled to the plasma while avoiding amorphization by high energy bombardment as discussed in many previous works[17, 24] (Section 2.1.1) resulting in higher nc-Si:H deposition rates. The combination of both of these developments highlight the need for hardware solutions offering even greater flexibility in the choice of excitation frequency independently of substrate area. In this study we have shown the potential of multi-tile CCP sources as a solution to this challenge.

Previous results have also shown that the combination of high power VHF excitation and high pressure depletion (HPD) can further increase the deposition rate[42, 58, 60].

[1] The deposition rate maxima between the tiles exceed 6000 Å, which for this process time is equivalent to 7.5 Ås^{-1}

HPD allows even higher power densities to be achieved while avoiding high energy ion bombardment. The high gas pressure increases the number of collisions experienced by an ion crossing the sheath. The dissipation of each ions energy through additional collisions reduces the amount of particles with sufficient impact energy to cause an amorphization event.

It should be noted that the ion bombardment energy continues to scale inversely with frequency[17, 24]. It is concluded that in simply utilising 162 MHz excitation, conditions similar to HPD regimes were achieved without the necessity for increased pressure. Furthermore it is also conceivable that in contrast to traditional, 2-electrode plasma sources[2] the push-pull multi-tile configuration drives a significant portion of current between the tiles through the plasma rather than to the grounded substrate electrode. Depending on the fractional current shunted through the plasma this would have significantly reduced the dependence of the substrate ion bombardment energy on the power coupled to the plasma.

It is concluded that further work in this area should explore higher power densities at low pressures to determine whether amorphization effects become apparent and the higher pressures become necessary. This was not attempted as part of this study because of the additional power requirements which were not available while using the existing apparatus. Increased power could be delivered to the plasma by either increasing available power[3]. Alternatively it would be possible to reduce thermal power losses in both the RF matching network and the multi-tile source thus increasing the fraction of power delivered to the plasma to the plasma. In addition further work should include a study of the fractional current driven through the plasma as opposed to the substrate in the push-pull configuration, which would inform the dependence of ion energy on the ion impact energy at a grounded surface.

The results of this study show that both the deposition rate uniformity and the RCF uniformity of films were effected by the spatial structure imposed on the plasma

[2]2-electrode sources in this context refer here to un-segmented parallel plate reactors, or even segmented electrodes powered in phase

[3]Depositions preformed in this study were close to the 3600 W maximum power available from the generator

by segmenting the powered electrode. The majority of depositions produced have a thickness maximum at tile edges with the layer becoming thinner in front of the tile face. The deposition thickness pattern has been shown to be strongly controlled by the total forward power. Depositions produced at lower power levels show a reduced difference between the tile-edge and face and further reducing the power has been shown to produce films with tile face dominated thickness profiles.

Whether the pattern is tile-edge dominated or tile face dominated deposition thickness consistently displays distinct differences between tile faces and tile edges. Depending on the relative strength of capacitive and inductive coupling, local changes in power coupling will be seen, at the tile centre or tile edge positions respectively. The relative independence to these power coupling mechanisms is determined, primarily, by the plasma skin depth (δ_P) and plasma resistivity (ρ_P)[4], which are dependant on the plasma density explaining the observed control of the thickness profile by changing the forward power set point.

This is not to say the the only means of controlling the thickness profile is by fine tuning the forward power levels, other process parameters such as gas pressure can also have a meaningful influence on the plasma density but process parameters are not the only means by which to control film thickness uniformity. The relative strength of capacitive and inductive power coupling mechanisms could be altered by changing the geometry of the segmented electrode. Specifically the tile size and the length of the inter-electrode gap could be changed so as to achieve equal capacitive and inductive coupling for the desired electron density for a given industrial process.

The RCF uniformity of deposited films also displays distinct differences between tile edges and tile faces, which will be further discussed in the context of the gas phase chemistry uniformity (section 5.2).

[4]The strength of inductive coupling couples with the plasma skin depth while the strength of capacitive coupling scales with the resistivity

5.2 Silane Depletion and Gas Phase Dynamics

It is concluded that the combination of high deposition rate and high crystalline fraction of the films produced are as a result of the VHF plasma produced by the MAMELUKE source as explored in section 5.1. This behaviour (figures 4.6 and 4.7) is consistent with many previous studies[45, 72, 73, 93, 94] which show that VHF excitation produces plasmas with a higher electron density and lower electron temperature compared to equivalent powers of conventional 13.56 MHz RF plasma. In a high electron density plasma such as is described, silane radicals are being produced by dissociative reactions at extremely high rates.

It is concluded that VHF excitation is responsible for capability of MAMELUKE to deposit crystalline silicon films in processes with significantly lower levels of hydrogen dilution. The majority of previous works investigating suitable dilution regimes have seen a transition to amorphous growth at silane fractional flows < 0.1[11, 18, 95, 96]. Figure 4.11 shows consistently high RCF measurements where the silane fractional flow is is 30%. We attribute this contrasting behaviour to high depletion[19, 57, 90] of the silane source gas and high rates of H_2 production attributable to high deposition rates. High rates of silane dissociation allow for high rates of deposition as explained in section 1.3. This effectively reduces the steady state silane density in the plasma and increases the steady state hydrogen density. The effective dilution of the plasma is therefore dependant on the rate of silane dissociation providing further incentive to research VHF solutions for large area industrial plasma.

The increasing electron temperatures of plasmas produced at high power densities with lower RF frequency (13.56 MHz) give rise, not only to high energy ions, as described in section 5.1, but also to increased production of higher order radicals, leading to dust[16], as discussed in section 1.3. It is concluded that lower order radicals (SiH_3) are preferentially produced in MAMELUKE. This conclusion is based the fact that no dust is observed in films when depositing films at high powers (and subsequently at deposition rates not available to conventional (13.56 MHz) PECVD due to dust).

We further support the previous conclusion using observations of the silane utilisa-

tion and deposition rate made in section 4.2. When comparing depositions of a different silane flow rate the deposition thickness was found to be essentially constant as long as the deposition time was altered to allow for constant silane exposure. Furthermore it was found that all layers produced are approaching the calculated maximum achievable thickness given the total mass of silicon delivered to the plasma[5] (equation 4.1). Then concentrating on the high deposition rate of films produced even at low powers we can conclude that the deposition rate is driven more strongly by the silane mass flow rate than the power (figures 4.7 and 4.10)

It is clear from the above that MAMELUKE produces a highly dissociated gas phase chemistry at all powers, but given the lack of powder at higher powers it is also evident that for all powers, there is a low population of SiH_2. It is evident that at higher powers the density of dissociative electrons far exceeds that required for full dissociation and despite this SiH_3 is the preferentially produced radical.

Further to the frequency effects it is concluded that gas residence time in the source is a more significant factor than hydrogen dilution in determining the plasma gas chemistry and thus the morphology of silicon films. This again is demonstrated by the results seen in 4.11. This low dilution regime shows the potential for even higher deposition rates than those demonstrated in chapter 4.

Experimental results also demonstrate that the uniformity of gas phase chemistry in MAMELUKE is not necessarily dependant on the local power deposition. While deposition thickness non-uniformities are seen to be accentuated at high powers, evidence of gas chemistry inhomogeneities is more prominent in layers deposited at lower powers. The RCF of films produced by MAMELUKE are seen to generally remain more uniform at higher powers. At lower powers, the crystalline fraction in front of the tile face fall lower than at the tile edge. It is concluded that this effect is attributable to the absence of source gas delivery between the tiles[6]. As a result the gas supply to these locations has undergone partial dissociation and depletion. The plasma at

[5]This observed quantitatively as the maximum thickness calculation assumes uniform deposition thickness and each of out depositions has a non uniform thickness profile

[6]As discussed in section 3.1 the gas delivery shower head of MAMELUKE is interrupted by the inter-tile dielectric

tile boundaries has a lower density of gas phase silane and a higher density of atomic (and molecular) hydrogen than the tile face both factors allow for deposition of highly crystalline material at flow and power settings which reduce the crystalline fraction in front of a tile face.

5.3 Measurement Techniques and Analysis

Raman spectroscopy is a powerful tool for the analysis of multiphase thin film silicon due to the ease of measurement and analysis[67–69]. Depending on the wavelength of the laser used different information can be inferred from the resulting spectra. Given the thickness range of films examined (3500Å to 7000Å) and the range of laser wavelengths used (488 nm to 785 nm) the dependence of penetration depth on wavelength is significant. Specifically, this means that, longer wavelengths of 633 nm and 785 nm were used to infer information concerning the thickness averaged crystalline fraction of the deposition while the shorter wavelengths of 488 nm and 514 nm were used to infer information about the surface crystalline fraction of the deposition. Primarily for the proposes of this study it was desirable to analyse the volume averaged crystalline fraction so as to avoid sensitivity to film thickness. In addition the use of lower wavelengths were useful to demonstrate growth trends which compare favourably with the existing literature. This is particularly pertinent given the growth mechanisms of nc-Si:H, specifically the presence of an amorphous incubation layer at the initial stages of growth. Using shorter wavelength lasers neglects the presence of the this incubation layer and as such dramatically overestimates the films crystalline fraction.

The Raman spectra of multiphase silicon remains, as of yet, unable to accurately represent the absolute volumetric crystalline fraction of the film[62, 66, 97] It is worth mentioning that no film analysis technique to date can be said to give an absolute and numerically accurate measure of the volumetric crystalline fraction of nc-Si:H films. As a result no “standards” for the measurement of VCF can be made. In addition no calibration factor can be determined to convert the measured RCF to the absolute VCF.

It outside the boundaries of this study to resolve outstanding questions within the field of raman analysis of nc-Si:H but it is worth summarizing the existing limitations to give context to the results presented. Primarily when considering the raman analysis of multi-phase silicon necessary to be aware of the difficulties in discerning an accurate relative absorption coefficient. There are several factors which make choosing a suitable

figure inherently complex.

- Given the multiphase nature of the material it is not fully understood whether the relative absorption coefficients remain the same as when nano-crystallites and amorphous material are analysed in isolation (separately). Furthermore it is possible that grain boundary material contributes to the relative absorption behaviour but again grain boundary material can not be examined in isolation.

- The absorption coefficient of nc-Si:H is dependant on the average crystallite size. Given that the the crystallite size varies as a function of layer thickness the relative absorption may also vary depending on both the collection depth of the laser used. In addition assuming a single absorption cross section for the volume averaged film may prove inaccurate.

- Amorphous material found within nc-Si:H, especially that found in incubation layers and adjacent to grain boundaries, may not necessarily behave the same as pure amorphous material examined in isolation.

The choice of a relative absorption coefficient of 1 in these experiments is consistent with many similar studies in the literature and while imperfect will offer consistency as well as always underestimate the volumetric crystalline fraction as explained in chapter 3.2.

Studies in the literature also suggest that there is no clear number of crystalline peaks with which to achieve a reasonable least squares fit while offering a physical effect that would account for the additional peaks. Different authors have advocated for the use of 2-peak and 3-peak methods, with one study advocating for a method where the amorphous $480\,\mathrm{cm}^{-1}$ is subtracted from the spectrum based on fitting to the secondary peaks adjacent to the $480\,\mathrm{cm}^{-1}$ to $518\,\mathrm{cm}^{-1}$ range. This is followed by a separate fitting to the remaining crystalline portion.

Again, there is no clear answer to suggest which method more closely represents the VCF and the method adopted in this study was chosen primarily for consistency with existing studies and secondarily because it is known to consistently trend with VCF.

In addition the arguments that a single intermediate peak could be attributed to grain boundary material was convincing and consistent while there was little justification for addition of further intermediate peaks.

Likewise the use of a DekTak profilometer was extremely powerful in the analysis of multiphase thin film silicon. While acquiring thickness measurements in a a single location proved to be accurate and easily repeatable, care must be taken in the analysis thickness uniformity behaviour over large scales. Significant challenges are present in automating both levelling procedures, and step height measurements for large sample geometries; whereas measurements over small scales or even single spot measurements have proved trivial. Small misalignments of the substrate on the DekTak stage and difficulties in producing a defect free reference strip exacerbate the challenge and can cause levelling errors leading to spikes in the thickness profile. By following the preparation, measurement and analysis procedures described in section 3.3 these spikes could be minimised. When these points were removed from the data the remaining information was found to be sufficient for analysis of the thickness profile.

5.4 Multi-tile sources

With the above conclusions in mind we will now make a series of conclusions relating specifically to multi-tile sources:

1. The division of the powered electrode into tiles allows for the production of uniform VHF plasmas over far greater substrate area than can be achieved by conventional, 2-electrode CCP source design, which develop wavelength dependent non-uniformities as the excitation quarter-wavelength approaches the electrode radius.

2. The spatial structure imposed my segmenting the electrode has direct but controllable impact on the local gas phase chemistry of the plasma and as a result the local film growth properties when used for the PECVD of nc-Si:H.

3. The operation of MAMELUKE in a push-pull, washer-board configuration using the PSTLD increases the ease of producing plasma with full substrate coverage.

4. The push-pull power delivery configuration means that there is zero net current being driven into / out-of the plasma at each point in time, minimising effects encountered by poor ground connections or asymmetrical grounding paths.

5. Depending on the fraction of current shunted through the plasma as opposed to through the grounded substrate, the push-pull configuration reduces the dependence of ion bombardment energy on the power delivered to the plasma.

6. Since each of the PSTD output pairs are electrically isolated from each other, problems with localised plasma are minimised Problems of of this nature are often associated with segmented electrodes lacking electrically isolated power delivery to each tile .

5.5 Concluding Remarks

The MAMELUKE source is found to be capable of high rates of nc-Si:H deposition. This is indicative of a high electron density, low electron temperature plasma. This finding is consistent with, and add weight to the existing body of research which suggests that VHF excitation of plasma provides unique plasma processing capabilities. Specifically the high rate deposition of nc-Si:H offers the potential of significant cost reduction in the manufacture of thin film solar panels utilising nanocrystalline absorber layers either in isolation or as part of a multi-junction configuration.

The spatial structure produced by segmenting the powered electrode of MAMELUKE, and the push-pull power delivery provided by the PSTLD has been shown to be both predictable and controllable. Power deposition non-uniformities are found to be the dominant effect in producing deposition rate non-uniformities, as a result producing uniform films for a given process simply becomes a matter of balancing capacitive coupling at tile centres with inductive coupling at tile edges. These findings offer insight for the future design of multi-tile plasma technology for all applications.

The crystalline fraction of nc-Si:H films are not significantly effected by the segmentation of powered electrode and as a result multi-tile sources remain an attractive solution to the limitations encountered by conventional 2-electrode sources. Interruption of the shower head gas delivery by inter-tile dielectric can induce RCF non-uniformity. This gives insight into the significance of silane gas residence time in determining the steady state fractional dissociation in the plasma. This is further demonstrated by producing films of high, uniform crystalline fraction with low hydrogen dilution and high gas residence time. This is specifically applicable to the development of new processes in thin-film solar manufacturing.

Bibliography

[1] B. Chapman, *Glow Discharge Processes: Sputtering and Plasma Etching*. A Wiley-Interscience publication, Wiley, 1980.

[2] A. Fridman and L. Kennedy, *Plasma Physics and Engineering*. Taylor & Francis, 2004.

[3] G. Franz, *Low Pressure Plasmas and Microstructuring Technology*. SpringerLink: Springer e-Books, Springer, 2009.

[4] S. Samukawa, "Development of high-density plasma reactor for high-performance processing and future prospects," *Applied Surface Science*, vol. 192, pp. 216–243, May 2002.

[5] S. Oda, "Frequency effects in processing plasmas of the vhf band," *Plasma Sources Science and Technology*, vol. 2, pp. 26+, Feb. 1993.

[6] P. C. Boyle, A. R. Ellingboe, and M. M. Turner, "Independent control of ion current and ion impact energy onto electrodes in dual frequency plasma devices," *Journal of Physics D: Applied Physics*, vol. 37, pp. 697+, Mar. 2004.

[7] D. L. Staebler and C. R. Wronski, "Reversible conductivity changes in discharge-produced amorphous si," *Applied Physics Letters*, vol. 31, no. 4, pp. 292–294, 1977.

[8] J. Cifre, J. Bertomeu, J. Puigdollers, M. C. Polo, J. Andreu, and A. Lloret, "Polycrystalline silicon films obtained by hot-wire chemical vapour deposition," *Applied Physics A*, vol. 59, no. 6, pp. 645–651, 1994.

[9] H. Matsumura, "Formation of silicon-based thin films prepared by catalytic chemical vapor deposition (cat-cvd) method," *Japanese Journal of Applied Physics*, vol. 37, no. Part 1, No. 6A, pp. 3175–3187, 1998.

[10] S. Klein, F. Finger, R. Carius, T. Dylla, B. Rech, M. Grimm, L. Houben, and M. Stutzmann, "Intrinsic microcrystalline silicon prepared by hot-wire chemical vapour deposition for thin film solar cells," *Thin Solid Films*, vol. 430, pp. 202–207, Apr. 2003.

[11] A. Matsuda, "Formation kinetics and control of microcrystallite in μc-si:h from glow discharge plasma," *Journal of Non-Crystalline Solids*, vol. 59-60, pp. 767–774, Dec. 1983.

[12] A. Matsuda, "Growth mechanism of microcrystalline silicon obtained from reactive plasmas," *Thin Solid Films*, vol. 337, pp. 1–6, Jan. 1999.

[13] C. C. Tsai, G. B. Anderson, R. Thompson, and B. Wacker, "Control of silicon network structure in plasma deposition," *Journal of Non-Crystalline Solids*, vol. 114, pp. 151–153, Dec. 1989.

[14] K. Nakamura, K. Yoshino, S. Takeoka, and I. Shimizu, "Roles of atomic hydrogen in chemical annealing," *Japanese Journal of Applied Physics*, vol. 34, no. Part 1, No. 2A, pp. 442–449, 1995.

[15] S. Sriraman, S. Agarwal, E. S. Aydil, and D. Maroudas, "Mechanism of hydrogen-induced crystallization of amorphous silicon," *Nature*, vol. 418, pp. 62–65, July 2002.

[16] H. Kawasaki, H. Ohkura, T. Fukuzawa, M. Shiratani, Y. Watanabe, Y. Yamamoto, S. Suganuma, M. Hori, and T. Goto, "Roles of $\mathbf{sih_3}$ and $\mathbf{sih_2}$ radicals in particle growth in rf silane plasmas," *Japanese Journal of Applied Physics*, vol. 36, no. Part 1, No. 7B, pp. 4985–4988, 1997.

[17] B. Kalache, A. I. Kosarev, R. Vanderhaghen, and Roca, "Ion bombardment effects on microcrystalline silicon growth mechanisms and on the film properties," *Journal of Applied Physics*, vol. 93, no. 2, pp. 1262–1273, 2003.

[18] A. Matsuda, "Microcrystalline silicon: Growth and device application," *Journal of Non-Crystalline Solids*, vol. 338-340, pp. 1–12, June 2004.

[19] B. Strahm, A. Howling, L. Sansonnens, C. Hollenstein, U. Kroll, J. Meier, C. Ellert, L. Feitknecht, and C. Ballif, "Microcrystalline silicon deposited at high rate on large areas from pure silane with efficient gas utilization," *Solar Energy Materials and Solar Cells*, vol. 91, pp. 495–502, Mar. 2007.

[20] A. Kohno, T. Sameshima, N. Sano, M. Sekiya, and M. Hara, "High performance poly-si tfts fabricated using pulsed laser annealing and remote plasma cvd with low temperature processing," *Electron Devices, IEEE Transactions on*, vol. 42, pp. 251–257, Feb. 1995.

[21] I. Kaiser, N. H. Nickel, W. Fuhs, and W. Pilz, "Hydrogen-mediated structural changes of amorphous and microcrystalline silicon," *Phys. Rev. B*, vol. 58, pp. R1718–R1721, Jul 1998.

[22] M. A. Lieberman, J. P. Booth, P. Chabert, J. M. Rax, and M. M. Turner, "Standing wave and skin effects in large-area, high-frequency capacitive discharges," *Plasma Sources Science and Technology*, vol. 11, pp. 283+, Aug. 2002.

[23] G. A. Hebner, E. V. Barnat, P. A. Miller, A. M. Paterson, and J. P. Holland, "Frequency dependent plasma characteristics in a capacitively coupled 300mm wafer plasma processing chamber," *Plasma Sources Science and Technology*, vol. 15, pp. 879–888, Nov. 2006.

[24] K. Kohler, D. E. Horne, and J. W. Coburn, "Frequency dependence of ion bombardment of grounded surfaces in RF argon glow discharges in a planar system," *Journal of Applied Physics*, vol. 58, no. 9, pp. 3350+, 1985.

[25] A. A. Howling, Dorier, C. Hollenstein, U. Kroll, and F. Finger, "Frequency effects in silane plasmas for plasma enhanced chemical vapor deposition," *Journal of Vacuum Science & Technology A: Vacuum, Surfaces, and Films*, vol. 10, pp. 1080–1085, July 1992.

[26] W. Schwarzenbach, "Sheath impedance effects in very high frequency plasma experiments," *Journal of Vacuum Science & Technology A: Vacuum, Surfaces, and Films*, vol. 14, pp. 132+, Jan. 1996.

[27] L. Sansonnens, A. A. Howling, and C. Hollenstein, "Electromagnetic field nonuniformities in large area, high-frequency capacitive plasma reactors, including electrode asymmetry effects," *Plasma Sources Science and Technology*, vol. 15, pp. 302+, Aug. 2006.

[28] X.-M. Zhu, W.-C. Chen, S. Zhang, Z.-G. Guo, D.-W. Hu, and Y.-K. Pu, "Electron density and ion energy dependence on driving frequency in capacitively coupled argon plasmas," *Journal of Physics D: Applied Physics*, vol. 40, pp. 7019–7023, Nov. 2007.

[29] L. Sansonnens, A. Pletzer, D. Magni, A. A. Howling, C. Hollenstein, and J. P. M. Schmitt, "A voltage uniformity study in large-area reactors for RF plasma deposition," *Plasma Sources Science and Technology*, vol. 6, pp. 170+, May 1997.

[30] M. Lieberman and A. Lichtenberg, *Principles of Plasma Discharges and Materials Processing*. Wiley, 2005.

[31] T. Michna and A. R. Ellingboe, "Characterisation of an rf power splitter for multi-tile pecvd systems application," *Current Applied Physics*, vol. 11, pp. S9–S11, Sept. 2011.

[32] S. Vepřek and V. Mareček, "The preparation of thin layers of ge and si by chemical hydrogen plasma transport," *Solid-State Electronics*, vol. 11, pp. 683–684, July 1968.

[33] J. Jang, J. Y. Oh, S. K. Kim, Y. J. Choi, S. Y. Yoon, and C. O. Kim, "Electric-field-enhanced crystallization of amorphous silicon," *Nature*, vol. 395, pp. 481–483, Oct. 1998.

[34] J. Perrin, J. Schmitt, Christoph, A. Howling, and L. Sansonnens, "The physics of plasma-enhanced chemical vapour deposition for large-area coating: industrial application to flat panel displays and solar cells," *Plasma Physics and Controlled Fusion*, vol. 42, pp. B353+, Dec. 2000.

[35] C.-H. Lee, A. Sazonov, and A. Nathan, "High-mobility nanocrystalline silicon thin-film transistors fabricated by plasma-enhanced chemical vapor deposition," *Applied Physics Letters*, vol. 86, pp. 222106–222106–3, May 2005.

[36] M. Faraji, S. Gokhale, S. M. Choudhari, M. G. Takwale, and S. V. Ghaisas, "High mobility hydrogenated and oxygenated microcrystalline silicon as a photosensitive material in photovoltaic applications," *Applied Physics Letters*, vol. 60, no. 26, pp. 3289–3291, 1992.

[37] J. Meier, R. Flückiger, H. Keppner, and A. Shah, "Complete microcrystalline p-i-n solar cell—crystalline or amorphous cell behavior?," *Applied Physics Letters*, vol. 65, no. 7, pp. 860–862, 1994.

[38] J. Meier, "Recent progress in micromorph solar cells," *Journal of Non-Crystalline Solids*, vol. 227-230, pp. 1250–1256, May 1998.

[39] A. Shah, P. Torres, R. Tscharner, N. Wyrsch, and H. Keppner, "Photovoltaic technology: the case for thin-film solar cells," *Science (New York, N.Y.)*, vol. 285, pp. 692–698, July 1999.

[40] A. V. Shah, J. Meier, E. Vallat-Sauvain, N. Wyrsch, U. Kroll, C. Droz, and U. Graf, "Material and solar cell research in microcrystalline silicon," *Solar Energy Materials and Solar Cells*, vol. 78, pp. 469–491, July 2003.

[41] J. Yang, A. Banerjee, and S. Guha, "Amorphous silicon based photovoltaicsfrom earth to the final frontier," *Solar Energy Materials and Solar Cells*, vol. 78, pp. 597–612, July 2003.

[42] T. Matsui, A. Matsuda, and M. Kondo, "High-rate microcrystalline silicon deposition for pin junction solar cells," *Solar Energy Materials and Solar Cells*, vol. 90, pp. 3199–3204, Nov. 2006.

[43] V. Fthenakis, "Sustainability of photovoltaics: The case for thin-film solar cells," *Renewable and Sustainable Energy Reviews*, vol. 13, pp. 2746–2750, Dec. 2009.

[44] F. Meillaud, A. Feltrin, D. Dominé, P. Buehlmann, M. Python, G. Bugnon, A. Billet, G. Parascandolo, J. Bailat, S. Fay, N. Wyrsch, C. Ballif, and A. Shah, "Limiting factors in the fabrication of microcrystalline silicon solar cells and microcrystalline/amorphous ('micromorph') tandems," *Philosophical Magazine*, vol. 89, pp. 2599–2621, Oct. 2009.

[45] G. Parascandolo, G. Bugnon, A. Feltrin, and C. Ballif, "High-rate deposition of microcrystalline silicon in a large-area pecvd reactor and integration in tandem solar cells," *Prog. Photovolt: Res. Appl.*, vol. 18, pp. 257–264, June 2010.

[46] T. Soderstrom, F.-J. Haug, V. Terrazzoni-Daudrix, and C. Ballif, "Flexible micromorph tandem a-si/c-si solar cells," *Journal of Applied Physics*, vol. 107, no. 1, pp. –, 2010.

[47] B. Yan, J. Yang, and S. Guha, "Amorphous and nanocrystalline silicon thin film photovoltaic technology on flexible substrates," *Journal of Vacuum Science & Technology A*, vol. 30, no. 4, pp. –, 2012.

[48] Y. Uchida, T. Ichimura, M. Ueno, and H. Haruki, "Microcrystalline si: H film and its application to solar cells," *Japanese Journal of Applied Physics*, vol. 21, no. Part 2, No. 9, pp. L586–L588, 1982.

[49] M. A. Green, "The path to 25% silicon solar cell efficiency: History of silicon cell evolution," *Prog. Photovolt: Res. Appl.*, vol. 17, pp. 183–189, May 2009.

[50] Y. Hamakawa, *Thin-Film Solar Cells: Next Generation Photovoltaics and Its Applications*. Physics and Astronomy Online Library, Springer, 2004.

[51] A. V. Shah, M. Vaněček, J. Meier, F. Meillaud, J. Guillet, D. Fischer, C. Droz, X. Niquille, S. Faÿ, E. Vallat-Sauvain, V. Terrazzoni-Daudrix, and J. Bailat, "Basic efficiency limits, recent experimental results and novel light-trapping schemes in a-si:h, c-si:h and 'micromorph tandem' solar cells," *Journal of Non-Crystalline Solids*, vol. 338-340, pp. 639–645, June 2004.

[52] H. Keppner, J. Meier, P. Torres, D. Fischer, and A. Shah, "Microcrystalline silicon and micromorph tandem solar cells," *Applied Physics A*, vol. 69, no. 2, pp. 169–177, 1999.

[53] M. Heintze, R. Zedlitz, and G. H. Bauer, "Analysis of high-rate a-si:h deposition in a vhf plasma," *Journal of Physics D: Applied Physics*, vol. 26, pp. 1781+, Oct. 1993.

[54] C. Niikura, M. Kondo, and A. Matsuda, "Preparation of microcrystalline silicon films at ultra high-rate of 10 nm/s using high-density plasma," *Journal of Non-Crystalline Solids*, vol. 338-340, pp. 42–46, June 2004.

[55] Y. Mai, S. Klein, R. Carius, J. Wolff, A. Lambertz, F. Finger, and X. Geng, "Microcrystalline silicon solar cells deposited at high rates," *Journal of Applied Physics*, vol. 97, no. 11, pp. 114913+, 2005.

[56] C. Niikura, M. Kondo, and A. Matsuda, "High rate growth of device-grade microcrystalline silicon films at 8nm/s," *Solar Energy Materials and Solar Cells*, vol. 90, pp. 3223–3231, Nov. 2006.

[57] M. N. van den Donker, B. Rech, F. Finger, W. M. M. Kessels, and M. C. M. van de

Sanden, "Highly efficient microcrystalline silicon solar cells deposited from a pure sih[sub 4] flow," *Applied Physics Letters*, vol. 87, no. 26, pp. 263503+, 2005.

[58] A. H. M. Smets, T. Matsui, and M. Kondo, "High-rate deposition of microcrystalline silicon ¡equation¿p-i-n¡/equation¿ solar cells in the high pressure depletion regime," *Journal of Applied Physics*, vol. 104, pp. 034508–034508–11, Aug. 2008.

[59] E. Amanatides and D. Mataras, "Frequency variation under constant power conditions in hydrogen radio frequency discharges," *Journal of Applied Physics*, vol. 89, no. 3, pp. 1556–1566, 2001.

[60] J. K. Rath, R. H. J. Franken, A. Gordijn, R. E. I. Schropp, and W. J. Goedheer, "Growth mechanism of microcrystalline silicon at high pressure conditions," *Journal of Non-Crystalline Solids*, vol. 338-340, pp. 56–60, June 2004.

[61] A. H. M. Smets, T. Matsui, and M. Kondo, "Optimization of the high rate microcrystalline silicon deposition conditions of the multi-hole-cathode very high frequency SiH4/H2 plasma," in *Photovoltaic Energy Conversion, Conference Record of the 2006 IEEE 4th World Conference on*, vol. 2, pp. 1592–1595, IEEE, May 2006.

[62] C. Ossadnik, S. Vepřek, and I. Gregora, "Applicability of raman scattering for the characterization of nanocrystalline silicon," *Thin Solid Films*, vol. 337, pp. 148–151, Jan. 1999.

[63] M. Kondo, H. Fujiwara, and A. Matsuda, "Fundamental aspects of low-temperature growth of microcrystalline silicon," *Thin Solid Films*, vol. 430, no. 12, pp. 130 – 134, 2003. Proceedings of the Second International Conference on Cat-CVD (Hot Wire CVD) Process.

[64] L. Houben, M. Luysberg, P. Hapke, R. Carius, F. Finger, and H. Wagner, "Structural properties of microcrystalline silicon in the transition from highly crystalline to amorphous growth," *Philosophical Magazine A*, vol. 77, no. 6, pp. 1447–1460, 1998.

[65] Z. Iqbal and S. Veprek, "Raman scattering from hydrogenated microcrystalline and amorphous silicon," *Journal of Physics C: Solid State Physics*, vol. 15, pp. 377+, Jan. 1982.

[66] C. Smit, van Swaaij, H. Donker, A. M. H. N. Petit, W. M. M. Kessels, and M. C. M. van de Sanden, "Determining the material structure of microcrystalline silicon from raman spectra," *Journal of Applied Physics*, vol. 94, no. 5, pp. 3582–3588, 2003.

[67] D. Han, J. D. Lorentzen, W. J. Wolf, L. E. Mcneil, and Q. Wang, "Raman study of thin films of amorphous-to-microcrystalline silicon prepared by hot-wire chemical vapor deposition," *Journal of Applied Physics*, vol. 94, no. 5, pp. 2930–2936, 2003.

[68] M. Ledinsky, A. Vetushka, J. Stuchlik, T. Mates, A. Fejfar, J. Kocka, and J. Stepanek, "Crystallinity of the mixed phase silicon thin films by raman spectroscopy," *Journal of Non-Crystalline Solids*, vol. 354, pp. 2253–2257, May 2008.

[69] B. Strahm, C. Hollenstein, and A. A. Howling, "Uniformity of silicon microcrystallinity in large area RF capacitive reactors," *Prog. Photovolt: Res. Appl.*, vol. 16, pp. 687–691, Dec. 2008.

[70] R. Tsu, J. GonzalezHernandez, S. S. Chao, S. C. Lee, and K. Tanaka, "Critical volume fraction of crystallinity for conductivity percolation in phosphorusdoped si:f:h alloys," *Applied Physics Letters*, vol. 40, no. 6, pp. 534–535, 1982.

[71] U. Kroll, A. Shah, H. Keppner, J. Meier, P. Torres, and D. Fischer, "Potential of vhf-plasmas for low-cost production of a-Si: H solar cells," *Solar Energy Materials and Solar Cells*, vol. 48, pp. 343–350, Nov. 1997.

[72] A. Matsuda, "Control of plasma chemistry for preparing highly stabilized amorphous silicon at high growth rate," *Solar Energy Materials and Solar Cells*, vol. 78, pp. 3–26, July 2003.

[73] Y. Takeuchi, Y. Nawata, K. Ogawa, A. Serizawa, Y. Yamauchi, and M. Murata, "Preparation of large uniform amorphous silicon films by vhf-pecvd using a ladder-shaped antenna," *Thin Solid Films*, vol. 386, pp. 133–136, May 2001.

[74] W. Tsai, G. Mueller, R. Lindquist, B. Frazier, and V. Vahedi, "High selectivity plasma etching of silicon dioxide with a dual frequency 27/2 mhz capacitive radio frequency discharge," *Journal of Vacuum Science & Technology B*, vol. 14, no. 5, pp. 3276–3282, 1996.

[75] T. Kitajima, Y. Takeo, and T. Makabe, "Two-dimensional ct images of two-frequency capacitively coupled plasma," *Journal of Vacuum Science & Technology A*, vol. 17, no. 5, pp. 2510–2516, 1999.

[76] T. H. Chung, "Scaling laws for dual radio-frequency capacitively coupled discharges," *Physics of Plasmas*, vol. 12, no. 10, pp. 104503+, 2005.

[77] P. A. Miller, E. V. Barnat, G. A. Hebner, A. M. Paterson, and J. P. Holland, "Spatial and frequency dependence of plasma currents in a 300mm capacitively coupled plasma reactor," *Plasma Sources Science and Technology*, vol. 15, pp. 889–899, Nov. 2006.

[78] H. H. Goto, H. Lowe, and T. Ohmi, "Independent control of ion density and ion bombardment energy in a dual rf excitation plasma," *Semiconductor Manufacturing, IEEE Transactions on*, vol. 6, pp. 58–64, Feb. 1993.

[79] S. , Y. Nakagawa, T. Tsukada, H. Ueyama, and K. Shinohara, "Lowtemperature, uniform, and highdensity plasma produced by a new ultrahighfrequency discharge with a spokewise antenna," *Applied Physics Letters*, vol. 67, no. 10, pp. 1414–1416, 1995.

[80] S. Samukawa and T. Tsukada, "Dependence of electron energy distributions on discharge pressure in ultrahigh-frequency and inductive-coupled $\mathbf{cl_2}$ plasmas," *Japanese Journal of Applied Physics*, vol. 36, no. Part 1, No. 12B, pp. 7646–7649, 1997.

[81] S. Samukawa, V. M. Donnelly, and M. V. Malyshev, "Effects of discharge frequency in plasma etching and ultrahigh-frequency plasma source for high-performance etching for ultralarge-scale integrated circuits," *Japanese Journal of Applied Physics*, vol. 39, no. Part 1, No. 4A, pp. 1583–1596, 2000.

[82] H. Kawasaki, H. Ohkura, T. Fukuzawa, M. Shiratani, Y. Watanabe, Y. Yamamoto, S. Suganuma, M. Hori, and T. Goto, "Roles of SiH3 and SiH2 radicals in particle growth in rf silane plasmas," *Japanese Journal of Applied Physics*, vol. 36, no. Part 1, No. 7B, pp. 4985–4988, 1997.

[83] Y. Takeuchi, H. Mashima, M. Murata, S. Uchino, and Y. Kawai, "Characteristics of very-high-frequency-excited SiH4 plasmas using a ladder-shaped electrode," *Japanese Journal of Applied Physics*, vol. 40, pp. 3405+, May 2001.

[84] Y. Yang and M. J. Kushner, "450 mm dual frequency capacitively coupled plasma sources: Conventional, graded, and segmented electrodes," *Journal of Applied Physics*, vol. 108, no. 11, pp. –, 2010.

[85] A. Perret, P. Chabert, J. P. Booth, J. Jolly, J. Guillon, and Ph, "Ion flux nonuniformities in large-area high-frequency capacitive discharges," *Applied Physics Letters*, vol. 83, no. 2, pp. 243–245, 2003.

[86] L. Sansonnens and J. Schmitt, "Shaped electrode and lens for a uniform radio-frequency capacitive plasma," *Applied Physics Letters*, vol. 82, no. 2, pp. 182–184, 2003.

[87] L. Sansonnens, H. Schmidt, A. A. Howling, C. Hollenstein, C. Ellert, and A. Buechel, "Application of the shaped electrode technique to a large area rectangular capacitively coupled plasma reactor to suppress standing wave nonuniformity," *Journal of Vacuum Science & Technology A: Vacuum, Surfaces, and Films*, vol. 24, pp. 1425–1430, July 2006.

[88] P. G. Jung, S. S. Hoon, C. C. Wook, and C. H. Young, "On the plasma uniformity

of multi-electrode ccps for large-area processing," *Plasma Sources Science and Technology*, vol. 22, pp. 055005+, Oct. 2013.

[89] M. Wojdyr, "Fityk: a general-purpose peak fitting program," *J. Appl. Cryst.*, vol. 43, pp. 1126–1128, Oct. 2010.

[90] T. Roschek, B. Rech, J. Müller, R. Schmitz, and H. Wagner, "Influence of the total gas flow on the deposition of microcrystalline silicon solar cells," *Thin Solid Films*, vol. 451-452, pp. 466–469, Mar. 2004.

[91] H. Schmidt, L. Sansonnens, A. A. Howling, C. Hollenstein, M. Elyaakoubi, and J. P. M. Schmitt, "Improving plasma uniformity using lens-shaped electrodes in a large area very high frequency reactor," *Journal of Applied Physics*, vol. 95, no. 9, pp. 4559–4564, 2004.

[92] H. Mashima, Y. Takeuchi, M. Murata, M. Noda, A. Yamada, H. Takatsuka, O. Urabe, and Y. Kawai, "Characteristics of the electron temperature in vhf-excited SiH4/H2 plasma produced using a ladder-shaped electrode," *Vacuum*, vol. 74, pp. 503–507, June 2004.

[93] U. Kroll, "From amorphous to microcrystalline silicon films prepared by hydrogen dilution using the vhf (70 mhz) gd technique," *Journal of Non-Crystalline Solids*, vol. 227-230, pp. 68–72, May 1998.

[94] Z. Wu, Q. Lei, J. Xi, Y. Zhao, and X. Geng, "Hydrogenated microcrystalline silicon films prepared by VHF-PECVD and single junction solar cell," *Journal of Materials Science*, vol. 41, pp. 1721–1724, Mar. 2006.

[95] U. Kroll, J. Meier, A. Shah, S. Mikhailov, and J. Weber, "Hydrogen in amorphous and microcrystalline silicon films prepared by hydrogen dilution," *Journal of Applied Physics*, vol. 80, no. 9, pp. 4971–4975, 1996.

[96] A. M. Funde, N. A. Bakr, D. K. Kamble, R. R. Hawaldar, D. P. Amalnerkar, and S. R. Jadkar, "Influence of hydrogen dilution on structural, electrical and optical

properties of hydrogenated nanocrystalline silicon (nc-si:h) thin films prepared by plasma enhanced chemical vapour deposition (pe-cvd)," *Solar Energy Materials and Solar Cells*, vol. 92, pp. 1217–1223, Oct. 2008.

[97] R. J. Meier, "On art and science in curve-fitting vibrational spectra," *Vibrational Spectroscopy*, vol. 39, pp. 266–269, Oct. 2005.